博士論文

Development of Wide Area and High Resolution Gamma-ray Imager Based on Compton Scattering Principle

（コンプトン散乱を用いた、広域高分解能ガンマ線画像計測装置の開発）

by

江　建勇　(JIANG Jianyong)

A dissertation submitted in partial fulfillment
of the requirements for the degree of
Doctor of Philosophy
(Department of Nuclear Engineering and Management)
in The University of Tokyo
June, 2015

ACKNOWLEDGEMENTS

First and foremost I would like to thank my supervisor, Professor Takahashi Hiroyuki, who has been inspiring, encouraging and continuously supportive through my three-year Ph.D life in the University of Tokyo. He has been also challenging my ideas and techniques in a constructive way. I am very grateful for everything I have learned from him about radiation detection, and for the expert advices he suggested throughout this work. The field flights in Fukushima with our wide area imager would not have been possible without his leadership, dedication to the work, and his concern about the situation in Fukushima. As a foreigner in Japan who can not communicate in Japanese, I was carefully taken care of by him. I still remember the day when I had a bicycle accident on my way to the campus, he put aside the work on hand, immediately came to me after he got the news, and kindly helped me to solve the trouble in the police office. Without his guidance and patient help, this dissertation would not have been possible.

I am very grateful to professor Shimazoe Kenji, who played a vital role in this work. He generously shared his knowledge and expertise with me, and cultivated my abilities through the way he approached and solved problems with clarity, intuition, and common sense. I learned lots of things about detectors, electronics, and even philosophy of life from him.

In addition to those who directly contributed to this work, I very much appreciate the many wonderful people who have been supporting, loving, and guiding me along the way.

I am grateful for the funding of this work from the Japan Science and Technology(JST) under Grant number <140300000425> and the support I received through the Japanese Government Scholarship from the Ministry of Education, Culture, Sports, Science and Technology(MEXT) of Japan.

TABLE OF CONTENTS

LIST OF FIGURES

Figure

LIST OF TABLES

Table

LIST OF ABBREVIATIONS

FNPP	Fukushima Daiichi Nuclear Power Plant
AUH	Autonomous Unmanned Helicopter
DGPS	Differential Global Positioning System
CCM	Compton Camera Mode
GCM	Gamma Camera Mode
SDM	Single Detector measurement Mode
ESM	Events Selection Method via energy
GAGG	Ce:$Gd_3(Al,Ga)_5O_{12}$
FWHM	Full Width at Half Maximum
ASIC	Application Specic Integrated Circuit
FPGA	Field-Programmable Gate Array
rms	root mean square
HWHM	Half Width at Half Maximum
SBP	Simple Back Projection
FBP	Filtered Back Projection
MLEM	Maximum Likelihood Expectation Maximization
DToT	Dynamic Time over Threshold
PD	Photodiode
APD	Avalanched Photodiode
SiPM	Silicon Photomultiplier

ABSTRACT

Development of Wide Area and High Resolution Gamma-ray Imager Based on Compton Scattering Principle

by

JIANG Jianyong

Chair: Hiroyuki Takahashi

Following the Fukushima Daiichi Nuclear Power Plant(FNPP) accident on March 11, 2011, substantial amounts of radionuclides were deposited primarily within a 20 km radius from the plant and rapidly extending up to 30 km to the northwest of the FNPP owning to winds at the time of the explosions. Because of the fallout and for public safety, a government-mandated exclusion zone or evacuated area was declared which resulted in at least 185,000 people displaced from their homes. In addition, radioactive contamination was detected in dairy products from affected areas. Methods to survey and clean-up the affected regions were implemented after the accident. However, even four years later, after the accident, most of the evacuation orders have not been lifted for the affected areas, because of the scale of the contamination along with the difficulty of the decontamination.

In addition to nuclear accidents, the capability of producing, the possession of, and the illicit trafficking of nuclear weapons or special nuclear materials(SNM) by hostile individuals, groups, and non-nuclear weapons countries, is considered to be an even more general nuclear threat to the world security and public safety at this time.

Whether for the clean-up in contaminated regions in, for example, Fukushima prefecture in Japan as a result of a nuclear power plant accident, or for the detection of the presence of those types of threat nuclear weapons and SNM, instruments that are capable of detecting, localizing, characterizing, monitoring the transport of, and estimating the intensity of radioactive sources in a large area with high efficiency and accuracy are helpful and subsequently highly demanded.

Detection of electromagnetic radiation in the form of gamma rays provides a path to reconstruct the origin of nuclear materials, regarding that the vast majority of possible threat radioisotopes emit gamma rays. Gamma rays are of high frequency and they have a long range in air. Due to their high penetrating power, they are difficult to be detected. The detection and imaging of gamma rays depend upon an understanding of the methods in which the high-energy photons interact with matter. Gamma rays emitted from radioisotopes are usually within the energy band from tens of keV to a few MeV, in which, Compton camera is an ideally suited technique for detection and localization of the presence of nuclear sources.

This dissertation focusses on the design, development and characterization of a gamma-ray detection and imaging instrument that is capable of localizing radionuclides over a wide scale with high spatial resolution. We, for the first time, proposed a new airborne imaging modality through equipping a Compton camera on an Autonomous Unmanned Helicopter(AUH) that can hover and fly in a programmed route at an altitude of 10 m $\sim$ 150 m. The AUH is controlled autonomously according to a preset program in flight. A differential global positioning system(DGPS) is applied to provide the position information of the AUH. Measured data are sent to the ground station in real time through wireless data communication modules. The system was designed to work in two modes, one is Compton camera mode(CCM) which discovers the origin of radioactive sources through Compton imaging using hovering flights, while the other one is Gamma camera mode(GCM) which maps the wide spread

radiation via measured coincidence events using programmed flights.

The advantages of this new gamma-ray imager are apparently. They can easily assess activities of radioactive sources over large areas. Other than a non-directional detector which detects an increase in the detected photon rate operated in a raster pattern, the employment of Compton imaging enhances the detection accuracy of the system. This configuration is also capable of imaging the radiation distribution in high dose rate regions, for example, evacuated areas near the struck FNPP, in mountainous areas, paddy fields, and swampy grounds where are not easily accessible by people. Alternately, it would allow investigation of a scene without disturbing it, providing personnel safety from loose sources of radioactivity, and preserving evidence for eventual prosecution.

Compton camera is the heart of the wide area imager. Flying 10 $\sim$ 150 m away from the ground to conduct airborne measurements, the number of counts collected in a limited time period is essential and directly determine the accuracy of reconstructed images. For this reason, Ce:$Gd_3(Al,Ga)_5O_{12}$(GAGG) scintillation detectors with large sensitive areas(10 mm $\times$ 10 mm) are employed. The detectors are arranged in a two-planar configuration to allow for Compton imaging. The front plane consists of thinner active detectors to serve as a Compton scatter plane, while the back plane was constituted by thicker crystals to absorb the scattered photons. A new Dynamic time over threshold signal processing method was firstly and successfully applied to covert analog signals to digital signals for multi-channel spectra and coincidence measurement. Thanks for the application of this new method that is composed by simple circuits, a low power consumption and a stable circuit performance are realized.

A prototype system was firstly developed to demonstrate its capabilities for radiation detection, spectroscopy, and imaging over large areas. For the Compton camera in this prototype system, 32 GAGG crystals were coupled to 16 silicon photomultipliers and 16 avalanched photodiodes as the scatterer and absorber respectively. The

32-detector Compton camera was fully characterized within the laboratory and field environment. For point source imaging in CCM in the laboratory, an intrinsic efficiency of 1.68%±0.04% and an angular resolution of 13.9°(FWHM) at 662 keV was achieved. In GCM, a spatial resolution of 10.7 cm(FWHM) was obtained when detecting area is 11.2 cm away from the detector. The overall power consumption was 1125 mW. The prototype system was brought to Fushima in April in 2014 for the first aerial test. The instrument proved reliable and performed very well under uncontrollable temperature, high humidity, AUH vibrations, and complicated terrains. The field measurement of the prototype wide area imager in Fukushima revealed regions of high intensity of cesium among a diffuse background through aerial-based coincidence count rate mapping, Compton imaging in hovering flights and ground measurements.

Encouraged by the results obtained in Fukushima by the prototype imager, a large volume Compton camera with 128 pixels, was devised and developed with the purpose to achieve higher efficiency and angular resolution. The fully characterization of this large volume Compton camera in the laboratory environment yields a system energy resolution of 6% (FWHM) at 662 keV, an angular resolution of 8.6°(FWHM) at 662 keV in CCM, an intrinsic efficiency of 1.30±0.03% and a total power consumption of 1584 mW. With this angular resolution, the detector system is expected to achieve a spatial resolution of 1.6 m in field while it works in CCM at an altitude of 10 m. Simulations by Geant4 proved an spatial resolution of 8.8 cm(FWHM) in GCM while the detecting area was 100 mm away. Field tests using the newly developed wide area gamma ray imager has also been conducted in Fukushima. The imager performed very well, e.g. with a similar count rate from each channel, the working temperature within the compensable range of the temperature compensation circuit, and promising images obtained under complicated terrains, high humidity, and strong AUH vibrations due to the wind. Challenges to field imaging were detailedly studied

and recommendations for the next run were made based on the calibration flights.

CHAPTER I

Introduction

After the widely known Great East Japan or Tohoku Earthquake, occurring off the Pacific coast of Japan on March 11, 2011, a 15 meters high tsunami wave was generated and struck the area of Fukushima Daiichi Nuclear Power Plant(FNPP). Besides causing extensive damage and loss of life, the power supply and cooling system of the FNPP were disabled, causing core meltdown and a series of three explosions at the plant [1]. The explosions gave rise to a large scale release of radioactive materials into the environment. Substantial amounts of radionuclides were deposited primarily within a 20 km radius from the plant and rapidly extending up to 30 km to the northwest of the FNPP owing to winds at the time of the explosions. Because of the fallout and for public safety, a government-mandated exclusion zone or evacuated area was declared which resulted in at least 185,000 people displaced from their homes [2]. In addition, radioactive contamination was detected in dairy products from affected areas. Methods to survey and clean-up the affected regions were implemented after the accident. However, even four years later, after the accident, most of the evacuation orders have not been lifted for the affected areas, because of the scale of the contamination along with the difficulty of the decontamination.

In addition to nuclear accidents, the capability of producing, the possession of, and the illicit trafficking of nuclear weapons or special nuclear materials(SNM) by

hostile individuals, groups, and non-nuclear weapons countries, is considered to be an even more general nuclear threat to the world security and public safety at this time.

Whether for the clean-up in contaminated regions in, for example, Fukushima prefecture in Japan as a result of a nuclear power plant accident, or for the detection of the presence of those types of threat nuclear weapons and SNM, instruments that are capable of detecting, localizing, characterizing, monitoring the transport of, and estimating the intensity of radioactive sources in a large area with high efficiency and accuracy are helpful and subsequently highly demanded.

The vast majority of possible threat radioisotopes emit gamma rays. Therefore, detection of gamma rays provides a path to discover the presence of the radionuclides. Gamma-ray detection depends upon the understanding and predictability of how they interact with matter. In this chapter, the background and motivation of this work is firstly presented, followed by the introduction of the gamma-ray detection and imaging technologies. At the end of this chapter, the objective of the work is given.

1.1 Background and Motivation

The wide area and high resolution gamma-ray imager concept arose from a need for an instrument with substantially enhanced abilities to detect, localize and characterize radiological and nuclear materials in a wide area in Fukushima, where there were various of radioisotopes released because of the FNPP accident after the earthquake on March, 11th, 2011. Due to this accident, a large areas surrounding Fukushima have been contaminated, as shown in Figure 1.1 [3].

Radioactive materials that were released into the environment raise a threat through direct airborne exposure and as a potential contaminant of food and water sources. The threat can be short term, such as the intake of ^{131}I through diary products with its half life of 8 days, or long term, such as the chronic exposure from ^{137}Cs which is with a half life of 30 years and can be dispersed in the environment

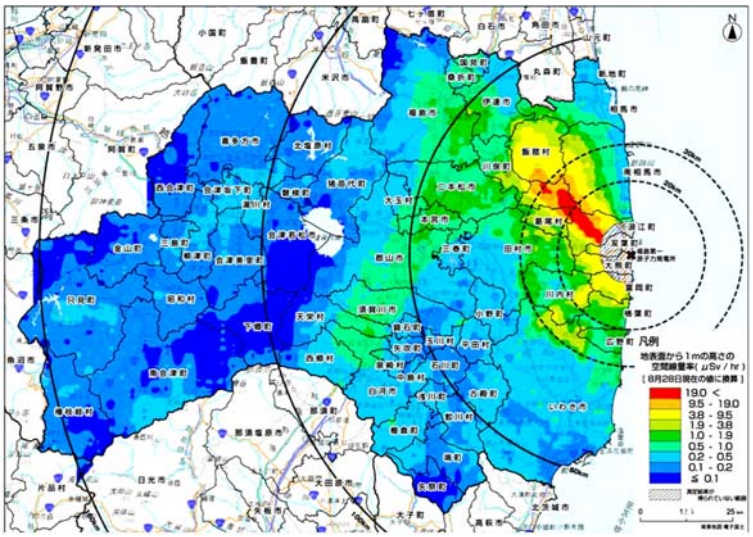

Figure 1.1: A rough distribution map of radioactive isotopes in Fukushima. From website of MEXT: Ministry of Education, Culture, Sports, Science and Technology. [3]

and last for generations.

Effective decontamination is highly demanded in order to get rid of this threat, lift the evacuation orders and encourage the evacuated people to return. Unfortunately, the contamination in Fukushima is quite complicated, not only because different kinds of radioisotopes(mainly ^{137}Cs, ^{134}Cs, and ^{131}I. [4–6]) have been released, but also because the contamination is transporting through air, on ground, and in groundwater. Of particular concern is the transport of radionuclides from contaminated regions into zones that have already been cleaned-up. Additionally, clean-up of contaminants is of high difficulty in areas, such as high dose rate regions, mountainous areas, paddy fields, and swampy grounds that are difficult of access, as illustrated in Figure 1.2. As a result, detection, localization and identification of nuclear materials in the Fukushima prefecture is a challenging but vitally important problem.

A system used to detect dangerous nuclear materials in Fukushima must have a high detection efficiency, subsequently be capable of assessing levels of radioactive contamination over a wide area, and at the meantime, have a high detection probabil-

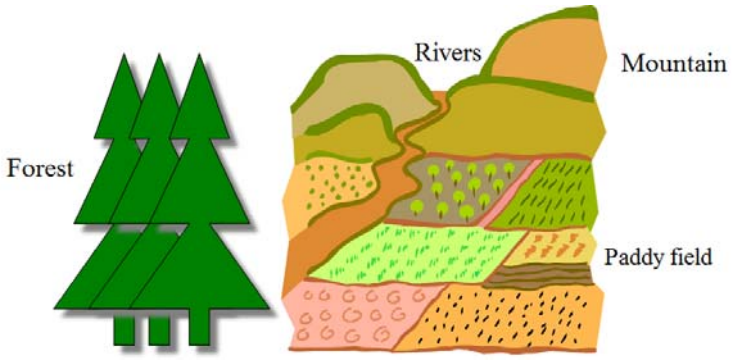

Figure 1.2: Illustration of the complicated terrains in Fukushima.

ity to reliably detect actual nuclear materials released from the nuclear power plant. Additionally, since there might be some hot spots left even after the decontamination, this wide area imager has to achieve a high spatial resolution to meter-scale for the sake of identifying those hot spots. To avoid unnecessary radiation exposure, an unmanned mobile system is preferred. This kind of instrument is also helpful at the beginning of a nuclear accident for emergency response. Because the amount of the released radioactive isotopes and the direction in which the radioactive isotopes are releasing could be easily obtained. All these information could be a great help for the government to take much more effective actions.

Besides for decontamination and emergency response in Fukushima, this imager can also be applied for use in consequence management operations and in security investigation. The imaging modality would bring the obvious benefit of providing a quicker source localization in a wide scale than could be provided by a non-directional detector operating in a raster pattern. Many ordinary materials, such as concrete, contain radioactive isotopes that contribute to the background radiation recorded by the detector. These materials, as well as cosmic radiation, are usually more broadly distributed in space than malicious radioactive objects. Position sensitive detectors have the ability to use the *apriori* knowledge that malicious sources are spatially localized to increase detection performance. Alternately, it would allow investigation

of a scene without disturbing it, providing personnel safety from loose sources of radioactivity, and preserving evidence for eventual prosecution.

1.2 Types of Radiation

Before designing a detection system to image a radiation environment, it is significant to make clear the expected emissions and their interaction methods. No radiation can be observed unless it interacts with a detector directly or indirectly.

Alpha particles, as well as fission fragments, have a very short range even in air [7], so they are hard to be measured directly unless the detector is nearly touching the emitters. Some recent works have shown that secondary ultraviolet emissions from alpha-particle-induced ionizations of air can be observed from long distances; however, a direct line of sight to a bare source [8] is required. Similarly, the range of beta particles in materials is also short, therefore most source-packaging geometries can prevent beta-particle emissions. Neutrinos or antineutrinos are also produced, however, these rarely interact. As a result, they are not practically detectable for most applications.

Neutrons are emitted by a number of threat sources. They have a long range in air and then interact with some detector materials with reasonable efficiency. The natural background of neutrons is low, so neutron-emitting threat radioisotopes are quite easily distinguishable from background. However, not all threat sources of radiation produce neutrons, limiting their use primarily to special nuclear materials [9]. Still, many of the techniques used to detect and image neutrons [10–13] have been studied.

The vast majority of possible threat radioisotopes emit gamma rays. As a result, detection of gamma rays provides a path to discover the presence of the radionuclides. Gamma rays are electromagnetic radiation of high frequency. They have a long rang in air. Due to their high penetrating power, they are difficult to be detected. However,

for the same reason, detecting gamma rays is very attractive because these high energy photons require high-Z materials to be effective shielded. Reconstructing the spatial distribution of gamma ray emitters has been studied for decades in many fields such as astrophysics [14, 15], life science [16], and industrial scanning [17]. Gamma rays are the most common to detect among particles emitted from radioactive materials. The detection and imaging of gamma rays depends on an understanding of the methods in which these high-energy photons interact with matter. This work focus on gamma-ray detection.

1.3 Gamma-ray Imaging

Understanding interactions between gamma-rays and matter is the basis for detection, spectroscopy, and imaging of gamma-ray emitters. Subsequently, it enables environmental monitoring of radioactivity, such as monitoring the widespread contamination within the Fukushima prefecture, and allows for identification and localization of nuclear materials to avoid illicit trafficking and to protect against harmful acts, ultimately. This section describes the dominant physical process, Compton scattering that enables imaging of gamma-rays within an energy band from tens of keV up to a few MeV, and summarizes the reported techniques on gamma-ray imaging.

1.3.1 Gamma-ray Interactions in Matter

There are three main gamma-ray interactions with the detector materials: photoelectric absorption, Compton scattering, and pair production. Figure 1.3 shows the relative probability of each type of interaction to occur as a function of energy in Ce:$Gd_3(Al,Ga)_5O_{12}$(GAGG) crystal. At low energies the photoelectric effect dominates, and as the photon energy increases, Compton scattering is more likely. At energies much higher than 1.022 MeV, pair production is the dominant interaction type. Although the plot shows the probability for GAGG, which is the material of

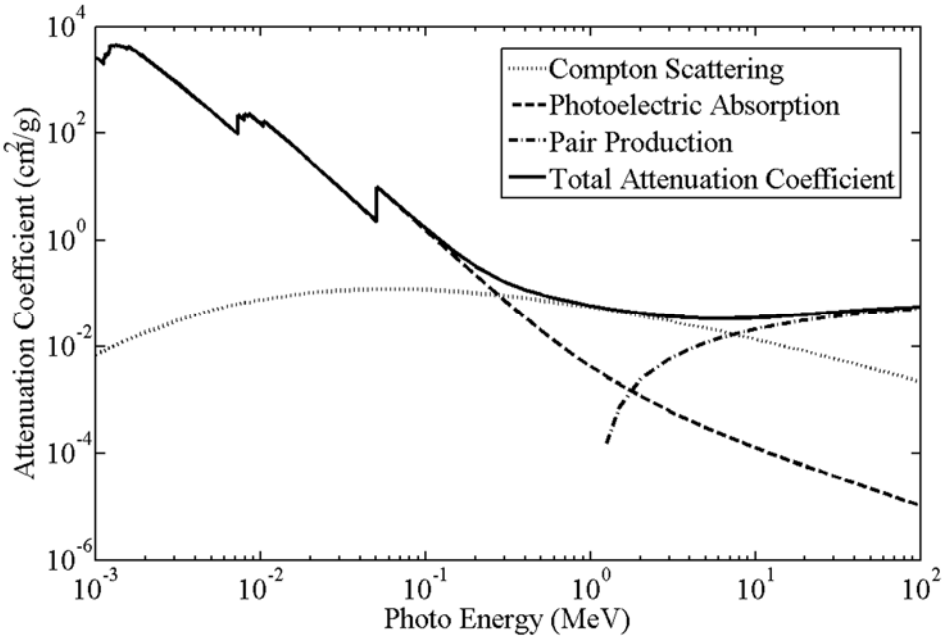

Figure 1.3: Gamma-ray attenuation coeffcient (interaction probability) for GAGG. The probability of photoelectric absorption, Compton scattering, pair production and total interactions to occur as a function of energy in GAGG crystal.

the detectors used in this work, the trends are similar for all materials. Each of these three interactions can be used to image gamma-ray [18–28].

1.3.2 Compton Scattering

Gamma rays emitted from radioisotopes are usual within an energy band from tens of keV up to a few MeV. Compton scattering is the dominant interaction process for those gamma rays in matter. The Compton scattering interaction is the basis for many of gamma-ray imaging systems that do not use collimation. Compton scattering occurs when the gamma ray interacts with an electron directly, whether it is bound to an atom or not, see Figure 1.4. Here the electron absorbs the full energy of the photon initially. However, unlike photoelectric effect, a second photon of lower energy is emitted in a different direction than the original photon. The electron then carries the difference in energy between the scattered photon and the incident photon.

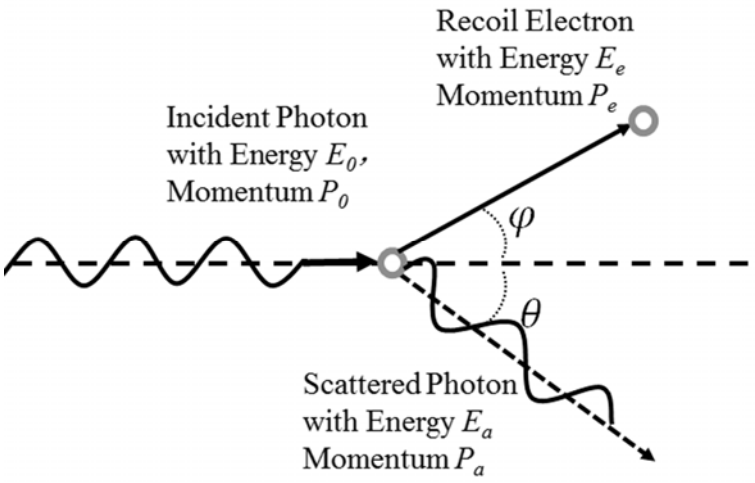

Figure 1.4: Compton scattering.

The incident direction can be determined to within the surface of a cone by recording the deposited energies at two interaction locations, if the incident gamma-ray energy is unknown. In Compton scattering, a gamma-ray elastically scatters with a weakly bound electron. The relationship between the resulting energies and scattering angle can be uniquely defined by conservation of energy and momentum based on the assumption that the electron is free and at rest. The scattering angle θ as a function of incident energy E_0, deposited energy E_s, and scattered energy E_a is:

$$\cos\theta = 1 + m_0c^2\left(\frac{1}{E_0} - \frac{1}{E_0 - E_s}\right) \qquad \text{Compton Scattering Kinematics} \qquad (1.1)$$

$$E_0 = E_s + E_a \qquad \text{Conservation of energy} \qquad (1.2)$$

The distribution of Compton scattering angles is predicted by the famous Klein-Nishina formula [29] for the differential scattering cross section $d\sigma/d\Omega$, and it has strong tendency for forward scattering at high values of the gamma-ray energy[7].

$$\frac{d\sigma}{d\Omega} = Zr_0^2\left(\frac{1}{1+\alpha(1-\cos\theta)}\right)^2\left(\frac{1+\cos^2\theta}{2}\right)\left(1 + \frac{\alpha^2(1-\cos\theta)^2}{(1+\cos^2\theta)[1+\alpha(1-\cos\theta)]}\right) \qquad (1.3)$$

Where $\alpha \equiv hv/m_0c^2$, h is the Planck constant, v the frequency of initial photon, m_0 the rest mass of electron, c the light speed, r_0 the classical electron radius, and Z the atomic number of the detector material.

The Compton scattering Equation 1.1 is based on the assumption that the electron is free and at rest before the scattering interaction. But in reality, the electron is bound to a nucleus,and has finite momentum. The non-zero initial momentum of the electron causes an effect called Doppler broadening. Since the initial electron momentum is unknown, it appears as a broadening in scattered energy at a particular angle. The effect roughly scales with atomic number and electron orbital structure. The detailed mechanism is discussed in chapter II.

1.3.3 Reported Progress on Gamma-ray Imgaing

Currently, there are several approaches having been or being developed to detect and localize gamma-ray emitters. A traditional technology for radioactive sources detection is survey meter, which detects an increase in the detected photon rate, disregarding the directions of origin. This method is easy to be applied. However, the directional information, which is useful because it allows one to gain information about the spatial distribution of the radiation emitting materials around the detector, can not be obtained. Additionally, it is time consuming and need to be done carefully. For example, in order to get stable responses with a NaI survey meter(TCS-172B), 30 seconds, 10 seconds, and 3 seconds are required for areas with dose rate below 1-2 μSv/h, around several μSv/h, and higher than 10 μSv/h, respectively [30]. In addition, adequate sampling is demanded to ensure that an area is devoid of hotspots. Further more, people who carry out the measurements take the risk of radiation exposure

Compton camera is an good candidate for detection and localization of radioactive source. It is a classical technology that exploits the physics of Compton scatter-

ing. Compton imaging has been performed with two position sensitive detectors or arrays of detectors. Sequences in which the gamma ray scatters in the front plane detector and is absorbed in the back plane detector generate a cone of possible source locations. Overlapping cones projected onto the source plane from multiple sequences yields an image of the source distribution.

Based on this principle, different types of Compton cameras have been developed, for example, the High Efficiency Multimode Imager(HEMI) [31] developed by Lawrence Berkeley National Laboratory, the 4π Compton camera with single 3D position sensitive CdZnTe detector [32–34] proposed by the University of Michigan, the Si/CdTe semiconductor based Compton camera [35, 36] developed by Japan Aerospace Exploration Agency(JAXA), and the handy Compton camera based on GAGG crystals [37] developed by Waseda University. Taking advantage of the good energy resolution of the Si and CdTe, Compton camera developed by JAXA achieved an angular resolution of 3.5°(FWHM) at 662 keV(^{137}Cs)[35]. However, the efficiency of this Compton camera was restricted by the low sensitivity of thin Si/CdTe devices, especially at energy as high as 662keV the efficiency was only 0.017% [35]. The handy Compton camera proposed by Waseda University achieved an intrinsic efficiency of 1% at 662 keV [37]. However, the area of the detector was only 10×10 mm^2 [37] and this limited the absolute efficiency of the system.

Another point worth mentioning when applying a Compton camera in field is that, gamma rays are incident from different directions and some of them will be scattered by the absorber first, as shown in Figure 1.5. These events will degrade the performance of the detector unless shielding materials or direction estimation algorithms are employed.

An alternative approach to Compton imaging is to use a collimated detector. A collimated detector has thin strips of high density materials that only allow photons from a particular direction to enter. Figure 1.6 illustrates a collimated detector.

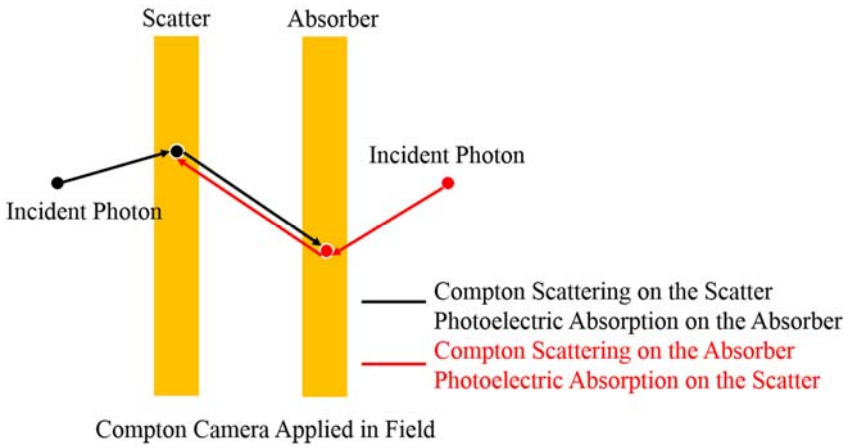

Figure 1.5: Sequence problem for ground Compton camera. For one event, it might be generated in two possible processes: one is Compton scattering on the scatter and photoelectric on the absorber, the other is just opposite, Compton scattering on the absorber and photoelectric on the scatter. Therefore, Compton sequence reconstruction algorithms or shield materials are demanded.

The pixel in which a gamma-ray interacts in the collimated detector gives information about the direction of photon origin. The cone in Figure 1.6 illustrates the possible directions of emitter for a measured photon. Note that this cone is solid and its half angle is determined by the height of the collimator. Longer collimator holes result in a narrower cone and better position resolution, but a longer collimator also blocks more photons, leading to lower sensitivity. This is a sensitivity-resolution tradeoff. In contrast, the position-sensitive Compton detector does not need a collimator to provide information about the photon direction of origin. As a result, inference about the direction of photon origin from the recorded interaction positions is sometimes referred to as "electronic collimation". The cone of possible directions of origin is hollow for a position-sensitive Compton detector, whereas the cone for a collimated detector is solid. Meanwhile, the heavy collimator makes the system difficult to be handled. Another significant difference between a Compton camera and a collimated detector is that, data processing is an integral part of the optical system. In Compton imaging systam, it is possible to effectively improve the optical

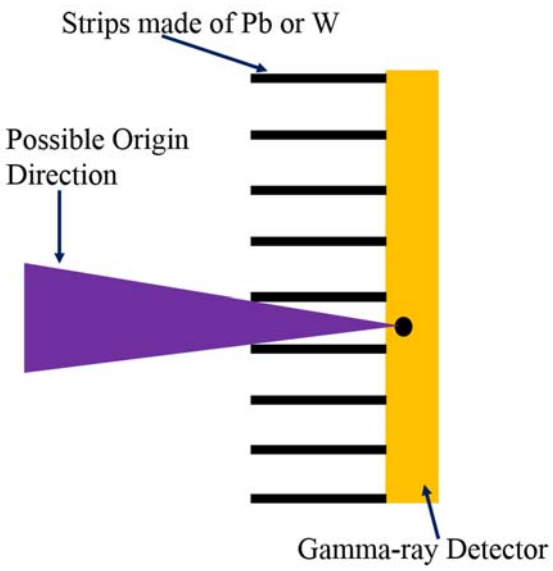

Figure 1.6: Collimated detector.

properties of the detector by operating on the input data during the generation of the image. In the collimated detector system, data processing is normally only applied to the complete image.

Pinhole type gamma camera [38–40] is another method to image gamma rays by employing a mechanical collimator, as shown in Figure 1.7. Similarly, the geometrical area of the pinhole is also restricted as another tradeoff between the angular resolution and the detection efficiency. It is also not convenient to handle this kind of system due to the employment of thick and heavy collimator made of lead(Pb) or Tungsten(W).

All the techniques discussed above are conducted on the ground. It would take years to cover the whole evacuated areas in the Fukushima prefecture in order to make clear the localized changes in background levels both before and after decontamination efforts as well as areas in which the radioactive materials tend to accumulate. Methodical ground measurements in places such as high dose rate regions, mountainous areas, paddy fields, and swampy grounds that are difficult of access, would be a grievous work. In addition, these grievous works should be done carefully and repeatedly until the area is devoid of hotspots. Therefore, ground measurement systems are

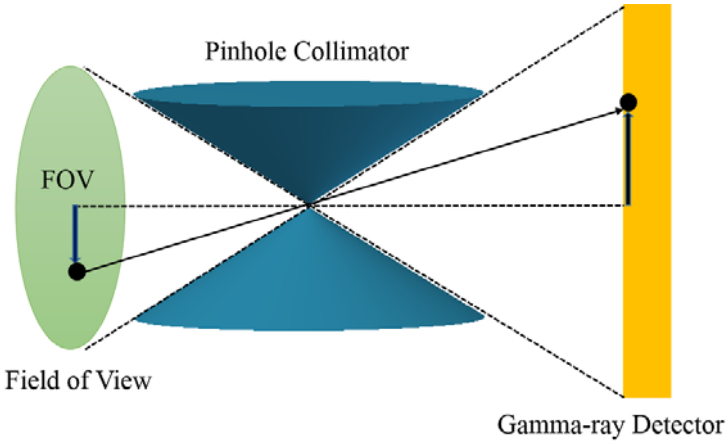

Figure 1.7: Pinhole type gamma camera.

not appropriate for radiation detection and localization in wide area application. To achieve wide area imaging capability, the Japanese government proposed an airborne radiation monitoring concept in which a radiation detection system was equipped on an airplane which could fly at an altitude of 150 m to 300 m . This method has been applied to image the radioactive materials in Fukushima. Despite its high efficiency, the spatial resolution was around 300 m to 600 m [41].

To achieve better spatial resolution, Japan Atomic Energy Agency(JAEA) proposed a remote radiation monitoring system using an autonomous unmanned helicopter [42, 43], mounted with a radiation detector(Ce:$LaBr_3$) and three CCD cameras. This unmanned remote radiation monitoring system could hover and fly at an altitude of approximately 10 m to 150 m [44]. This system can fly to destinations and return under automatic operation, measure radiation data during flight, and immediately transmit the data, including images, to a monitoring station on the ground. It is also possible to monitor the data on a map on a computer display in real time. The images are obtained by mapping the acquired count rates at each point as a function of position. Interpolation between points is applied to estimate the ground intensity. It successfully improved the spatial resolution which however, was still limited to 160 m, because the normal flight altitude was 80 m above the ground level and no selection

of the direction of incident gamma rays was performed.

1.4 Objective of this Work

The objective of this work is to design and build an unmanned and mobile gamma-ray imager that is able to detect, localize, characterize, monitor the transport of, and estimate the intensity of radiological and nuclear materials over a wide area with high efficiency and accuracy. This imager is expected to finish one scan over the whole contaminated areas in Fukushima in weeks. A spatial resolution to meter-scale is aimed at aiding and assessing the clean-up efforts of hotspots within the contaminated regions, e.g. in Fukushima, because of a nuclear accident, and for identification and localization of nuclear materials to avoid illicit trafficking in far field.

Chapter II introduces the design of wide area imager. In this chapter, a general frame of the system is firstly given, followed by the introduction of Compton camera. The principle of Compton camera, the developing history, will be described. Angular resolution and efficiency of Compton camera will be analyzed in detail, with the help of Geant4 simulation. The detector materials, the front-end electronics, the data acquisition architecture, the reconstruction algorithms, and different working modes of the imager are also presented in this chapter.

In chapter III, Geant4 simulation works are reported to optimize the design of the Compton camera, which is the heart of the proposed imager. A Geant4 description and analysis of the Compton camera parameters as how they effect the camera's performance in wide area imaging application is provided. Those parameters including the thickness of the scatterer crystals, thickness of absorber crystals, and the distance between them. Meanwhile, the performance of the proposed imager in different working modes are also evaluated using simulation before the implementations.

To demonstrate the proposed concept, a prototype system was built. The per-

formance of this prototype imager was evaluated and is introduced in Chapter IV. As a prototype, 32 Ce:$Gd_3(Al,Ga)_5O_{12}$(GAGG) crystals were coupled to 16 silicon photomultipliers and 16 avalanched photodiodes as the scatter and absorber, respectively. The performance of the system was evaluated in different working modes. As the first wide area imager using Compton imaging priciple, field experimental results in Fukushima of this prototype system are also reported in this Chapter.

Chapter V further improves the efficiency and spatial resolution by increasing the volume of the imager to 64 channels plus 64 channels. Angular resolution and efficiency of the 8×8 system are analyzed and introduced. In this chaper, a newly designed application-specific integrated circuit with 64 channels integrated as well as a new concept of reverse geometry for Compton camera are also presented.

Chapter VI is closing remarks of this thesis. The findings and contributions are summarized followed by a detailed discussion of the limitations and possible paths for optimization of the imager.

CHAPTER II

Design of Wide Area and High Resolution Gamma-ray Imager

For achieving wide area imaging capability as well as high spatial resolution, this thesis proposes a new survey system, using an Autonomous Unmanned Helicopter(AUH) equipped with a Compton camera for radioactive sources detection and localization. The AUH can hover and fly in a programmed route at an altitude of 10 m to 150 m. The proposed system can fly to destinations and return under automatic operation, collect data in flights, and immediately transmit the data to a monitoring station on the ground.

This Chapter focusses on the design of the system. An entire view of the design of the wide area and high resolution imager will be described in section I. Section II discusses the multiple mapping modes of the imager, followed by an introduction of the detector material in section III. In section IV, principle, history, reconstruction algorithms, angular resolution and efficiency of Compton scattering imagers are discussed and studied. In section V and VI, the front-end electronics and Data Acquisition(DAQ) architecture are presented.

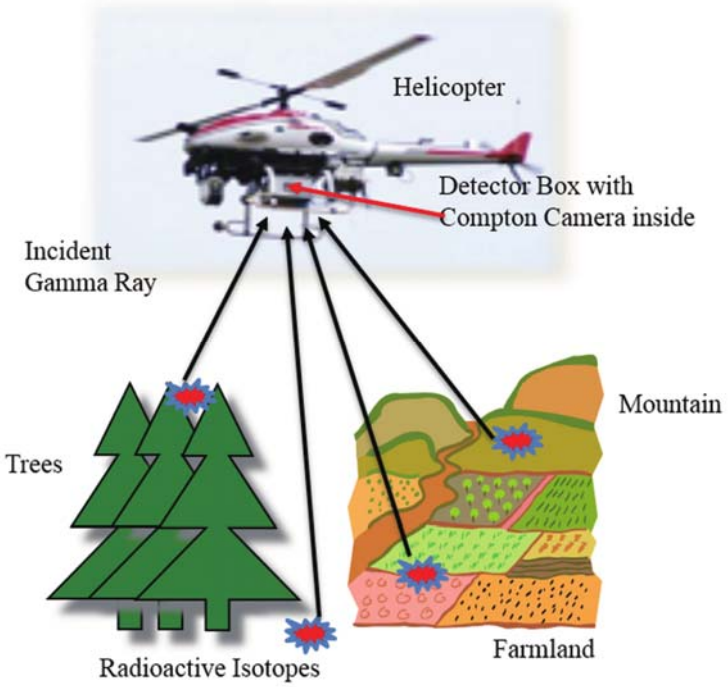

Figure 2.1: Wide area and high resolution Gamma-ray imager using an autonomous unmanned helicopter equipped with a Compton camera for radioactive sources detection and localization.

2.1 Design of the System

The concept of the new proposed system is shown in Figure 2.1. Compared with measurement performed on the ground using portable survey meter or other gamma cameras, this new system can quickly cover large areas. Measuring flights can be programmed using an autonomous flight system. Inspection of radiation distribution and investigation of the migration of the radioactive materials can be assessed in a single flight. It is also able to map the radiation distribution in high dose rate regions, for example, evacuated areas near the struck FNPP, in mountainous areas, paddy fields, and swampy grounds where are not easily accessible by people.

Other than employing a non-directional detector which detects an increase in the detected photon rate operated in a raster pattern, the employment of Compton imaging enhances the detection accuracy of the system. Without using any mechanical

collimators, Compton camera utilizes kinematics of Compton scattering and reconstructs well-defined Compton cones where the radionuclides locate. Additionally, by summing the energy losses on the scatter and absorber of coincidence events, the total energies of the incident photons can be obtained and this can be used to identify different radioisotopes by their characteristic gamma-ray energies. Taking advantage of the aerial monitoring, in which almost all the incident gamma rays are from the bottom side, sequence problem is eliminated.

The design for this wide area and high resolution Gamma-ray imager is given in Figure 2.2. In this design, a box containing the Compton camera, a computer with the data logger installed and a Wi-Fi module, is mounted on the AUH. A new Dynamic time over threshold (DToT) is applied to convert CR-RC shaping signals to digital signals. Then the digital signals are sent to a FPGA which performs multichannel spectra and coincidence measurements, and records the information of energy, position and timing of each coincident event. A differential global positioning system(DGPS) is applied to provide the information of the AUH. Measured data is sent to the ground station in real time through wireless data communication modules.

2.1.1 Autonomous Unmanned Helicopter

An AUH(RMAX G1) manufactured by Yamaha Motor Co., Ltd(Shizooka, Japan) was purchased. The AUH is controlled autonomously according to a preset program when flying, although it must be operated manually when taking off and landing. The operator could plan the flight program, including the flight path, speed, and altitude based upon the information of the position of the AUH obtained from the differential global positioning system(DGPS). The autonomous unmanned helicopter weights 94 kg and has a maximum payload capacity of 10 kg. Its speed can be as fast as 72 km/h(about 40 knots). The flight duration can be as long as 1.5 h in a filled-up fuels

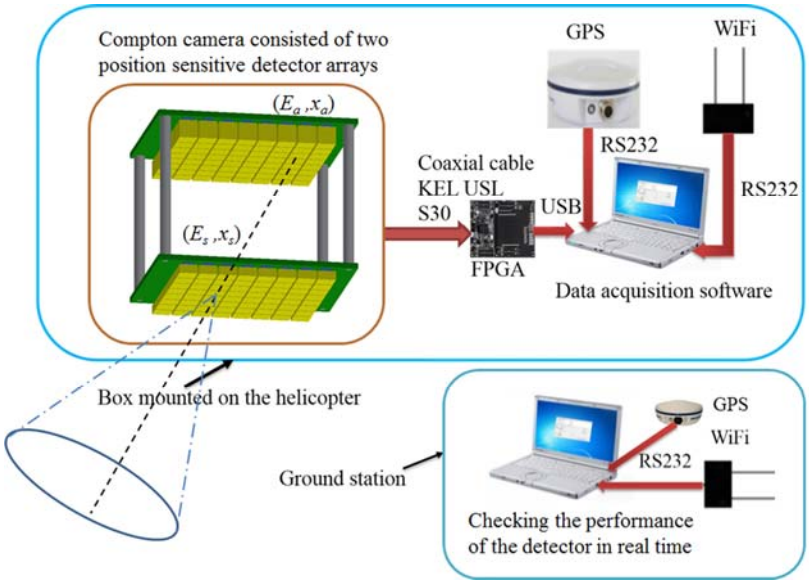

Figure 2.2: Design for a wide area and high resolution Gamma-ray imager.

situation.

2.1.2 GPS and WiFi Module

A Crescent A100 smart antenna was mounted on the helicopter to track GPS and SBAS(WAAS and EGNOS) signals at a rate of 5 Hz while another R100 GPS module was mounted on the ground station. They could achieve a differential spatial resolution of 0.6 m. Two Wireless data communication modules(FDJ03TJ010) were mounted on the helicopter and ground station respectively. Thus, the information of coincidence count rate and GPS data can be sent to the ground station in real time through the WiFi modules. The communicable distance of the WiFi module can be as long as 1500 m.

2.2 Two Mapping Modes

Traditional Compton cameras are set standstill at the same position to measure the coincidence events in order to reconstruct Compton cones utilizing Compton kinematics. However, when a Compton camera is mounted on an unmanned helicopter

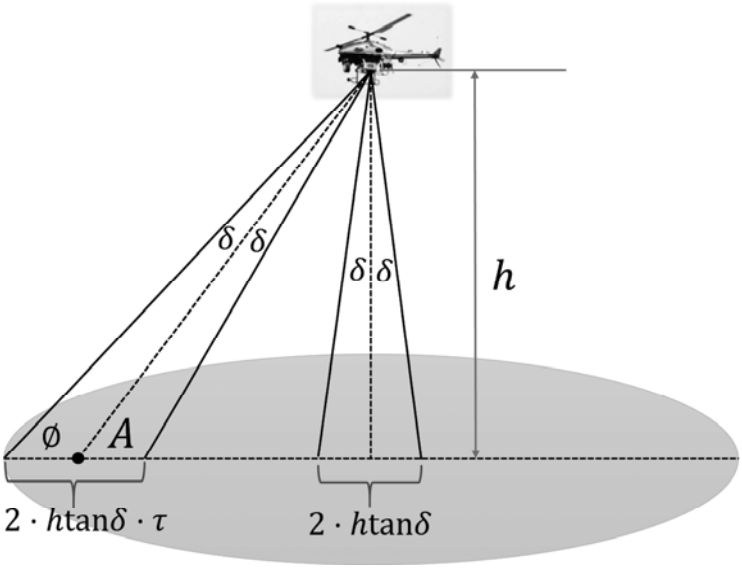

Figure 2.3: Spatial resolution analysis.

hovering from the ground, the spatial resolution depends on the distance from the place being detected to the detector. As shown in Figure 2.3, supposing the angular resolution of the Compton camera is $2\times\delta$, then the spatial resolution of the place just under the helicopter is $2\cdot h\tan\delta$ while at position A it will be $2\cdot h\tan\delta\cdot\tau$. h is the height of the detector system and ϕ is the elevation angle from position A to the helicopter.

Here,

$$\tau = \frac{\left(\frac{1}{\sin(\phi+\delta)} + \frac{1}{\sin(\phi-\delta)}\right)\cdot\cos\phi}{2\sin\phi} \tag{2.1}$$

Figure 2.4 shows the relationship between τ and ϕ while δ is set to be 4 different values. The value of τ almost doubles when ϕ is around 45°, and even quadruples when ϕ is around 30°. Considering this, we came to another idea that using the AUH carries the Compton camera to scan the contaminated places. Other than working in Compton camera mode(CCM) via reconstructing Compton cones, the coincidence count rate are used to estimate the radioactivity of the scanned places. We name this working mode Gamma camera mode(GCM). Additionally, because

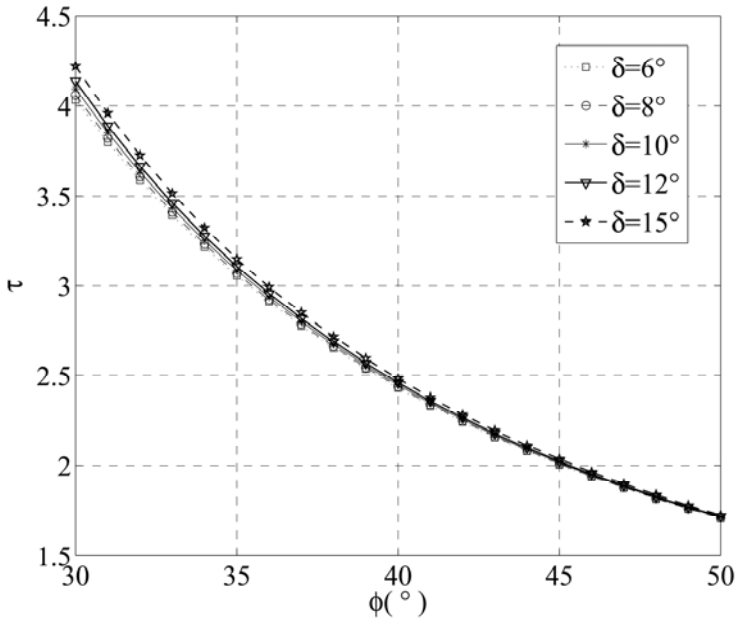

Figure 2.4: Spatial resolution variation along with the distance from the position detected to the detector.

Compton scattering angle θ is monotonically increasing while the energy deposited on the scatter E_1 increases, by only taking account the events whose energy losses on the scatter are in a certain energy range which is the so called events selection method via energy(ESM), the incident angle of the gamma rays could be selected which subsequently improves the spatial resolution of the imager.

The two mapping modes are shown in Figure 2.5. In real case, these two working modes can be combined. The system is firstly set to working in GCM to scan the contaminated places with high sensitivity, with the option of switching to CCM once a radiation field of interest has been detected.

2.3 Detector Material

Three prominent devices for gamma-ray measurement are semiconductor detectors, gas detectors and scintillation detectors. Semiconductor detectors detect gamma-rays by sensing the moving charge due to electrons freed from their orbits by

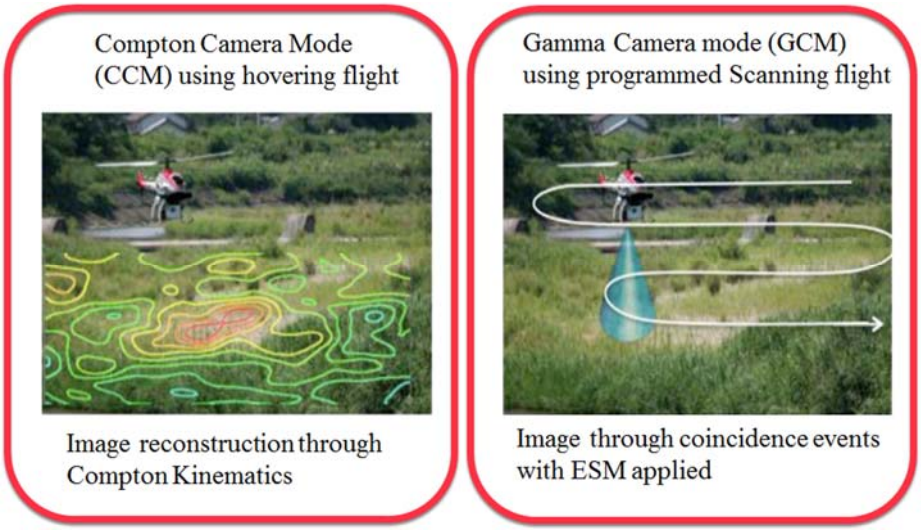

Figure 2.5: Two mapping modes. The proposed wide area and high resolution Gamma-ray imager is designed to work in two modes: one is Compton camera mode(CCM) which obtains the radiation distribution maps through Compton imaging using hovering flights, while the other one is Gamma-camera mode(GCM) which maps the radiation distribution via measured coincidence events using programmed flights.

interacting gamma-rays. Semiconductor detectors, typically, have better energy resolution than scintillation detectors and gaseous detectors. For example, Germanium detectors can exhibit less then 0.5%(FWHM) at 662 keV [45]. However, such high energy resolution can only be obtained while a cooling system is applied. At room temperature, CdZnTe detectors have been demonstrated with an energy resolution of 0.77%(FWHM) in [46]. However, the use of CdZnTe detectors have been restricted by its high cost as well as the difficulty to grow high quality and large crystals. Because of the inherent difficulties in the growth and fabrication process, the cost will probably never drop significantly. As a result, when the first priority is obtaining a large number of counts at a low price, CdZnTe would never be the detector of choice. In such a case, large volume scintillators will be used for quite some time. Room temperature semiconductor detectors made of Silicon have also been reported in [47]. However, those devices are with relatively low sensitivity.

Through measuring the charge in the atoms that are ionized by interacting high

energy photons, energy information of gamma rays can be obtained by gaseous detectors. Typically, gaseous detectors have lower sensitivity per unit volume than semiconductor detectors and scintillators due to the low density of gases. Moreover, gaseous detectors are also with worse energy resolution [7]. An example of a gaseous detector can be found in [48].

Scintillation detectors work by converting incident gamma-ray photons to visible light photons which are collect by photon detectors, such as Photomultipliers(PMT) [49, 50], Photodiodes(PD) [51], avalanched photodiodes(APD) [52], and silicon photomultipliers(SiPM) [53–55]. Thanks for their relatively high sensitivity, scintillators have been widely applied for radiation detection in the field of medical imaging, homeland security, astrophysics, phytology [56] and so on.

In our application where the wide area gamma-ray imager flies $10 \sim 30$ m away from the ground to conduct airborne measurement, efficiency or the number of counts obtained in a limited time period, is essential. Additionally, the system is better to be compact, which is free from geometrical collimators as well as cooling system. Therefore, in the fabrication of the detector, scintillator detectors was chosen. Table 2.1 shows the properties of some investigated scintillators.

From the comparison in the table 2.1, we found that GAGG(HR)[1] is a very good choice which is consisted of high atomic number elements(Z=51) and whose density is relatively high compared with other crystals such as TI:NaI, Ce:$LaBr_3$ and Eu:SrI_2[57]. It is a new scintillator with an energy resolution(FWHM) of 3.9% at 662 keV($10\times10\times10$ mm^3 size), a light output of 57000 photons/MeV, 175 ns decay time, 6.63 g/cm^3 density and No self-background radiation[58].

Besides the density and effective atomic number of the detector material, the size of the detector is also an important term which directly effects the efficiency of the system. Considering the size of normal photon detectors, as well as not increasing

[1]HR means High Resolution. In this dissertation, unless otherwise pointed out, GAGG refers to the high resolution type of GAGG from here on.

Scintillator	GAGG(HR)	GAGG	Tl:NaI	Ce:$LaBr_3$	BGO	Eu:SrI_2	Ce:La-GPS	Ce:GYAGG
Effective Atomic Number	51	51	51	46	75	49	52∼54	48
Density (g cm^{-3})	6.63	6.63	3.67	5.07	7.13	4.6	5.3	∼6.5
Light Yield (photons MeV^{-1})	57000	57000	45000	75000	8000	80000	40000	45000
Emission Wavelength Max(nm)	520	520	415	380	480	430	390	520
Decay Time (ns)	175	88	230	18	300		60	80
Energy Resolution @ 662 keV	3.9%(APD)	6.3%	6%(PMT)	3%(PMT)	12%	3-4%	5%	5%
Hygroscopic	No	No	Yes	Yes	No	Yes	No	No
Self-background	No	No	No	Yes	No	No	Low	No

Table 2.1: Properties of different scintillators.

the readout channels in order to reduces the number of electronics-induced problems that always occur during real-world operations, GAGG crystal with 10 mm $\times$ 10 mm sensitive area are employed. The thickness of the crystal will be discussed using Geant4 simulation in Chapter III.

2.4 Compton Scattering Imaging

Compton camera is the kernel technique in this work. This section will introduce the physics mechanism of Compton camera and history of Compton camera[59–69]. Front-end electronics used to amplify and convert the analog signals to digital signals will also be described. Data acquisition part and reconstruction algorithms are discussed at the end of this section.

2.4.1 Compton Scattering Imaging Principle

Typically, Compton camera consists of two position sensitive detectors. A gamma-ray emitted from a radioactive isotopes is incident to the first detector plane, which is also called scatterer where the Compton scattering takes place. The incident gamma-ray deposits part of its energy, E_s at position P_s in the first detector. For a successful reconstruction of the origin of the gamma-ray, the scattered photon has to escape from the scatterer and be absorbed in the second detector plane, which is also called absorber. The energy deposition E_a and interaction position P_a are recorded. Through the two consecutive interactions, a well-defined Compton cone can be reconstructed on whose surface the radiation source locates, as shown in Figure 2.6.

The apex of the cone is P_s, the axis of the cone is the line defined by P_s and P_a, and the half-angle of the cone is θ, which is the Compton scattering angle and can be deduced from equation 2.2 based on the assumption the electron is unbound and

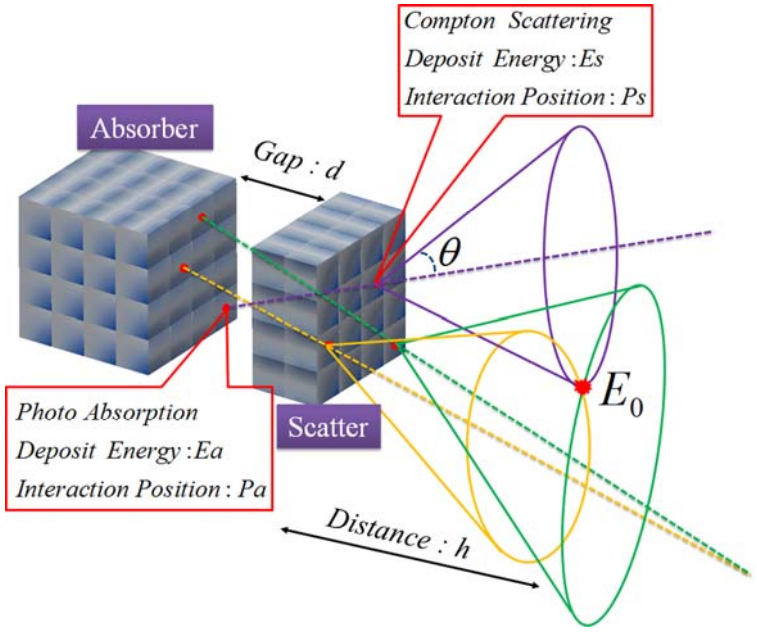

Figure 2.6: Compton scattering imaging principle.

at rest.,

$$\cos\theta = 1 + m_0c^2(\frac{1}{E_0} - \frac{1}{E_0 - E_s}) \qquad \text{Compton Scattering Kinematics} \qquad (2.2)$$

where m_0c^2 is the rest mass energy of an electron (511 keV). Each sequence of the events in the two detectors results in a cone whose intersection with the image plane is a ring. Over many events, the rings on the image plane are summed to produce an image of the source distribution. Various back projection and iterative image reconstruction algorithms have been developed to improve the quality of the image[70–77]. Pixellated detectors [78–80], orthogonal strip detectors [81, 82], or conventional planar detector arrays [37, 83] can be applied as the position sensitive spectrometers during the design and fabrication of a Compton camera.

2.4.2 History of Compton camera

Gamma-ray imagers based on Compton scattering principle, which is also called "electronically collimator" have been attracting the attention of scientists and re-

searchers for over forty years. The first Compton scattering device was proposed in 1973 by Schönfelder Volker, Hirner Andreas and Schneider K from the Max-Planck-Institut für Physik und Astrophysik in Germany to measure extraterrestrial gamma ray fluxes in the energy range 1-10 MeV [84]. This Conpton telescope was composed of two large plastic scintillator blocks, 1.20 m apart. The upper scintillator was of 15 $\times$ 15 $\times$ 15 cm^3 in dimension and consists of Nuplex 4 which had a light output 70% of anthracene, while the lower detector consisted of nine blocks of Nuplex 3, each 20 $\times$ 20 $\times$ 20 cm^3 in dimension. Gamma rays were detected by two successive Compton collisions in two large plastic scintillators, combined with a time of flight measurement. This telescope has directional sensitivity such that observable differences could be expected for points sources, galactic background, and the diffuse gamma-ray spectrum, though it did not produce images. As a result the authors reported that the telescope had a half opening angle of 15° half width at half maximum(HWHM), an energy resolution of 20% (HWHM) and an absolute detection efficiency of about 0.5%. Meanwhile, the instrument performed an especially low response to undesired background gamma rays.

Two year later in 1975, design for a large double scatter telescope for gamma rays and neutrons was announced by researcher at Physics Department and Institute of Geophysics and Planetary Physics in the University of California, Riverside [85]. Still, this device was aimed to obtain directional sensitivity and not gamma-ray images. This telescope was developed for measurements of the flux, energy, angle and time distributions of gamma rays and neutrons from a balloon. It was sensitive to gamma rays from 0.5 to 30 MeV and to neutrons from 2 to 100 MeV. A gamma-ray was identified by Compton scatters in each of two large liquid scintillator tanks of cross section 1 m $\times$ 1 m spaced 1 m apart. Time of flight measurements separated the gamma rays from the neutrons and determines their direction through the telescope. Instead directly using the energy losses of the scattered gamma ray in the second

detector as its total energy in the design of Schönfelder Volker et al., a correction factor was applied to estimate the initial gamma-ray energy based on the observed energy losses and interaction positions. For point sources the gamma ray detection efficiency was a maximum of 3% at 4 MeV and dropped to 1% at 0.5 MeV and 0.4% at 30 MeV, while for a neutron point source, its peak efficiency was 8% at 6 MeV and fell rapidly to 1% at 3 MeV and slowly to 0.4% at 100 MeV. For the large cells the gamma ray and neutron energy resolutions were both about 20% HWHM for the useful energies, and the cone angle resolutions were about 10° HWHM. Energy resolution of 25% HWHM at 2.2 MeV and 20% HWHM at 4.4 MeV was identified by simulations. Angular resolution was estimated around 8° HWHM with a maximum file of view of about π steradian.

In 1974, the concept of Compton imaging devices was firstly proposed by Todd et al. from the University of Southampton in United Kingdom as a alternative to a mechanically collimated imaging system which could only achieve two-dimensional images [86]. They are the first to report that a gamma ray source distribution image can be obtained vis measuring the energy depositions and interaction positions of the two consecutive interactions. They also recognized that a number of practical problems including the determination of the sequence of interactions, the removal of spurious data by time coincidence methods, amplification of a large amount of low intensity pulses, and detector fabrication arose in order to produce promise images. Soon, they reported their first design for a gamma-ray imager based on Compton effect [87]. A segmented semiconductor detector which was able to locate successive interaction points in multi-collision trajectories and the associated energy losses was employed in this design. In this publication, based on a computation method, the statistical spread of a point source, was determined. They also discussed the possibility of preprocessing the basic detector data to improve the image.

In 1983, Manbir Singh and David Doria at the Institute for Physics and Imaging

Science in the University of Southern California announced the first working Compton imaging system [88, 89]. In [88], the authors performed the detector optimization studies based on a prototype system consisting of a cryogenically cooled 33 × 33 array of 5 × 5 mm^2 semiconducting detection elements placed in front of an uncollimated conventional scintillation camera. The authors reported that germanium would be the preferred semiconducting material for imaging in the 140-511 keV range, and that its optimal thickness at 140 keV was 6 mm. In [89], iterative algorithms was investigated for reconstructing images from data obtained using a cylindrical 6 mm diameter × 6 mm thick high purity germanium(HPGe) front-plane separated by 5 cm from an uncollimated NaI scintillation detector in the back plane. A two stage approach in which line projection images were reconstructed from the conical surface samples in the first stage, and tomographic images were reconstructed in the second stage, was studied by computer simulation. Three dimensional tomographic and 2-D planar images were obtained using the fist stage reconstruction procedure. These images experimentally demonstrate, for the first time, the feasibility of Compton imaging system based on Compton scattering principle.

Five years later, R. Ricardo Brechner and Manbir Singh discussed the comparison of above Compton imaging system("electronically collimated system") and a mechanical cone-beam system for imaging single photons through analytical study in [90]. They reported a factor of 62 gain in the counting sensitivity of the Compton imaging system at 140 keV for a 25 cm diameter sphere compared with a cone-beam collimated system. They also pointed out that the electronically collimated system could achieve the same signal to noise ratio as the cone-beam collimated system in less than 10% of the counting time through comparative computer simulated studies of noise propagation in the tomographic reconstruction from cone-beam projections for both systems.

The early successes of the Compton imaging system encouraged Schönfelder to

lead a international team of scientists to design, develop, fabricate and evaluate the first Compton telescope, COMPTEL, which was one of the four instruments selected for flight on the Gamma Ray Observatory(GRO) mission of NASA in the late 1980's. In a publication in 1988 in IEEE Transactions on Nuclear Science [91], the group introduced the design requirements for COMPTEL, its principles of operations, and described its properties and results from calibration of a Science Model. The front detector assembly consisted of seven liquid scintillator cells each of which was 28 cm in diameter by 8.5 cm deep and viewed by eight EMI 9755NA photomultiplier tubes. The back detector assembly consisted of fourteen NaI scintillators, each 28 cm in diameter by 7.5 cm in depth and viewed by seven EMI 9754NA photomultipliers. Due to the large separation between the two assemblies (over 2 m), the spatial resolution was 3.53 cm FWHM at 1.0 MeV, 2.83 cm FWHM at 2.7 Mev in the front detector array, and 5.89 cm FWHM at 0.5 MeV, 3.30 cm FWHM at 1.3 MeV in the back detector array. The energy resolution was measured 12% FWHM at 511 keV, 8% FWHM at 1.28 MeV and 6% FWHM at 2.75 MeV. The angular resolution was also calculated to be 4.7° FWHM at 1.2 MeV and 3.06° FWHM at 2.75 MeV. The authors announced that COMPTEL was capable of exploring the relatively unknown sky in the energy 1-30 MeV at a sensitivity level far exceeding any previous observations.

COMPTEL had the highest sensitivity among astronomical gamma-ray detectors in the 1-30 MeV range, at the time of its flight. However, the efficiency and angular resolution of the system were abysmal by medical imaging standards. Therefore, different configurations were investigated to maximize the efficiency of such systems while enhancing the angular resolution. In 1988, T. Kamae and N. Hanada from the University of Tokyo in Japan proposed an new design for an Compton scatter imager consisting of a stack of 500 layers of 6 mm $\times$ 6 mm in area and 500 μm in thickness 2-dimensional silicon strip detectors surrounded by a side counter made of CsI(Tl) [92]. The CsI(Tl) scintillator was cylindrical with 10 cm in inner radius, 18 cm in

height, and 2 cm in thickness. Thanks for the increasing off the solid angle subtended by the back plane detector, the efficiency of the device was therefore largely increased. They reported that a total intrinsic efficiency near 20% for a simulated beam source with energy less than 500 keV has been achieved. An angular resolution of 3∼5.5° FWHM when the initial gamma-ray energy was known was also obtained. Christopher John Solomon and Robert John Ott at the Institute of Cancer Research and The Royal Marsden Hospital declared that germanium and silicon were feasible scattering detectors based on sensitivity, absorption, and position resolution characteristics [93]. In their study, only high atomic number scintillators were considered for the second plane detector. It should be noted that by the late 1980s, pixellated anode structures had not yet been used with semiconductor detectors. At a result, semiconductors with poor charge carrier transport properties were not considered feasible for these devices.

Throughout the 1980s and 1990, more scientists and researchers paid attention to silicon, germanium, CdTe, and CdZnTe detectors as possible candidates for Compton imaging systems due to the fast improvements of semiconductor detectors in this period. In 1990, Dogan, N et al. at the Department of Nuclear Engineering in the University of Michigan investigated a compact, multiple layered, Compton scattering gamma ray imaging camera for technological feasiblity [94]. Beginning from Kamea and Hanada's work, the multiple Compton scattering camera utilised stacks of a series of large area thin silicon (or germanium) detectors surrounded by a CsI(Tl) scintillation detector. Each layer was designed to be an independent, two dimensional, position sensitive detector. The layers were sufficiently thin so the probability of multiple interactions in any layer was small. This was the first demonstration of using multiply scattered gamma rays to reconstruct images. Monte Carlo simulations yielded reconstruction efficiencies of 7-14% for silicon and 16-28% for germanium detectors. Including anticipated experimental errors, they obtained angular errors of ∼2-5° in

the reconstructed incident gamma ray directions over the energy range of interest. In [95], this group optimized the layer thickness to be less than 2 mm for 150-511 keV incident gamma rays and approximately 4 mm for 1 MeV gamma rays through Monte Carlo simulations. Based on the optimization, the authors announced the efficiency and the angular resolution of a proposed multiple Compton scatter imaging camera consisting of 1 mm thick, 20 layer silicon strip detectors surrounded with an annular CsI side counter. Based on Monte Carlo simulations, an angular resolutions of 2-7° FWHM assuming a 1 keV noise source with intrinsic efficiencies of 2.5-22% over the energy range of 150-1000 keV was reported. Although the angular resolutions obtained were rather modest, the detection efficiency was very encouraging. This high efficiency shows that the multiple Compton scatter camera could be particularly useful for imaging weak radiation sources, and minimizing image acquisition time.

A ring Compton scatter camera for imaging medium energy gamma rays was proposed by J.B. Martin et al. in 1993 [83]. This detector consisted of two position sensitive detector arrays: a 4 × 4 planar array of 5 mm × 5 mm × 6 mm Ge detectors as the first detector and a ring array of up to 64 NaI(Tl) crystals as the seconde detector. In the second array, each NaI element was a right circular cylinder, 19.1 mm in diameter and 50.8 mm in length. Past evaluations of Compton cameras usually employed a planar second detector, which was subjected to a large flux of gamma rays that either passed directly through or underwent small angle scatter in the first detector. Direct and small angle scattered events in the second detector could be significantly reduced by employing a ring array. Observed Compton central scattering angle could be varied by moving the Ge detector array alont the axis of the NaI(Tl) ring. In point spread functions generated with a simple back projection algorithm, the angular resolution was about 9° FWHM and the intrinsic efficiency is measured to be 0.015% when the central scattering angle was set to be 45°.

In 1995, T. J. O'Neill et al. from the University of California, Riverside reported

a system similar to those proposed by Kamae and Hanada and by Dogan, Wehe, and Knoll [81]. The Tracking and Imaging Gamma-Ray Experiment (TIGRE) was designed to observe cosmic gamma ray sources at energies of 0.3 to 100 MeV. Its major feature was its use of multi-layer silicon strip detectors to track Compton recoil electrons and positron-electron pairs. It used 7 double sided silicon strip detectors 3.2 cm $\times$ 3.2 cm $\times$ 300 μm with 1 mm pitch in the both x and y coordinates. The direction and energy of the Compton scattered gamma ray was measured with small CsI(Tl) photodiode detectors consisting of 36 CsI(Tl) crystals of 1 cm $\times$ 1 cm $\times$ 1.7 cm. Knowing the energy and momentum of the scattered electron and scattered photon allowed them to determine the incident direction uniquely and thus eliminated the azimuthal uncertainty in the back projected images, resulting in a ray but not in a cone. Total energy resolutions at 511 and 900 keV were measured to be 11% and 8.9% FWHM respectively. They reported angular uncertainties 10° FWHM at 900 keV and 11° FWHM at 511 keV.

In 1996, B.F.Phlip et al. announced the performance of a Compton telescope using position-sensitive planar germanium detectors. They created a telescope with 625 $\times$ 25 pixels combinations by combining a 25 $\times$ 25 strip (2 mm pitch) detector with a 5 $\times$ 5 strip detector (9 mm pitch). The 25 $\times$ 25 strip detector was positioned vertically in a cryostat whereas the 5 $\times$ 5 strip detector was horizontal. The vertical detector was placed 40 -150 cm in front of the horizontal detector. This Compton camera achieved an excellent energy resolution of 0.5% at 662 keV and angular resolution $\sim$1° FWHM. The angular resolution could be further improved by using detectors with small pixels for both of the detectors.

In 1997, J.E. Gormley et al. performed a direct simultaneous experimental comparison between electronic collimation and mechanical collimation. The authors examined the relative performance of these two techniques at the medium gamma-ray energies 0.1-1 MeV [96]. They built a mechanically collimated (pinhole) camera and

compared its performance to an electronically collimated camera. Planar radioactive sources were applied and imaged simultaneously by both cameras for identical periods of real time. The authors presented data for several radioactive sources of different energies and shapes. Results using an iterative image reconstruction techniques showed that the mechanical collimated device had a better performance at the lowest energy examined, 279 keV, while for energies above 400 keV, the electronically collimated device performed better.

In the same year, Alexander I. Bolozdynya et al. reported a new attempt, using a gaseous high pressure xenon to build a Compton camera [97], although theoretical study had been done 10 years ago by Ichiro Fujieda and Victor Perez-Mendez [98]. The high pressure xenon gas electroluminescent chamber had an optical readout which was not affected by the capacitance of the electrode structure, and used a small amount of readout channels over a large field of view, compared with ionization and semiconductor detectors. The electroluminescent detector also had a low detection threshold ($\sim$1 keV) and good energy resolution in low energy range because of intrinsic light-amplification. The imager consisted of a cylindrical pressure chamber with a low electric field drift region and a high electric field electroluminescent region. Two dimensional interaction positions were measured by position-sensitive photomultipliers and the delay time between the signals generated by the original scintillation and the electroluminescence was used to estimated the third coordinate. A spatial resolution of 25 mm was obtained for a 140 keV point-like source placed 10.5 cm in front of the camera without any collimator. This corresponded to an angular resolution of 13.6° FWHM.

In [99], researchers from the University of Michigan reported the C-SPRINT camera, a prototype Compton imager for low energy gamma rays. It consisted of a single $3 \times 3 \times 0.1$ cm^3 silicon pad detector module centered at the front face of a SPRINT detector system. The silicon pad detector was pixellated into a 22×22

array of 1.2 × 1.2 mm^2 elements while the SPRINT detector system was made of 11 modules arranged in a 50 cm diameter, 10 cm long cylinder. Each module was composed of an array of 1.27 cm in thickness NaI bars viewed by 20 photomultiplier tubes that provided and intrinsic spatial resolution of 3 mm at ^{99m}Tc energy (140.5 keV). The energy resolution for the silicon detectors was 1 keV FWHM. Simulations using this setup showed angular uncertainties of 4.1° and 2.2° FWHM for ^{99m}Tc and ^{131}I point sources, corresponding to spatial resolution of 7.2 mm and 3.8 mm at 10 cm, respectively.

In 1996, E. Aprile et al. built the first Liquid Xenon Gamma-Ray Imaging Telescope (LXe-GRIT) for medium energy astrophysics based on a liquid xenon time projection chamber (LXe-TPC) with a total volume of 10 liters and a sensitive area of 20 cm × 20 cm [100]. The LXe-TPC, which was sensitive to gamma-rays from 300 keV to 30 MeV, measured the energy and the 3-D position of each gamma-ray interaction with a resolution of 6% FWHM and 2.4 mm FWHM at 1 MeV. Its detection efficiency for Compton events was about 4% in the energy range 1—3 MeV, whcih was an energy band of great astrophysical interest for both continuum and line emission. The image accuracy could be as good as 1°. In [101], another design with a total geometrical area of 2500 cm^2 in a single pressure vessel was proposed. In this Compton telescope configuration, two LXeTPC assemblies were employed, of which the upper assembly was composed of 4 modules while the lower assembly was composed of 4 towers of 4 modules. Each module was with 25 cm × 25 cm sensitive area. the separation was 10 cm. The angular resolution for this setup was estimated to be 0.94°-5.65° FWHM over the 120° field of view.

In 2001, Y.F. Du et al. from the University of Michigan, reported an evaluation for an prototype Compton scattering camera using 3-D position sensitive CdZnTe detectors [102, 103]. The imager was based on two 1 cm^3 cubic 3-D position sensitive CdZnTe detector. There were 11 × 11 pixels on each anod surface. The authors

analysed the energy resolution, angular resolution and the efficiency of the camera. The angular resolution was estimated to be 3°-4° for 511 keV gamma rays within a ±30° field of view, and enhanced to 2° at 1 MeV, when the central scatter angle was set to be 50° and separation between the two detectors 5 cm. The intrinsic efficiency of the camera was between 1.5×10^{-4} and 8.8×10^{-6} for 511 keV to 3 MeV.

In the same year, G.J. Schmid et al. proposed another design using segmented HPGe to image gamma rays [79]. A 5 cm × 5 cm pure coaxial HPGe was applied to develop a Compton camera imager. This work was the first attempt to use a single crystal for 4π Compton imaging. The potential efficiency gain associated with this new design was estimated to be about 1 order of magnitude. The position sensitivity of the crystal was achieved by segmenting the outer contact, and performing digital pulse shape analysis on all the signals for all the events. As a result, the authors declared that it was possible to determine the location of single-site interactions at 374 keV to better than 1 mm. Experimental and theoretical imaging studies were performed using the Gamma-Ray Energy Tracking Array (GRETA) [104] and results showed a high noise level was inhibiting the imaging performance at 186 keV and 244 keV. Although the attempt failed to gain the source location, the authors suggested that it seemed possible if noise levels a factor of seven below the GRETA prototype could be achieved.

E. A. Wulf et al. demonstrated the ability to identify the depth of a gamma-ray interaction point over the full active volume of a thick germanium double-sided strip detector which was capable of performing Compton imaging [105]. The detector used for this device was a 25 × 25germanium orthogonal strip detector with 2 mm strip pitch. It was 5 cm × 5 cm × 1.1 cm in size. It was with lithium strips held at +1.5 kV bias potential that collect electrons and boron strips on the rear face to collect the holes. Orthogonal strips on the front and opposite faces of the crystal allowed germanium strip detectors to locate a gamma-ray interaction in two dimensions with

an accuracy equal to the width of the strips. The intersection of the triggered strips on opposite sides of the detector determined its position. The interaction depth was estimated by the timing difference between signals from collection of electrons and holes. The position resolution in the depth direction was measured to be less than 0.5 mm. The reported angular resolution was 7° FWHM. Although only planar images were obtained, this attempt experimentally, for the first time, demonstrated the feasibility of Compton imaging using a single crystal. One year later, the three-Compton technique, where gamma rays were not required to transmit its full energy in the detectors as long as three interactions occurred, was demonstrated using two detectors by this group [106].

In 2003, F. Lebrun et al. presented a Compton cube, a 4π gamma-ray telescope operating in the energy range of 100 keV to 2 MeV on board a microsatellite for the study extragalactic phenomena and interstellar emission [107]. Considering the constraints of the weight, size and power consumption, the authors proposed to employ six gamma cameras, each having 32 $\times$ 32 pixels of 4 mm $\times$ 4 mm planar CdTe or CdZnTe detectors arranged inside of the Cube. The printed circuit board with the front-end electronics were on the outside of the cube. The reported energy resolution of the detectors was below 1.5% at 100 keV to 1 MeV. They also estimated the angular resolution around 4°-2.5° FWHM in the same energy range, although it was not clear whether they have considered Doppler broadening effect in the estimation. The uniqueness of this design was that any detector array could be used as the front or back plane. Therefore, the field of view was much larger than other geometries. However, the authors did not discuss how to properly reconstruct the sequence of each observed event.

Researchers from Kyoto University proposed a Compton imaging system based on a gaseous time projection chamber with Micro Pixel Chamber(Micro-TPC) [108]. In this design, a gas chamber was used as the scatter detector and a scintillation

detector, enclosing half volume of the gas chamber, was used to absorb the scatter photon. The Micro-TPC consisted of the μ-PIC, which has pixel type electrodes arranged perpendicular to each other with 400 μm spacing, and this enabled it to measure the fine tracks of electrons in Compton scattering. The estimated angular resolution on the order of 15° FWHM and intrinsic efficiency between 1% and 0.1% between 100 keV and 2 MeV were achieved using Monte Carlo simulation.

In 2004, Lisha Zhang et al. from the University of Michigan, reported a Compton camera for high performance scintimammography [109]. This imager was a dual-head camera composed of two silicon detectors, each composed of a stack of 1 mm thick 10 cm $\times$ 10 cm pixellated silicon detectors and followed by a 40 cm wide, 40 cm deep and 2 cm thick NaI scintillation detector with a 3 mm FWHM intrinsic resolution, respectively. Using Monte Carlo simulation, they demonstrated that the proposed technique could achieve an absolute detection efficiency of 0.03 and a spatial resolution of 3.8 mm FWHM at 141 keV photon energy using 5 mm thick silicon detectors for point sources which was 2.5 cm deep in a 5 cm thick breast phantom.

In 2004, Takefumi Mitani et al. proposed a prototype Si/CdTe Compton camera using a double sided Si strip detectors (DSSDs)as the scatterer and two CdTe pixel detectors as the absorber [110]. Later in 2005, the same group reported the imaging performance of a second prototype Si/CdTe Compton camera with another design in [111]. This second prototype consisted of six layered DSSDs as the scatterer, each with an area of 2.56 cm $\times$ 2.56 cm and thickness of 300 μm, and three 8 $\times$ 8 CdTe pixel detectors as the absorber, with dimensions of 18.55 mm $\times$ 18.55 mm and thickness of 500 μm. The author reported that energy resolutions of 9.1 keV and 12 keV were obtained at 356 keV and 511 keV respectively. An angular resolution of 3.9° FWHM was also presented. It should be note that, this research team have been developing Si/CdTe Compton cameras and many publication on this work have been reported. The detector concept was adopted as the key technology for the Hard X-

ray Imager(HXI) and the Soft Gamma-ray Detector on board the ASTRO-H X-Ray observatory, which was scheduled fo lauch in 2014 [112].

In the same year, Dan Xu et al. from the University of Michigan proposed another 4π Compton imaging with single 3-D position sensitive CdZnTe detector [113]. The single CdZnTe crystal used in this work was 15 mm $\times$ 15 mm $\times$ 10 mm in dimension and its anode was pixellated into an 11 $\times$ 11 array. The depth information was achieved by measuring the electron drift time from the interaction positions to the anodes. The authors announced that the position resolution at the time was about 1.2 mm in each direction, and the energy resolution was 1.1% and 1.6% for single and double pixel events at 662 keV. They also discussed and compared different algorithms for sequence and imaging reconstruction. Angular resolutions of 10° and 19° were realized using list mode MLEM reconstruction algorithm after 24 iterations and filtered back projection, respectively. In [114], thsi group reported the progress using the same detector under a weighted list mode MLEM reconstruction algorithm. An measured intrinsic efficiency of nearly 2% as well as an angular resolution of 17° FWHM at 662 keV after 10 iterations have been achieved. The 3-D position sensitive CdZnTe detector for Compton imaging is still drawing the attention of this group currently.

In 2009, Mark Amman et al. reported the High Efficiency Multimode Imager(HEMI) [115], which was developed for the purpose of detecting, locating, and spectroscopically characterizing gamma-ray emitters at long-range standoff distances. HEMI was composed of CdZnTe coplanar-grid detectors which were arrayed to form an imaging device that employed both coded aperture and Compton imaging simultaneously. In the design of this instrument, the back plane was fully populated with 8 $\times$ 8 CdZnTe crystals, while the front plane was only partially populated with 32 CdZnTe crystals. All the CdZnTe crystals were with the same size, 1 cm $\times$ 1 cm $\times$ 1 cm. The energy resolution was shown to be sub-2% FWHM at 662 keV. In [116],

Michelle Galloway et al. presented the simulated and measured response of the HEMI. An angular resolution of 11° was estimated using list mode MLEM reconstruction algorithm after 5 iterations for a 24-detector array HEMI.

In 2011, Kai Vetter et al. firstly proposed the demonstration of electron-tracking for Compton imaging in solid-state detectors using a 650 μm thick and fully depleted Si-based charge couple device (CCD) with 10.5 μm pixel size and an energy resolution of 570 eV at energy of 60 keV [117]. Similar to the work done by Kyoto University group, through measuring the initial direction of the Compton-scattered electron, which was deduced by analyzing the electron energy loss measured on the pixelated readout, the authors reported that they could reconstruct the gamma ray origin on an arc instead of a Compton cone. In [118], they described the procedure to deduce the three-dimensional electron-scattering direction, while in [119], the gain and impact of electron-tracking based Compton imaging over conventional Compton imaging were presented. The results showed this device could reduce the Compton cone to approximately ±30° for 662 keV incident photons, which resulted in a reduction in the background by a factor of 6.

In 2013, a handy Compton camera using 3D position sensitive scintillators were developed by J. Kataoka et al [37]. This device employed two 50 × 50 arrays of 1 mm × 1 mm × 10 mm inorganic Ce-doped $Gd_3Al_2Ga_3O_{12}$ crystals both as scatter and absorber. It was aimed to identify radioactive hotspots in Fukushima to ensure effective decontamination. The first prototype was only 1.5 kg in weight. The sensitivity was reported to be ∼1% at 662 keV. Using list mode MLEM reconstruction algorithm, an angular uncertainty of 14° FWHM at 662 keV without DOI information was achieved.

There are many other meaningful works on Compton imaging which are not included above. For example, combination of coded aperture with Compton camera to achieve better angular resolution proposed by L.E. Smith et al. [120–122],

a gaseous Compton imager using 2D-sensitive gaseous photomultiplier to compete with the standard Anger Camera reported by C.D.R. Azevedo et al. [123], the first Compton telescope prototype based on continuous $LaBr_3$-SiPM detectors developed by G.Llosá et al. for dose monitoring during irradiation in hadron therapy [124], and a prototype Compton camera array consisting of four PVT and four NaI(Tl) scintillation detecotrs with PMT readout for localization and identification of remote radiation sources reported by Y. Kong et al. [125]. Compton imagers have also been applied to various areas, from prostate imaging [126] to nuclear materials inspection [79], to environmental monitoring [127]. To assess the practicality of using Compton imaging for any application, it is necessary to make clear how the parameters and configurations could effect the performance of a Compton camera.

2.4.3 Angular Resolution of Compton camera

As illustrated in Figure 1.4 and from Equation 2.2, Compton scattering angle is determined by the initial energy and the energy deposited in the scatter. Therefore, the uncertainty of the energy measurement, either due to the detector's energy resolution or the Doppler broadening effect, will contribute to the resolution of scattering angle θ. Since the axis of the back-projected cone is determined by the interaction positions in the two detector arrays, the accuracy of the position measurements will also contribute to the angular resolution. The overall angular resolution is the quadratic summation of these three components, as long as each component is a Gaussian distribution and independent of each other.

$$(\Delta\theta)^2 = (\Delta\theta_{energy})^2 + (\Delta\theta_{geometry})^2 + (\Delta\theta_{Doppler})^2 \tag{2.3}$$

Here, $\Delta\theta$ is the total angular resolution, $\Delta\theta_{energy}$ is the contribution from the detector energy resolution, $\Delta\theta_{geometry}$ is the contribution from uncertainty of the interaction

position measurement, and $\Delta\theta_{Doppler}$ is the contribution from the Doppler broadening effect. Quantitative analysis of each component is presented below.

2.4.3.1 Energy Resolution Contribution

In Compton scatter imaging, an effective event used for reconstruction must be that the initial photon only undergoes one scatter in the first detector then the scattered photon escapes the first the detector and interacts with the second detector. Usually, the initial energy of the incident photon is unknown, therefor we have to assume that the scattered gamma-ray deposits its full energy in the second detector in a photo electronic process. Then by replacing E_0 with E_s+E_a, the equation 2.2 can be written as below:

$$\cos\theta = 1 - m_0c^2\left(\frac{E_s}{E_a^2 + E_sE_a}\right) \tag{2.4}$$

Applying error propagation to equation 2.4, the angular resolution caused by the uncertainty of energy measurement is given by:

$$(\Delta\theta_{energy})^2 = \left(\frac{m_0c^2}{\sin\theta}\frac{1}{(E_s+E_a)^2}\Delta E_s\right)^2 + \left(\frac{m_0c^2}{\sin\theta}\left[\frac{1}{(E_s+E_a)^2} - \frac{1}{E_a^2}\right]\Delta E_a\right)^2 \tag{2.5}$$

In the above derivation, the scattered gamma-ray is assumed to deposit its full energy in the second detector which is not always true, especially for gamma-rays with a high and middle energy which have a higher probability to undergo another Compton scattering and only loss a part their energy. In such a case, the energy deposition in the second detector E_a is no longer equal to the scattered photon energy E_0-E_s. Therefore, the scattering angle calculated using equation 2.4 is not related to the true scattering angle. These events will only add background noise to the reconstructed image. A window is usually used for the summed energy spectrum to select full energy deposition events to eliminate the noise. In this case, instead of using the summed

energy to derive the scattering angle, the peak or the centroid energy(i.e. E_γ) of the summed spectrum can be used. Then equation 2.4 become:

$$\cos\theta = 1 - m_0c^2(\frac{E_s}{E_\gamma^2 - E_\gamma E_s}) \tag{2.6}$$

$$(\Delta\theta_{energy})^2 = \left(\frac{m_0c^2}{\sin\theta}\frac{1}{(E_\gamma - E_s)^2}\Delta E_s\right)^2 + \left(\frac{m_0c^2}{\sin\theta}\frac{E_s^2 - 2E_\gamma E_s}{(E_\gamma^2 - E_\gamma E_s)^2}\Delta E_\gamma\right)^2 \tag{2.7}$$

In equation 2.7, ΔE_γ is the error for E_γ, which only comes from the systematic calibration bias and is usually much smaller than the detector energy resolution. Thus, the angular resolution in equation 2.7 is dominated by the first term.

In some special cases, such as Single Photon Emission Computed Tomography(SPECT), where the initial energy of the incident gamma-ray is known, the energy resolution contribution is merely determined by the first detector energy resolution as below:

$$\Delta\theta_{energy} = \frac{m_0c^2}{\sin\theta}\frac{1}{(E_0 - E_s)^2}\Delta E_s \tag{2.8}$$

For GAGG(10 mm × 10 mm × 10 mm) crystal coupled to SiPM(KETEK, PM6660), the energy resolution FWHM at 59.5 keV, 122 keV, 356 keV, 511 keV and 662 keV is shown in Figure 2.7. A general relationship between the energy resolution and the deposited energy is estimated by $\Delta E = 0.045\times E + 9.01$ (keV) using a linear fitting. Using equation 2.8, the predicted angular resolution due to the uncertainty of first detector energy measurement for 60 keV, 122 keV, 356 keV, 511 keV and 662 keV is shown in Figure 2.8.

As shown in Figure 2.8, ΔE_{energy} decreases as the incident gamma-ray energy increases. For 662 keV gamma rays, ΔE_{energy} is smaller than 5° FWHM for scattering angle between 7° $\sim$ 66°. Therefore, this GAGG crystal is good enough for Compton

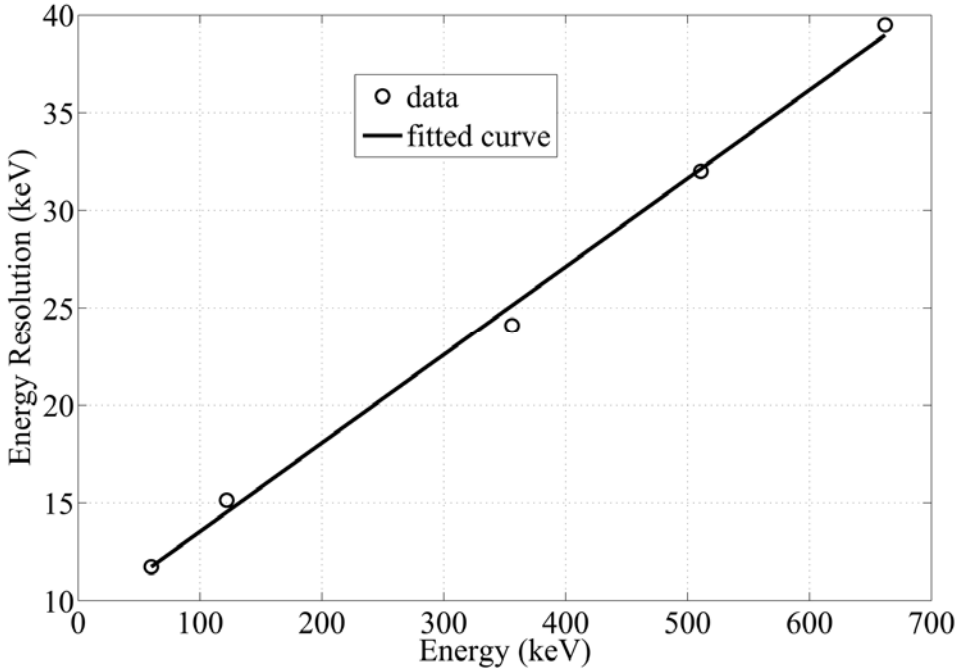

Figure 2.7: Energy resolution for GAGG(10 mm × 10 mm × 10 mm) crystal coupled to SiPM(KETEK, PM6660).

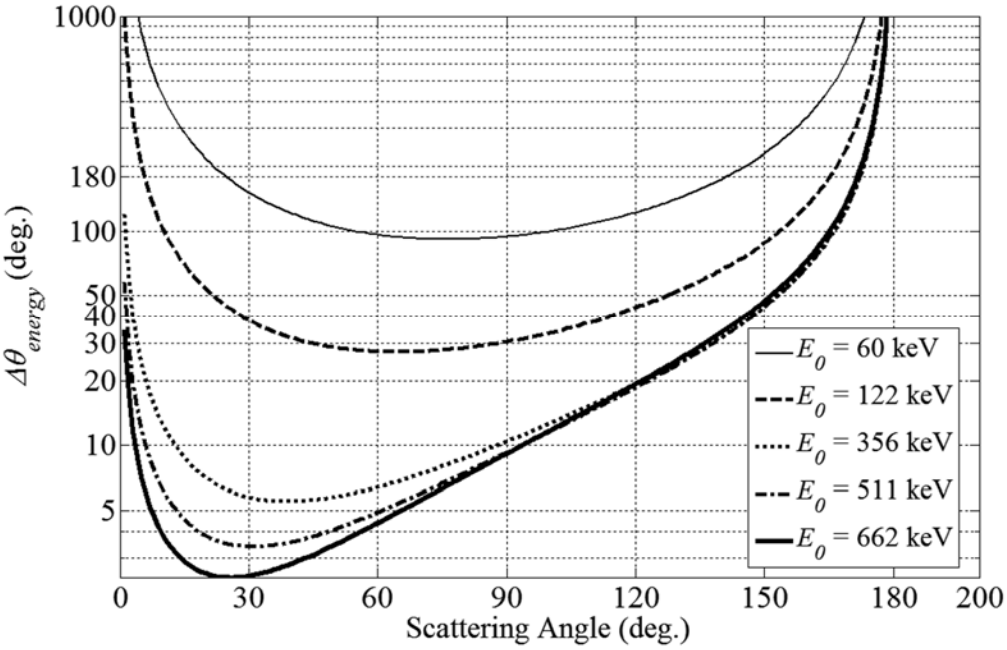

Figure 2.8: Angular resolution FWHM contributed by energy resolution.

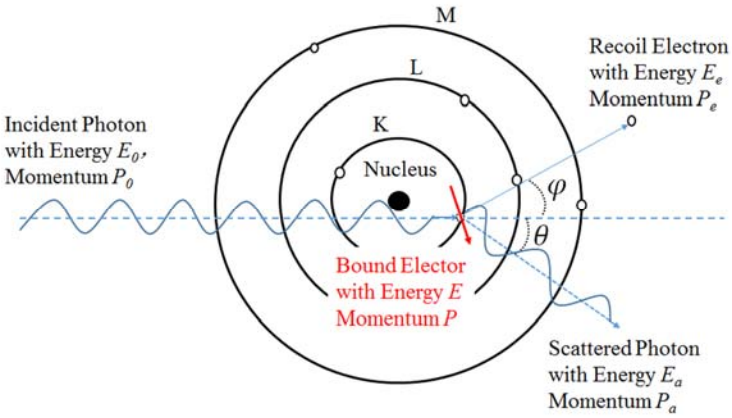

Figure 2.9: Compton scattering with a bound electron in reality.

scatter imaging for gamma-rays with energies 662 keV.

2.4.3.2 Doppler Broadening Contribution

The Compton scattering Kinematics, shown in Equation 2.2, is derived based on the assumption the the electron is at rest before the scattering interaction, But in reality, electrons are bound to nucleuses and have finite momenta. As shown in Figure 2.9, if the initial momentum $\mathbf{P}$ and energy E of a bound electron are included, from the conservation of the momentum and energy, we have

$$\begin{cases} \mathbf{P}_0 + \mathbf{P} = \mathbf{P}_e + \mathbf{P}_a \\ E_0 + E = E_e + E_a \end{cases} \tag{2.9}$$

In [128], Cooper and Malcolm gave the energy transferred to the electron by the incident photon as,

$$\begin{aligned} E_e &= \frac{\mid \Delta\mathbf{P} \mid^2}{2m_e} + \frac{\Delta\mathbf{P}_e \cdot \mathbf{P}}{m_e} \\ &= \frac{\mid \Delta\mathbf{P} \mid^2}{2m_e} + \frac{\mid \Delta\mathbf{P} \mid p_z}{m_e} \\ &= \frac{E_0^2 + E_a^2 - 2E_0E_acos\theta}{2m_ec^2} + \frac{p_z\sqrt{E_0^2 + E_a^2 - 2E_0E_acos\theta}}{m_ec} \end{aligned} \tag{2.10}$$

here, m_e is the electron mass, c is the velocity of light, $\Delta\mathbf{P}$ represents the scatter vector, which is the momentum difference between the scattered and incident photons and defined as $\mathbf{P}_a$-$\mathbf{P}_0$, and p_z is the initial electron momentum alone the scatter vector direction. In equation 2.10, the first part on the right side is the usual term given by Compton scattering kinematics, and the second part is the Doppler shift that is linear with respect to p_z and increases with incident energy E_0. As a result, the scattered photons energy is not merely decided by the scatter angle, θ, but also determined by the coupling between the initial electron momentum $\mathbf{P}$ and the scatter vector $\Delta\mathbf{P}$.

This Doppler broadening effect can be neglected when the incident gamma-ray energy is high enough, however, it deteriorates the angular resolution significantly in sub-MeV band. A more accurate Compton cross section than Klein-Nishina equation is given in order to performe a quantitative analysis of this effect.

In [129] in 1975, Ribberfors described the Compton differential cross section through a double differential cross section obtained from the relativistic impulse approximation (IA). A simplified equation using some first order approximation was done by Brusa et al. in [130]. They also proposed a parameterization of the Compton profile from which the simulation of Compton events can be carried out analytically by employing a few parameters that characterize the target atom, occupation numbers, namely shell ionization energies and maximum values of the one-electron Compton profiles. This method is used here to analyze Doppler broadening effect.

The Simplified Compton atomic double differential cross section obtained from IA is given by [130] as follow,

$$\frac{d^2\sigma}{dE_a d\Omega} = \left(\frac{d\sigma^{KN}}{d\Omega}\right) F(p_z) J(p_z) \frac{dp_z}{dE_a} \tag{2.11}$$

here,

$$\frac{d\sigma^{KN}}{d\Omega} = \frac{r_e^2}{2}\left(\frac{E_c}{E_0}\right)^2\left(\frac{E_c}{E_0} + \frac{E_0}{E_c} - sin^2\theta\right) \tag{2.12}$$

is the famous Klein-Nishina(KN) formula, where E_c is the scattered photon energy at scattering angle θ calculated by the normal Compton equation 2.2, r_e is the classical electron radius,. And $F(p_z)$ is defined as

$$F(p_z) = 1 + \frac{cp_c}{E_0}\left(1 + \frac{E_c(E_c - E_0 cos\theta)}{(cp_c)^2}\right)\frac{p_z}{m_e c} \tag{2.13}$$

here p_c is the momentum transfer,

$$p_c = \frac{1}{c}\sqrt{E_0^2 + E_c^2 - 2E_0E_c cos\theta} \tag{2.14}$$

The initial electron momentum alone the scatter vector direction, p_z is given by

$$p_z \equiv -\frac{\mathbf{P}\cdot\Delta\mathbf{P}}{\mid\Delta\mathbf{P}\mid} = \frac{E_0E_a(1-cos\theta) - m_ec^2(E_0 - E_a)}{c^2\mid\Delta\mathbf{P}\mid} \tag{2.15}$$

with

$$\mid\Delta\mathbf{P}\mid = \frac{1}{c}\sqrt{E_0^2 + E_a^2 - 2E_0E_a cos\theta} \tag{2.16}$$

if p_z=0, equation 2.15 turns to be the Compton scattering formula, equation 2.2. In a real atom, p_z distributed according to,

$$J_i(p_z) = \int\int \rho_i(\mathbf{P})dp_xdp_y \tag{2.17}$$

where $J_i(p_z)$ is the one-electron Compton profile in atomic shell i. Thus the atomic

Compton profile can be obtained through the sum of all electrons,

$$J(p_z) = \sum Z_i J_i(p_z) \tag{2.18}$$

here Z_i is the number of electrons in atomic shell i.

The Compton profile can be obtained in reference[131] and details of the Compton profile are not very important. In 1982 in [132], Ribberfors and Berggren proposed that the incoherent scattering functions that is defined as an integral over Compton profile can be computed in terms of a simple linear approximation. To minimize the required numerical information and simplify the random sampling, Brusa et al. reported the analytical one-electron profile as follow,

$$J_i^A(p_z) = \sqrt{2} J_{i,0} \left(\frac{1}{\sqrt{2}} + \sqrt{2} J_{i,0} \mid p_z \mid \right) \exp \left[\frac{1}{2} - \left(\frac{1}{\sqrt{2}} + \sqrt{2} J_{i,0} \mid p_z \mid \right)^2 \right] \tag{2.19}$$

here $J_{i,0}$ is the value of the Compton profile at $p_z = 0$ tabulated by Bigges et al. in [131].

Based on the discussing and analysis above, a simple Geant4 simulation was carried out to compute the energy broadening at different scattering angles with different incident gamma ray energies due to the Doppler broadening effect. Figure 2.10 shows the result of the simulation when the detector material is Silicon and the initial energies of the incident photon are 60 keV, 122 keV, 356 keV, 511 keV, and 662 keV. Figure 2.11 is the result of GAGG atom. The center energy for each scattering angle in Figure 2.10 and Figure 2.11 corresponds with the scattered photon energy derived from normal Compton equation 2.2, however, the distribution is broadening due to initial momenta of the electrons before interaction.

Angular resolutions contributed by Doppler broadening at different scattering angles are also calculated by applying the FWHM energy spread to equation 2.8. The result for Silicon detector and GAGG detector are show in Figure 2.12 and

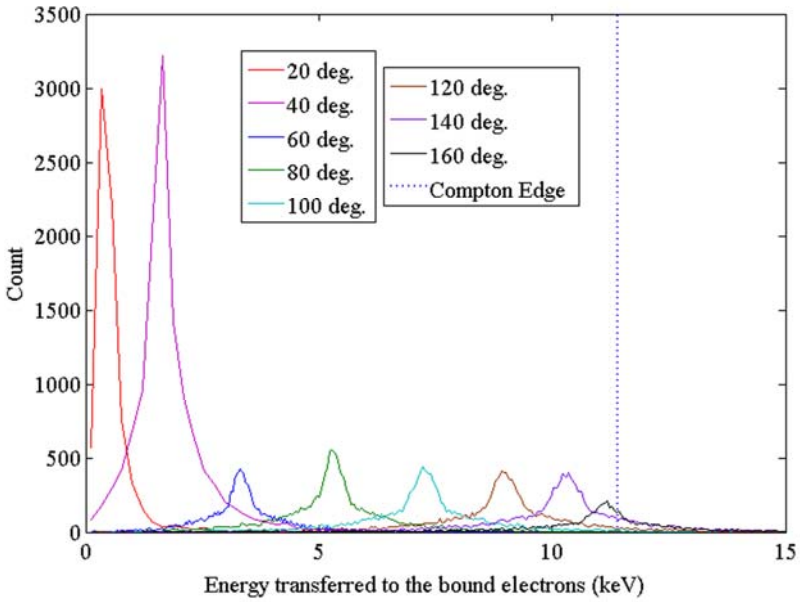

(a) Incident gamma-ray energy = 60 keV

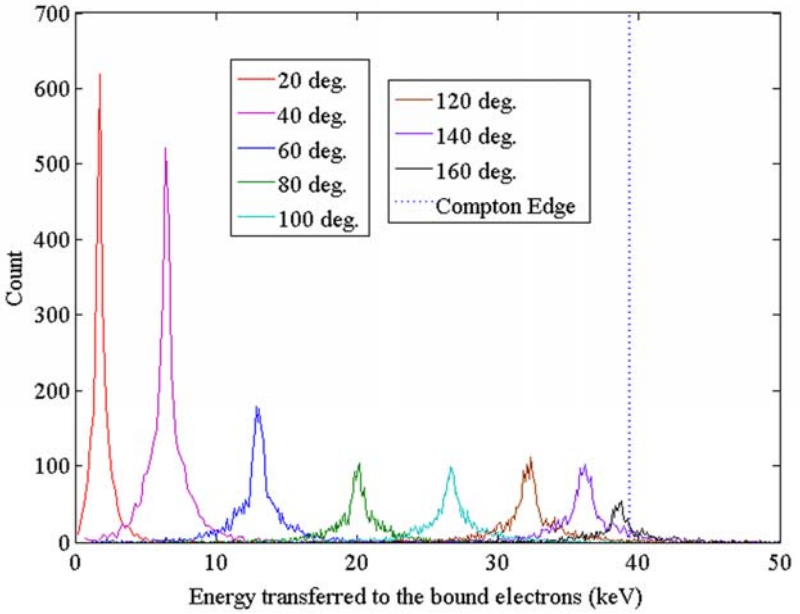

(b) Incident gamma-ray energy = 122 keV

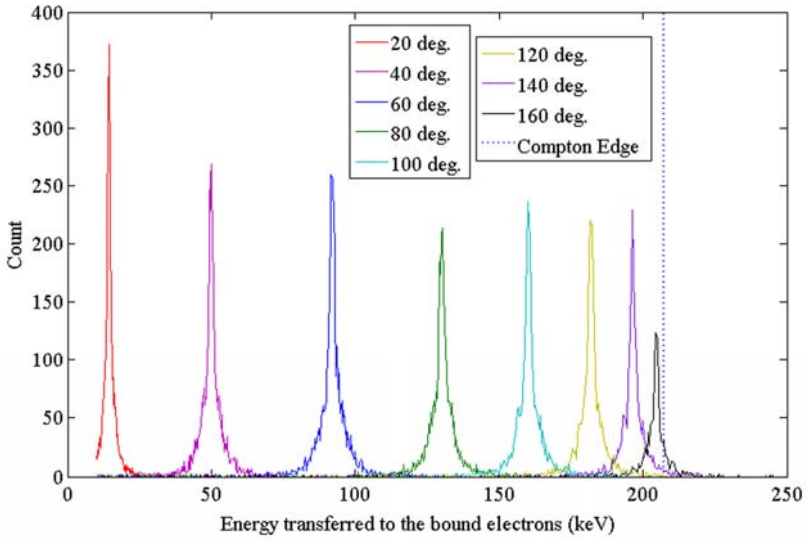

(c) Incident gamma-ray energy = 356 keV

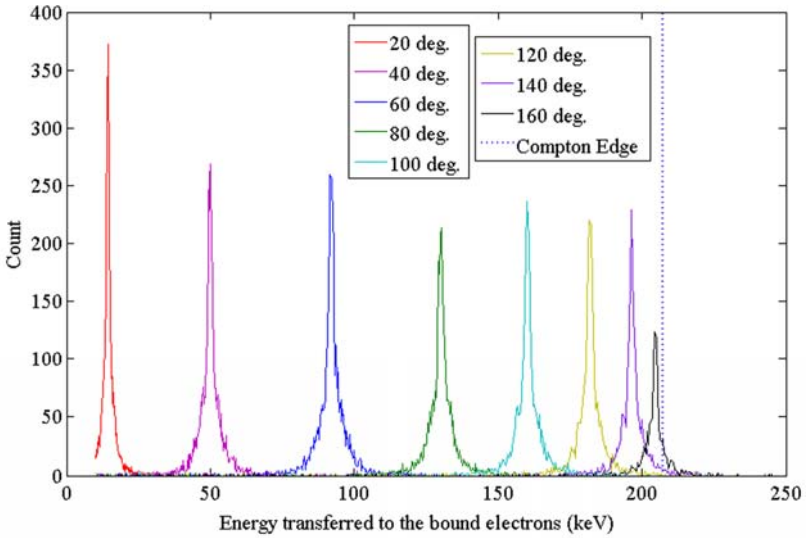

(d) Incident gamma-ray energy = 511 keV

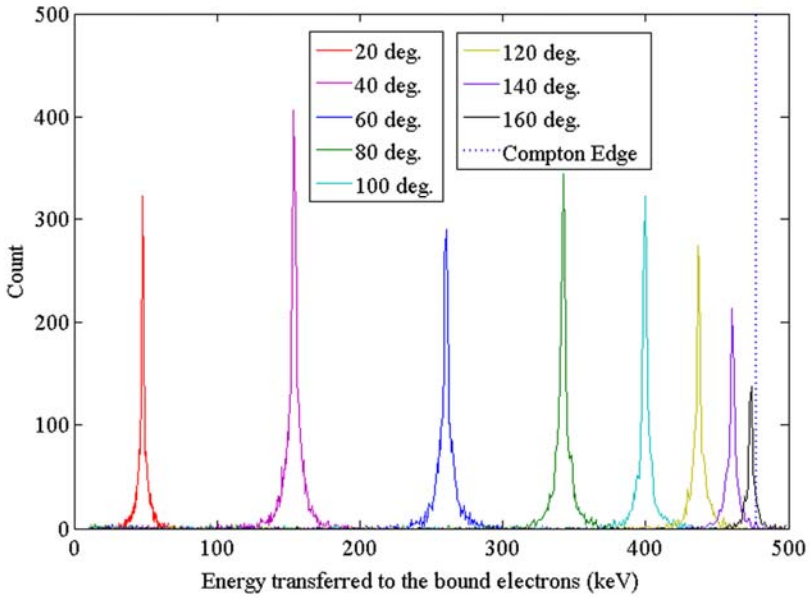

(e) Incident gamma-ray energy = 662 keV

Figure 2.10: Energy broadening at different scattering angles with different incident gamma-ray energies for Silicon atom. From Figure 2.11(a) to Figure 2.11(d), the incident gamma ray energies are 60 keV, 122 keV, 356 keV, 511 keV, and 662 keV. In a single figure, energy broadening at scattering angles of 20°, 40°, 60°, 80°, 100°, 120°, 140° and 160° are shown. The blue broken lines are the Compton edges for each incident gamma-ray energy.

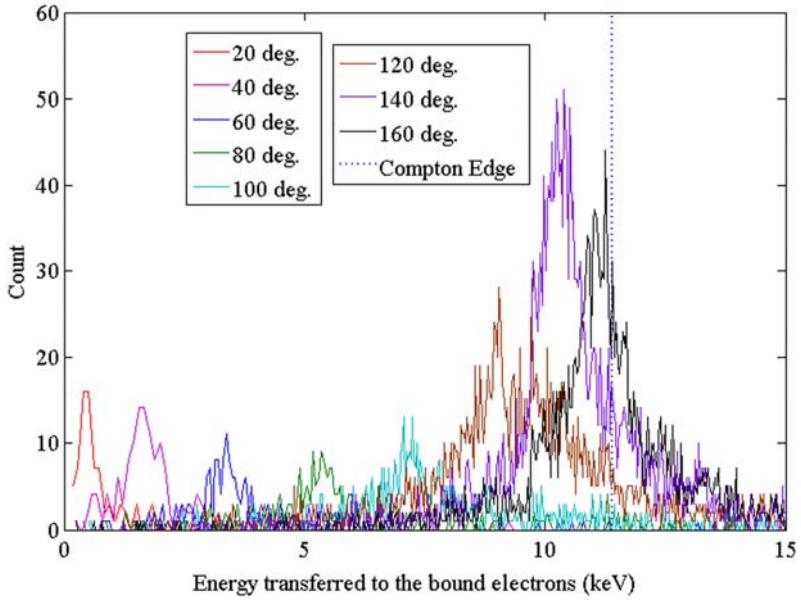

(a) Incident gamma-ray energy = 60 keV

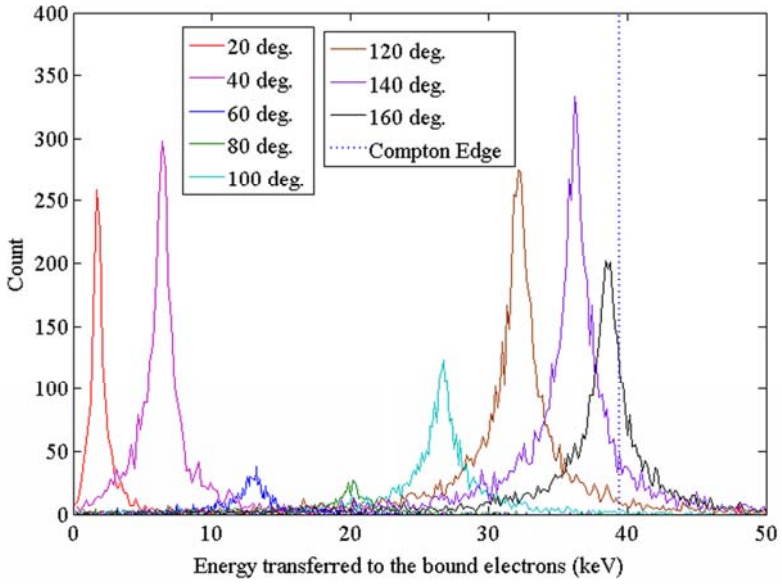

(b) Incident gamma-ray energy = 122 keV

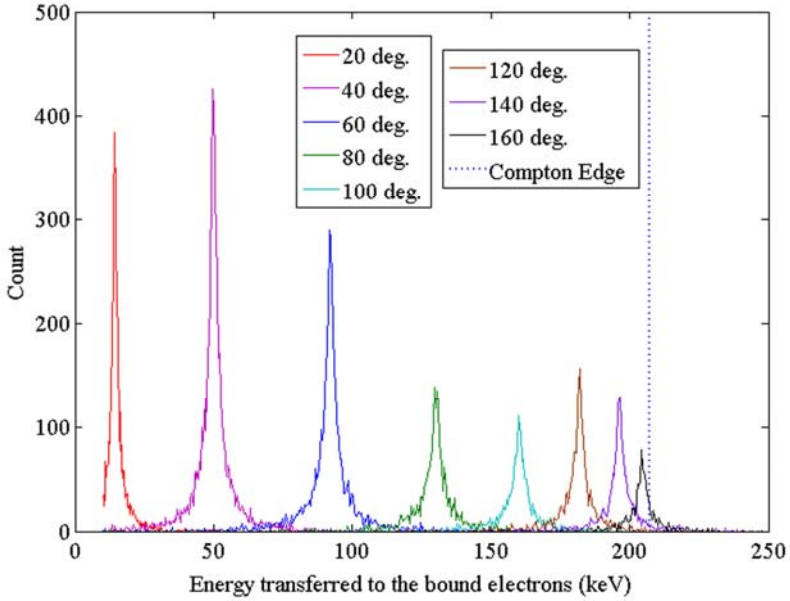

(c) Incident gamma-ray energy = 356 keV

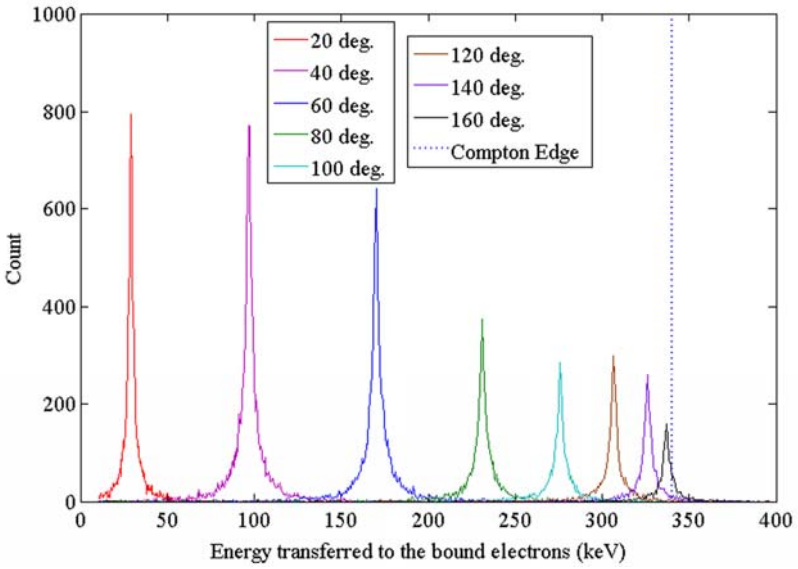

(d) Incident gamma-ray energy = 511 keV

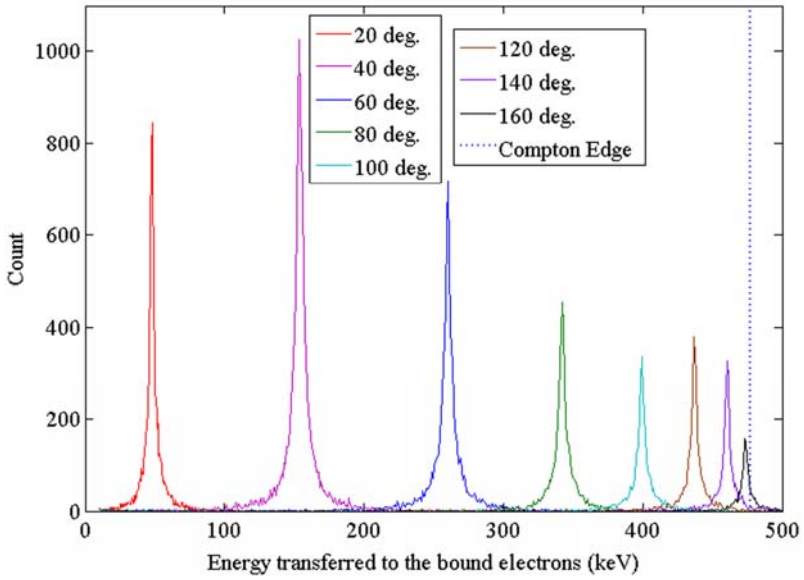

(e) Incident gamma-ray energy = 662 keV

Figure 2.11: Energy broadening at different scattering angles with different incident gamma-ray energies for GAGG atom. From Figure 2.11(a) to Figure 2.11(e), the incident gamma ray energies are 60 keV, 122 keV, 356 keV, 511 keV, and 662 keV. In a single figure, energy broadening at scattering angles of 20°, 40°, 60°, 80°, 100°, 120°, 140° and 160° are shown. The blue broken lines are the Compton edges for each incident gamma-ray energy.

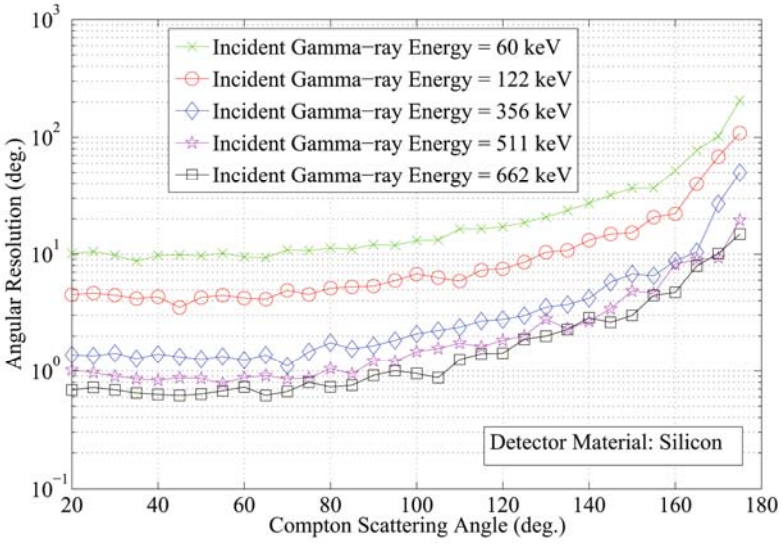

Figure 2.12: Angular resolutions FWHM contributed by Doppler broadening effect at different scattering angles with different incident gamma-ray energies for Silicon atom.

Figure 2.13, respectively. As shown in these two figures, Doppler broadening effect is tends to be more significant if the energy of the incident gamma ray becomes low and the scattering angle becomes large. A comparison of Silicon and GAGG are shown in Figure 2.14, from which, it is concluded that, Doppler broadening effect is emphasized when the atomic number of the detector material is getting higher. As shown in Figure 2.14(d), Doppler broadening contribution to the angular resolution is $\sim 1^\circ$ FWHM when the scattering angle is smaller than 80°.

2.4.3.3 Geometry Contribution

Because the axis of the back-projection Compton cone is determined by the two interaction position in the two detector planes, the position uncertainty introduces an uncertainty in the cone axis direction, which as a result, contributes to the angular resolution of the Compton camera [133]. These effects are shown in Figure 2.15. Two detector elements are shown as the yellow rectangular area. The distance between the central position of the two elements is $l=|\mathbf{O}_1\mathbf{O}_2|$. A point source is placed at

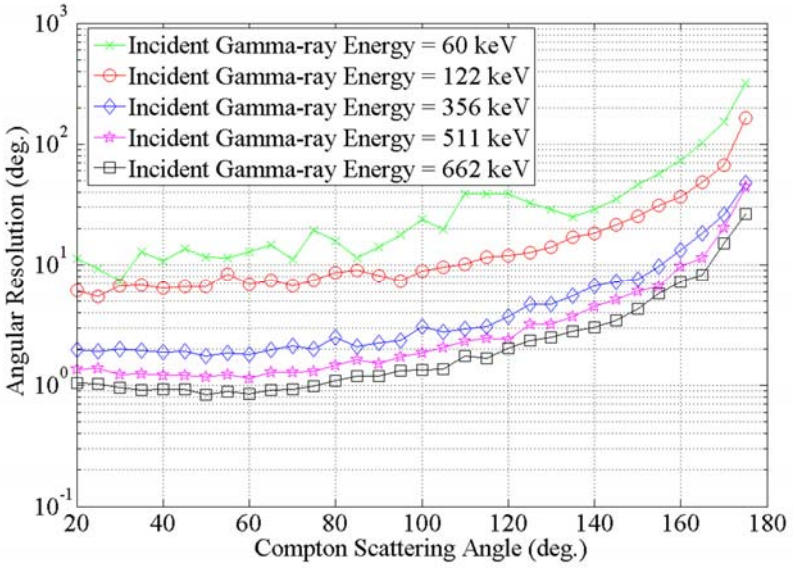

Figure 2.13: Angular resolutions FWHM contributed by Doppler broadening effect at different scattering angles with different incident gamma-ray energies for GAGG atom.

position S in front of the first element.

Angular resolution owing to the first detector lateral position resolution is illustrated in Figure 2.15(a). A gamma-ray emitted from the point source interacts with the first element at position A, which is the middle of the right edge, and then the scattered photon is absorbed at the center of the second element. The Compton scattering angle θ then is calculated as,

$$\cos\theta = \frac{\mathbf{SA} \cdot \mathbf{AO}_2}{|\,\mathbf{SA}\,| \cdot |\,\mathbf{AO}_2\,|} \tag{2.20}$$

In the back-projection, the interaction position A is not easy to be obtained, therefore, O_1, as a substitution, must be used. The back-projected source direction is $\mathbf{O_1S'}$, and

$$\cos\theta = \frac{\mathbf{O_2O_1} \cdot \mathbf{O_1S'}}{|\,\mathbf{O_2O_1}\,| \cdot |\,\mathbf{O_1S'}\,|} \tag{2.21}$$

The angular error, $\Delta\theta_1$, between the back-projected source direction and the

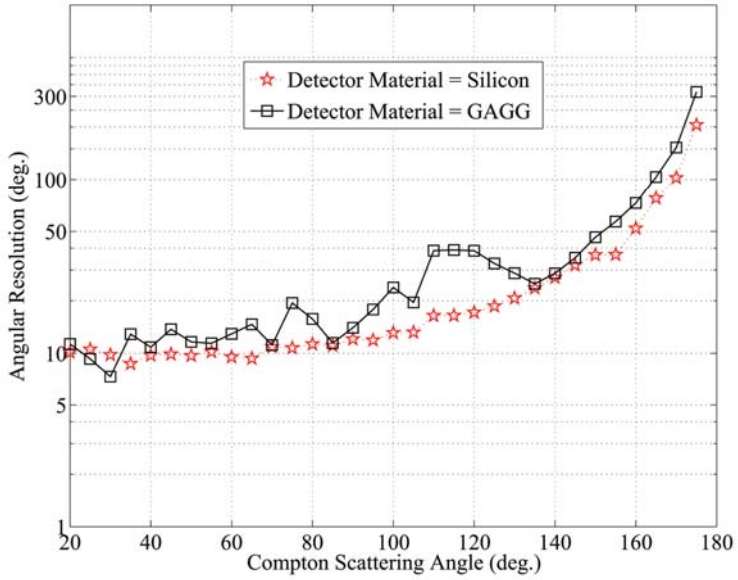

(a) Incident gamma-ray energy = 60 keV

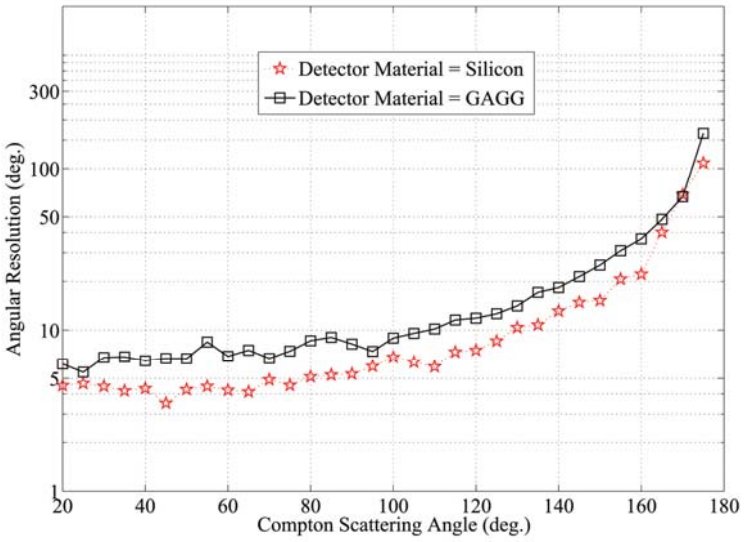

(b) Incident gamma-ray energy = 122 keV

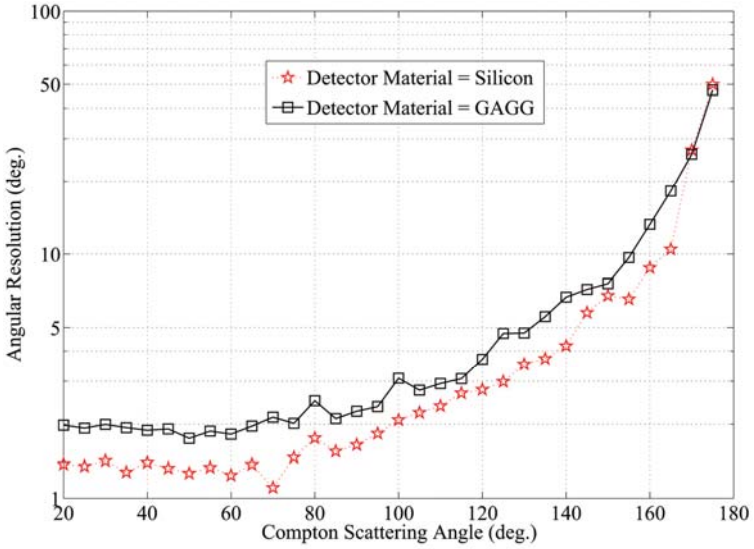

(c) Incident gamma-ray energy = 356 keV

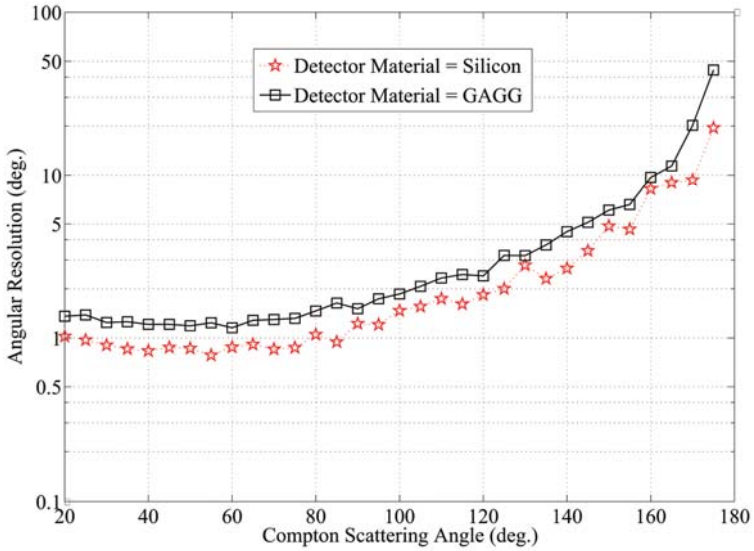

(d) Incident gamma-ray energy = 511 keV

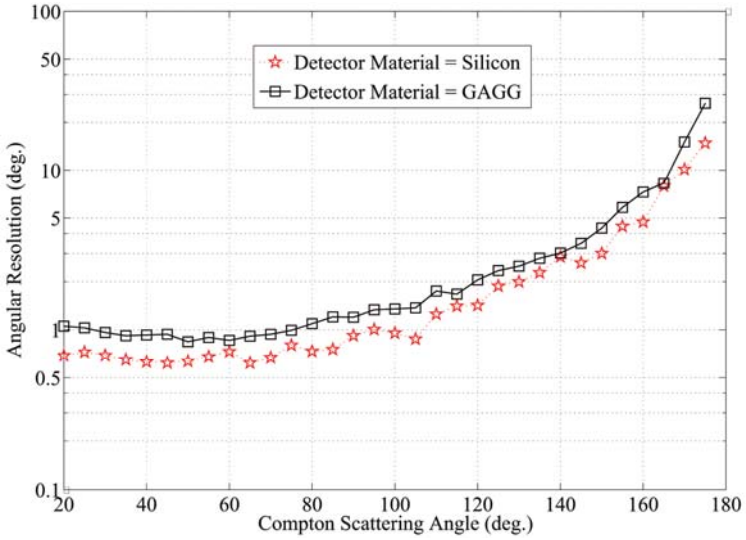

(e) Incident gamma-ray energy = 662 keV

Figure 2.14: Comparison of Angular resolutions FWHM contributed by Doppler broadening effect at different scattering angles with different incident gamma-ray energies for Silicon and GAGG atoms.

true source direction, is

$$\cos\Delta\theta_1 = \frac{\mathbf{O_1S}\cdot\mathbf{O_1S'}}{|\,\mathbf{O_1S}\,|\cdot|\,\mathbf{O_1S'}\,|} \tag{2.22}$$

From the geometry relation in Figure 2.15(a), a equation can be derived,

$$l\cdot\cos(\theta+\Delta\theta_1)\tan(\theta+\angle ASO_1)+\mathrm{d1} = l\cdot\sin(\theta+\Delta\theta_1) \tag{2.23}$$

Usually, the distance from the source to the first element is much larger than the lateral position resolution d1, thus $\angle \mathrm{AS}O_1$ is quite smaller for useful scattering angles, discussed in last two sections. As a result, $\theta+\angle \mathrm{AS}O_1\approx\theta$, and

$$\begin{cases} \sin(\theta+\Delta\theta_1) = \sin\theta+\cos(\theta)\cdot\Delta\theta_1 \\ \cos(\theta+\Delta\theta_1) = \cos\theta-\sin(\theta)\cdot\Delta\theta_1 \end{cases} \tag{2.24}$$

Substituting Equation 2.24 in Equation 2.23, the following relation can be gotten,

$$l \cdot (\cos\theta - \sin\theta \cdot \Delta\theta_1) \cdot \tan(\theta) + \mathrm{d1} = l \cdot \sin\theta + l \cdot \cos(\theta) \cdot \Delta\theta_1 \tag{2.25}$$

Finally, angular resolution due to the first detector lateral position resolution is given by,

$$\Delta\theta_1 = \frac{\mathrm{d1}}{l} \cdot \frac{1}{\cos\theta + \sin\theta \cdot \tan\theta} = \frac{\mathrm{d1}}{l}\cos\theta \tag{2.26}$$

Similarly, from Figure 2.15(b), angular resolution owing to the first detector depth position resolution can be given,

$$\Delta\theta_2 = \frac{\mathrm{d2}}{l}\sin\theta \tag{2.27}$$

Angular resolution due to the second detector lateral position resolution is,

$$\Delta\theta_3 = \frac{\mathrm{d3}}{l}\cos\theta \tag{2.28}$$

Angular resolution due to the second detector depth position resolution is,

$$\Delta\theta_4 = \frac{\mathrm{d4}}{l}\sin\theta \tag{2.29}$$

For each element, there are two lateral position contributions. By means of error propagation, the overall geometry contribution to the angular resolution is,

$$\begin{aligned}(\Delta\theta_{geometry})^2 &= 2 \cdot (\Delta\theta_1)^2 + (\Delta\theta_2)^2 + 2 \cdot (\Delta\theta_3)^2 + (\Delta\theta_4)^2 \\ &= \frac{1}{l^2}\left(2(\mathrm{d1})^2\cos^2\theta + (\mathrm{d2})^2\sin^2\theta + 2(\mathrm{d3})^2\cos^2\theta + (\mathrm{d4})^2\sin^2\theta\right)\end{aligned} \tag{2.30}$$

In Figure 2.16, a set of figures are presented with different values of l, d2 and d4 to show the dependence of the angular resolution on geometry. Values of d1 and d3 are both fixed to be 5 mm. From the plots, we can conclude that the geometry contribution to the angular resolution is small than 1° during the useful scattering angles when the distance between central positions of the two detector elements is longer than 70 mm.

2.4.3.4 Overall Angular resolution

The above analysis of the energy resolution contribution, Doppler broadening effect contribution and geometry contribution to the angular resolution is only based on that the events collected by the system are useful for the back-projection reconstruction. Those events are that the incident gamma-rays undergo only one Compton scattering in the first detector, meanwhile the scattered photons escape the first detector, interact with the second detector and deposit a part or all of their energies. In reality, the incident gamma-rays are possible to have Multi-Compton scattering in a single crystal or between neighborhood crystals. The incident photons also probably penetrate the first layer, interact with the second layer in a Compton scattering process, then the scattered photons escape the second layers and interacted with first layer in a Compton scattering or photo electronic absorption process. Those possibilities can not be separated by the photo sensors and will definitely degrade the performance of the Compton camera. Multi-Compton scattering possibility will be discussed using Mote Carlo simulation in Chapter III.

In addition, the coincidence events are usually measured with a time window. Therefore, the time window should be reasonably small to discriminate random coincidence events, and at the same time, not so small to eliminate the good events as that could lead to poor photon counting. There is a tradeoff between the counting rate and random coincidence events proportion. The random coincidence events de-

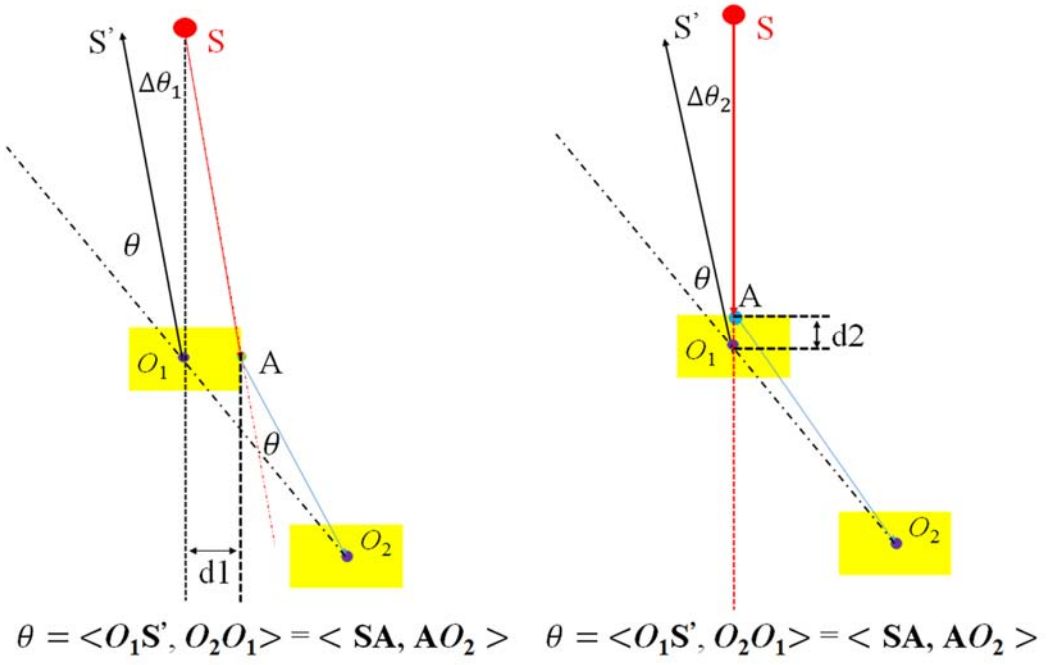

(a) Angular resolution owing to the first detector lateral position resolution

(b) Angular resolution owing to the first detector depth position resolution

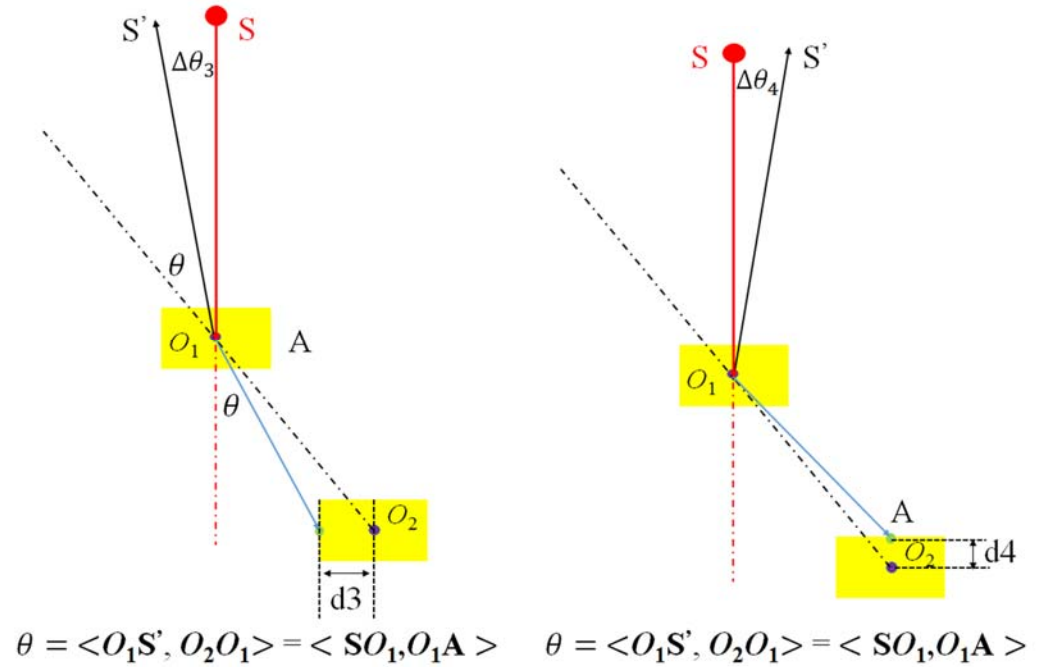

(c) Angular resolution owing to the second detector lateral position resolution

(d) Angular resolution owing to the second detector depth position resolution

Figure 2.15: Angular resolution owing to the detector position resolution. The red and blue arrows in the figures illustrate the true initial and scattered photon directions, respectively, while the black arrows are the back-projection direction.

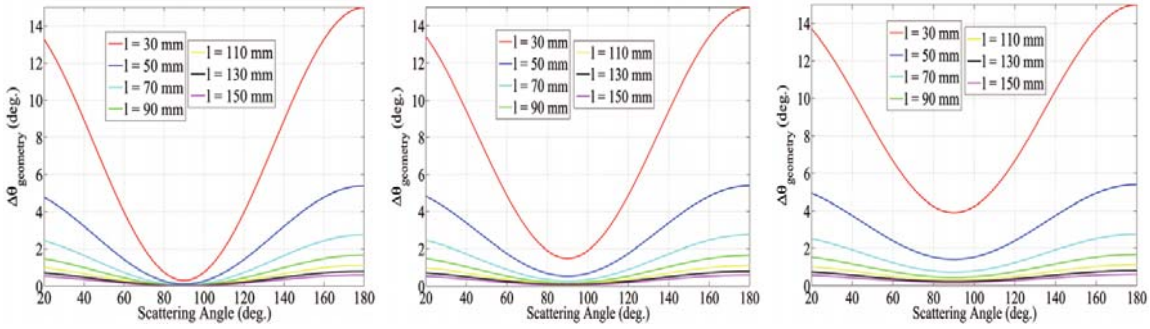

(a) Depth position resolutions for detector 1 and 2 are 1 mm and 1 mm, respectively.

(b) Depth position resolutions for detector 1 and 2 are 1 mm and 3 mm, respectively.

(c) Depth position resolutions for detector 1 and 2 are 1 mm and 5 mm, respectively.

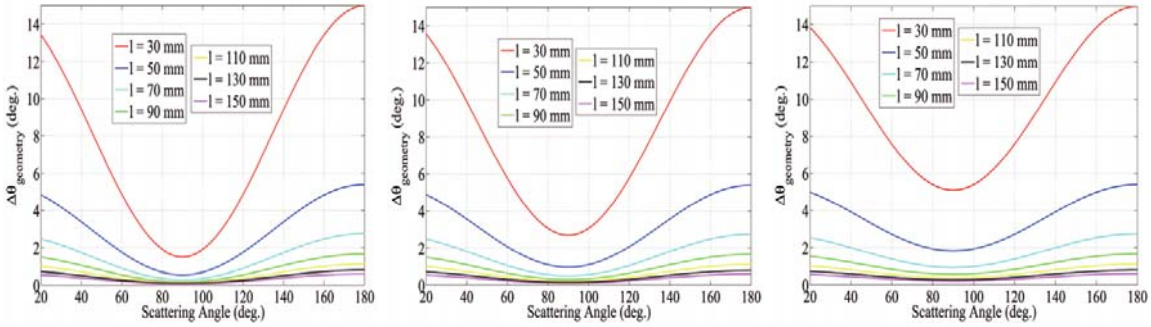

(d) Depth position resolutions for detector 1 and 2 are 3 mm and 1 mm, respectively.

(e) Depth position resolutions for detector 1 and 2 are 3 mm and 3 mm, respectively.

(f) Depth position resolutions for detector 1 and 2 are 3 mm and 5 mm, respectively.

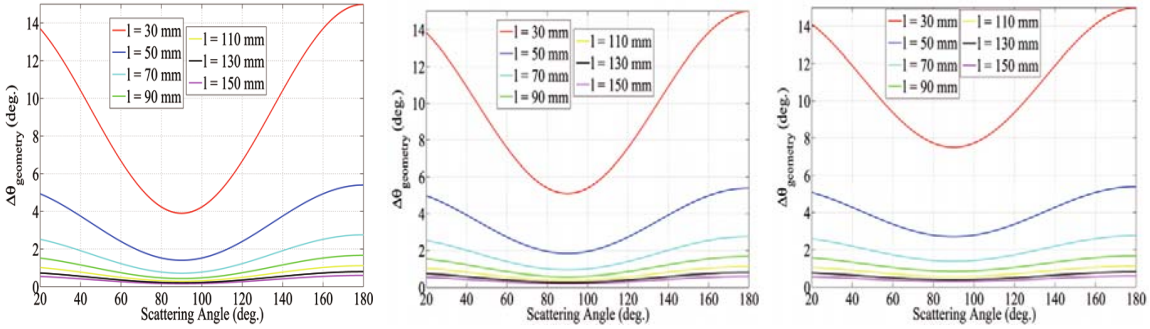

(g) Depth position resolutions for detector 1 and 2 are 5 mm and 1 mm, respectively.

(h) Depth position resolutions for detector 1 and 2 are 5 mm and 3 mm, respectively.

(i) Depth position resolutions for detector 1 and 2 are 5 mm and 5 mm, respectively.

Figure 2.16: Geometry contribution to the angular resolution. A set of figures are drown with different values for depth position resolutions for detector 1 and 2, as well as the distance between the central positions of the two detector elements.

teriorate the angular resolution. In the section VI, we will discuss the coincidence measurement in detail.

For one Compton scattering coincidence event, the origin of gamma-ray emitters can not be identified and only can be estimated on the surface of a well-defined Compton cone. Therefore, the thickness of the reconstructed Compton cones, the accuracy measurement of the distance from the source plane to the scatterer plane for 2D imaging, the statistic, and even the reconstruction algorithms could also effect the final angular resolution of the images.

2.4.4 Efficiency of Compton camera

The Compton camera sensitivity is defined as the fraction of photons emitted from a source must

(1) arrive in the sensitive area of the first detector plane

(2) undergo only one Compton scattering in the scatterer

(3) escape from the scatterer after the Compton scattering

(4) the scattered photon must travel within the solid angle range of the second detector plane

(5) and interact with the absorber to deposit a part or all of its energy

For a real system, the combination of the scatter and absorber must be capable of providing the information of the two consecutive energy depositions, interaction positions and timing. With this information, a time coincidence mode and energy criterion are employed to ensure the two interactions observed are caused by a single gamma-ray.

The above items given for a useful event related to five efficiencies which can be maximized for optimal Compton camera efficiency. By increasing the surface area

of the scatter, or decreasing the source to detector distance, the first term can be improved. In this thesis, we will not discuss the effect on the efficiency due to the distance from the source to the detector. The second one relates to the Compton efficiency of the scatterer. Many possible interactions can happen when gamma-rays are incident to a detector, i.e. Multiple Compton scattering in the same pixel or in neighborhood pixels, Multiple Compton scattering followed by a photo absorption, and only one Compton scattering. Multiple Compton scattering events is allowed in the sensitivity analysis since in real situations there is no way of filtering them out. The third term is related to the effect of self-attenuation of the scattered photon within the scatterer, and this depends on the scattered photon energy and scatterer thickness, material characteristics as well. Decreasing the gap between the two detector arrays or increasing the sensitive area of the absorber can improve the forth efficiency, which is a function of the overall geometry. The fifth term is related to the intrinsic peak efficiency of the absorber. This component is strongly dependent on the energy of the scattered photon. It can be optimized by choosing high density materials and increasing the absorber thickness.

Based on the discussion, the efficiency ε can be expressed as,

$$\varepsilon = \frac{1}{\Omega_1} \int_{\text{det1}} dV_1 \int_{\text{det2}} dV_2 \Delta\Omega_1 \mu_c(E_0) \cdot \exp(-\mu_t(E_0)L_1) \cdot \frac{d\sigma}{d\Omega}(\theta_{12}) \Delta\Omega_2 \cdot \exp(-\mu_t(E_s)L_{12}) \cdot \mu_p(E_s) \tag{2.31}$$

here, Ω_1 is the solid angle subtended by the scatterer, $\Delta\Omega_1$ is the solid angle for dV_1 which is a differential volume element, L_1 is the attenuation distance in the scatterer from the source to dV_1, L_{12} is the attenuation distance from dV_1 to dV_2, and μ_t, μ_c, and μ_p represent the total, Compton scattering, and photoelectric coefficients, respectively.

Analytical calculation of ε can not be done unless numerical integration over the two detector volumes is performed and interaction probabilities for the initial and scattered gamma-rays are known. In this thesis, instead of using an analytical approach, a Monte Carlo simulation based on Geant4 was applied to compute ε. This simulation and its results are described in Chapter III.

2.4.5 Reconstruction Algorithms

In general, Compton cameras record information of the two consecutive energy depositions, interaction positions and timing, but this information is not natively an image. Therefor, the recorded information has to be processed to reconstruct a useful image. In this section, three Compton camera reconstruction algorithms will be described.

2.4.5.1 Simple back projection

The simplest way to produce a Compton image is to back project the cones to the imaging plane as shown in Figure 2.17. Here, we refer this method as simple back projection(SBP) algorithm. In Figure 2.17, **s** is the reconstruction image vector decided by Compton scattering position and each pixel position in the image plane. **t** is the interaction vector which is the axis of the Compton cone. SBP can be expressed as,

$$f(s) = \sum_{i=1}^{N} \delta\left(\langle s, t_i \rangle, \cos\theta\right) \tag{2.32}$$

here, N is the number of events used for reconstruction, and θ is Compton scattering angle computed using the energy deposition. The Reconstruction procedure can be simply concluded as,

$$for \text{ Every Compton Event } (N)$$

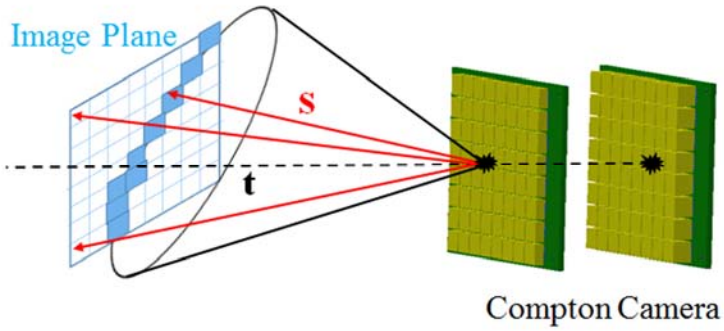

Figure 2.17: Simple back projection method.

for Every Imaging Pixel (s)

Inner Angle(**s**,**t**)

δ(Inner Angle, Compton Angle)

Because each useful event provides the information of the possible source locations which are uniformly distributed on the surface of a cone, a single event alone can not reveal the direction of a single point source. The ambiguity results from not knowing the initial direction of the excited Compton electron. Compton cone collapses to a line that connects the interaction position and the source location, as long as this direction is known. Unfortunately, it is difficult to track the initial direction of the excited electron due to the sporadic path that electrons take.

Form most Compton cameras, including the system discussed in this work, electron tracking information is unknown. In this case, multiple Compton cones must be overlapped to distinguish the source from the background. As seen in Figure 2.18, all of the reconstructed Compton cones are projected in the image plane and intersects in the source direction, however, some also overlapped in other chance locations. As a result, due to those chance intersections combined with measurement errors and interference from other sources and background, a large amount of events are required to yield the true source direction in practice.

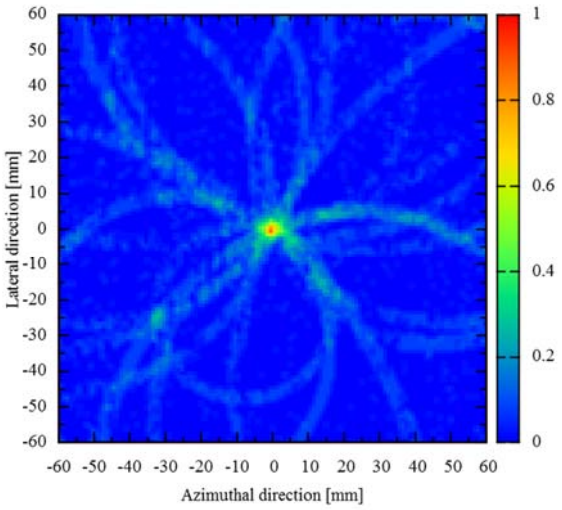

Figure 2.18: Point source image reconstructed using Simple back projection method with 20 events. The data of those 20 events were obtained using Geant4 simulation that reported exact energy deposition and interaction position information of 662 keV photons emitted from a point source which was placed at the center of plane. Doppler broadening effect because of the initial momentum of the Compton electron was ignored.

Since this method is simple and fast, it might be useful in some special applications which requires fast response rather than promise angular resolution, such as source probing. In order to get higher quality Compton images, more advanced reconstruction techniques are demanded.

2.4.5.2 Filtered back projection

In 2000, for the first time, Parra presented an analytical inversion algorithm based on spherical harmonics expansion for the complete date set of all possible scattering angles according to Klein-Nishina formula [70]. In reality, as pointed out by Tomitani and Hirasawa [71], because the detector is limited to finite size and detecting events with small Compton scattering angles is difficult, it is almost impossible to measure a data set with a full range of scattering angles. As an improvement, Tomitani and Hirasawa proposed an reconstruction algorithm for limited angle Compton data set. With perfect detector performance, a point source will produce a filted back projection

image as,

$$f(s) = \sum_{i=1}^{N} \sum_{n=0}^{NMAX} \frac{2n+1}{4\pi} \frac{1}{H_n} P_n(\cos\theta) P_n(\langle s, t_i \rangle) \tag{2.33}$$

here, H_n is expressed as,

$$H_n = \int_{\theta_1}^{\theta_2} d\cos\theta \sigma(\theta) P_n^2(\cos\theta) \tag{2.34}$$

where, $\sigma(\theta)$ is computed using Klein-Nishina formula, P_n is Legendre polynomial. Because the image is obtained by transforming a given source distribution into spherical harmonics space, filtering and then transforming back into the angular space, this method is named as filtered back projection(FBP). Figure 2.19 shows two images obtained using the same data set with SBP and FBP respectively. The data of those events used for reconstruction were obtained using Geant4 simulation that provided exact energy deposition information of 662 keV photons emitted from a point source which was placed at the center of image plane. Doppler broadening effects because of the initial momentum of the Compton electron were ignored. The interaction postion was assumed to be the center of the crystals. From the Comparison we can see that, FBP could offer a better angular resolution, although it costs a slightly longer computation time. Since FBP algorithm can also be executed event by event, it is easy to implement this method in real time imaging.

2.4.5.3 List-mode maximum likelihood expectation maximization

The maximum likelihood expectation maximization (MLEM) is an widely used and accepted iterative algorithm in the field of gamma-ray imaging [74–77]. Different from SBP and FBP, which is a linear superposition of the Comtpon cones, MLEM uses the combined knowledge of the entire group of the events to calculate and converge to

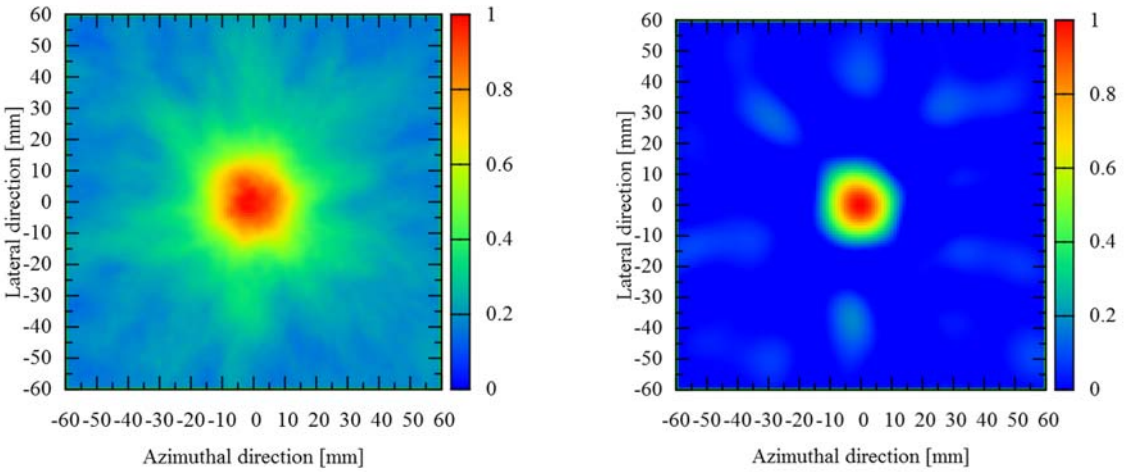

(a) Point source image reconstructed by BP

(b) Point source image reconstructed by FBP

Figure 2.19: Point source images reconstructed by BP and FBP, respectively. In this simulation, a Compton camera made of a 8×8 array of GAGG with 5 mm in thickness as the scatterer and another 8×8 array of GAGG with 10 mm in thickness as the absorber was built. the gap distance was 80 mm. The distance from the source to the scatterer was 100 mm. 2000 coincidence events were used to reconstruct the images.

a source distribution with the maximum likelihood given the measured data set and a model of the detector system. The convergence is assured as long as the total number of events is larger than the pixel number in the image plane. MLEM is performed using the following equation [77, 134],

$$\lambda_j^{n+1} = \frac{\lambda_j^n}{s_j} \sum_i \frac{Y_i t_{ij}}{\sum_k t_{ik} \lambda_k^n} \tag{2.35}$$

where, ${\lambda_j}^n$ is the estimated value of pixel j at n^{th} iteration, s_j denotes the probability that an emission from pixel j to be detected anywhere, Y_i is the number of times that measurement i is detected, $i = \{1,2,3,....i,....I\text{-}1,I\}$ includes all possible measurement bins, and t_{ij} represents the probability that a photon emitted from pixel j is collected

as measurement i. equation [77, 134],

$$s_j = \sum_i t_{ij} \tag{2.36}$$

And the matrix t_{ij} can be computed analytically as,

$$t_{ij} = \exp(-\sigma_t(E_0)r_{01})\frac{d\sigma_c}{d\Omega}\exp(-\sigma_t(E_0 - E_s)r_{12}) \tag{2.37}$$

here, $\sigma_t(E)$ denotes the total absorption cross section for a gamma-ray at energy E, E_0 and E_s are the initial energy of the photon and energy loss due to the Compton scattering, respectively, r_{01} is the attenuation distance in the scatterer from the source to the Compton scattering position, r_{12} is the attenuation distance between the two consecutive interaction locations, and $d\sigma_c/d\Omega$ represents the differential Compton cross section, which can be estimated by the Klein-Nishina cross section divided by r_{12}^2. Therefore, the system matrix is the possibility for the initial emission to reach the first interaction position, be scattered at angle θ, the scattered photon escapes the first detector and reach the second interaction position.

Barrett et al. [74] and Parra and Barrett [75] have demonstrated that the above discussion hold in list-mode case, in which, each observed measurement i can be considered to be a unique bin. Thus, $Y_i = 1$ for all the every measured event i and 0 for all unmeasured events. The one exception is that because the Y_i no long span the space of all possible observed events, $s_j \neq \sum_i t_{ij}$, but rather is the integral of all possible events i, including those events not observed in Y.

In [76], Scott J. Wilderman proposed an approaches as described below to compute s_j,

$$s_j \propto \sum^{det1} \frac{1 - \exp(-\sigma_t(E_0)z_{j1})}{d_{j1}^3} \tag{2.38}$$

here, z_{j1} is the pathlength inside the first detector along the direction of the initial photon from the center of pixel j to the center of each detector element and d_{j1} is the distance between the centers.

Generally, list-mode MLEM reconstruction algorithm can achieve the best angular resolution among the three discussed methods. However, because the iteration calculation, the computation cost for this method is much higher. As a result, it is difficult to apply this method for applications when real time imaging is demanded.

2.5 Front-end Electronics

As for this wide area gamma-ray imager, each channel of such an energy resolving multi-channel system must be of low power consumption and therefore it must be consisted of simple circuits. Traditional pulse-height-analysis systems suffer from the complexity arising from analog to digital converters (ADC) circuits. In practice, it is difficult to be applied to a large format array of pixellated detectors. Kenji et. al proposed a new time over threshold circuit which is capable of converting analog signal to digital signals in [135]. This new dynamic time-over-threshold (DToT) method compares input pulse signals with a dynamic threshold and measures the time width while the amplitude of input pulse signals is higher than the threshold level. As a result, the DToT method converts the pulse height into the corresponding time width. By measuring the time with, the pulse height, which contains the energy information, can be estimated due to a good linearity relationship between the time width and input pulse height. Figure 2.20 is a typically DToT circuit for one channel. It is simply consisted of a charge sensitive preamplifier, a CR-RC shaper, a comparator and two mono-stable vibrators. Figure 2.21 shows the theory of DToT method. The bule line in the figure is the DToT signal which is used to estimate the amplitude of the input signal which is express in red line.

A good relationship between the input pulse height and DToT signal time width

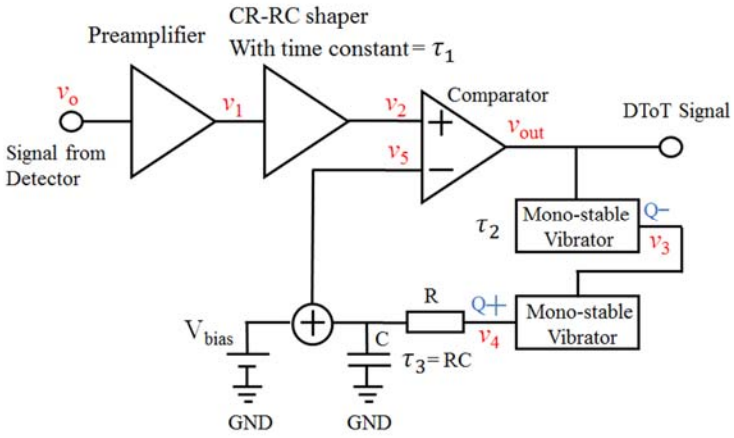

Figure 2.20: DToT circuit for one channel. In the figure, the red characters denote the signals of the points where they locate.

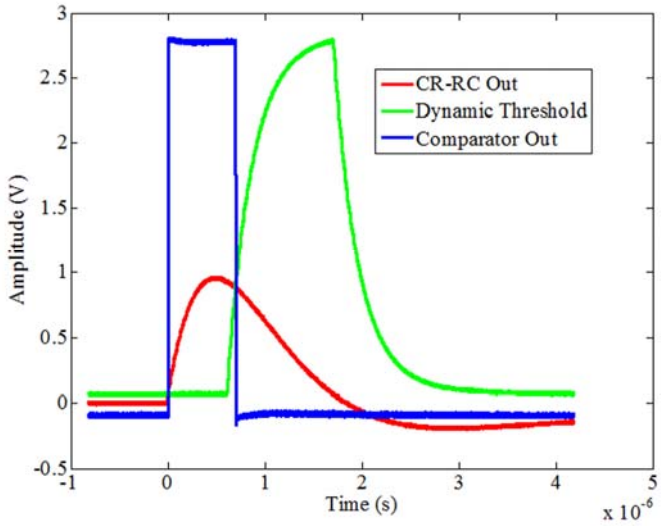

Figure 2.21: DToT theory.

can be obtained as long as the three time constants as shown in Figure 2.20 are the same. This method is also capable of realizing parallel signals processing. In Chapter IV, we will evaluate and present the performance of electronics including Application Specific Integrated Circuit(ASIC) and printed boards using discrete components both with DToT method integrated.

2.6 Data Acquisition Architecture

Figure 2.22 shows the data acquisition architecture. A FPGA(EP4CE55F23C7N) is applied to perform multi-channel spectra and coincidence measurement.

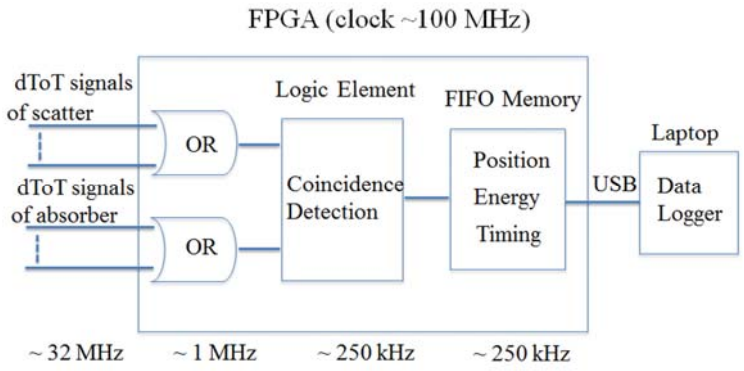

Figure 2.22: Data Acquisition Architecture.

The digital signals of scatterer and absorber are sent to a OR logic, respectively. The two OR signals are then transported to a logic element which executes the coincidence measurement using a time window. The energy, timing, and position information of the coincidence events are poured into a FIFO whose information can be acquired by a data logger using a USB connection. The sampling frequency of the FPGA was 100 MHz.

CHAPTER III

Monte Carlo Simulation based on Geant4

Compton camera is the heart of the proposed wide area imager and is, thus, responsible for collecting the high-energy photons emitted from possible radiation sources, estimating the energy depositions and locations of interactions, and generating the coincidence count data for subsequent image reconstruction. The capability of performing these functions depends on the design, materials, and electronics of the Compton camera. In this chapter, a Geant4 description and analysis of the Compton camera parameters as how they effect the camera's performance in wide area imaging application is provided. Those parameters including the thickness of the scatterer crystals, thickness of absorber crystals, and the distance between them. In addition, the performance of the proposed imager in both modes are also evaluated using simulation before implementation.

3.1 Geant4 Simulation Toolkit

The Geant4 toolkit is a platform for the simulation of the passage of particles through matter based on Monte Carlo methods [136–139]. It is the successor of the Geant series of software toolkits which are developed by CERN. Geant4 is the first to use object-oriented programming implemented in C++. It is a international collaboration that takes care of the development, maintenance, and user support of

the toolkit. Therefore, Geant4 acts as a repository which incorporates a large part of all that is known about particle interactions. It is now widely applied in various areas, including high energy physics, nuclear experiments, medical science, accelerator and space physics researches. Since the Geant4 software and source code is freely available from the official web site [140] and compatible to multiple operation systems, such as Linux, Unix, Mac OS, and Windows, the software is welcome in a large number of research projects around the world. Due to the integration with facilities for handling geometry, stepping, tracking, detector response, run management, visualization and user interface, less time is required on the low level details and researchers can start immediately on the more important parts of the simulation in most cases.

The flexibility of understanding the steps of detailed interactions between a photon and the detector, as well as the simplicity of modifications and improvements to optimize the design of the system leads the Geant4 the best simulation tool for this work. Moreover, the Geant4 Low Energy Electromagnetic package allows it capable of analyzing Doppler broadening effect for a Compton camera [141].

3.2 Geant4 Evaluations of Compton Camera Parameters

As discussed in Chapter II, the detector material and size have already been decided to be high energy resolution GAGG crystals and 10 mm $\times$ 10 mm due to the consideration of absolute efficiency and simplicity of the instrument. However, the thicknesses of both scatterer and absorber crystals, which also influence the efficiency and angular resolution of the camera, are to be determined. In addition, the gap distance between the two arrays also acts as a tradeoff between the efficiency and angular resolution, thus demanded to be decided. In this chapter, simulation analyses are presented to find the optimized values for those parameters.

3.2.1 Thickness of Scatterer

As mentioned above, for Compton imaging, a useful event is that a gamma-ray emitted from a source must be incident to the first detector, undergo only one scattering and escape the detector. As the thickness of the scatter increases, the possibility of interaction between the photon and detector increases. However, the fraction of multiple Compton scattering events, which can not be filtered and deteriorate the performance of the camera, might also increases [94]. Additionally, as the thickness of the scatter increases, the error of the Compton scattering position increases, which as a result, degrades the angular resolution. Here, we perform a Geant4 simulation to study the influences of the thickness of scatterer's crystals on the fraction of useful measurements in the total observed events, on the total efficiency, and on the angular resolution of the camera.

3.2.1.1 Effect on the fraction of useful events

Figure 3.1 shows the setup for this simulation. An 8×8 array of GAGG crystals, each with 10 mm $\times$ 10 mm in sensitive area, was built. Gamma rays of 662 keV in energy were incident to the detector array isotropically. Energy threshold was 40 keV (6% FWHM at 662 keV) which means only those events with total energy losses in the detector higher than 40 keV were recorded. For a single photon, the times of Compton scattering as well as the times of photoelectric absorption were tracked.

Figure 3.2 and Figure 3.3 shows the simulation results. As shown in Figure 3.2, while the thickness of the crystals increases, the photon is more likely to interact with the crystals. The possibilities of one Compton scattering, multiple Compton scattering, as well as photoelectric all increase as the thickness of the crystals increases. Taking advantage of time coincidence measurement, photoelectric events in the first detector can be filtered. However, there is no way to eliminate multiple scattering events from only one scattering events, merely which are useful for reconstruction.

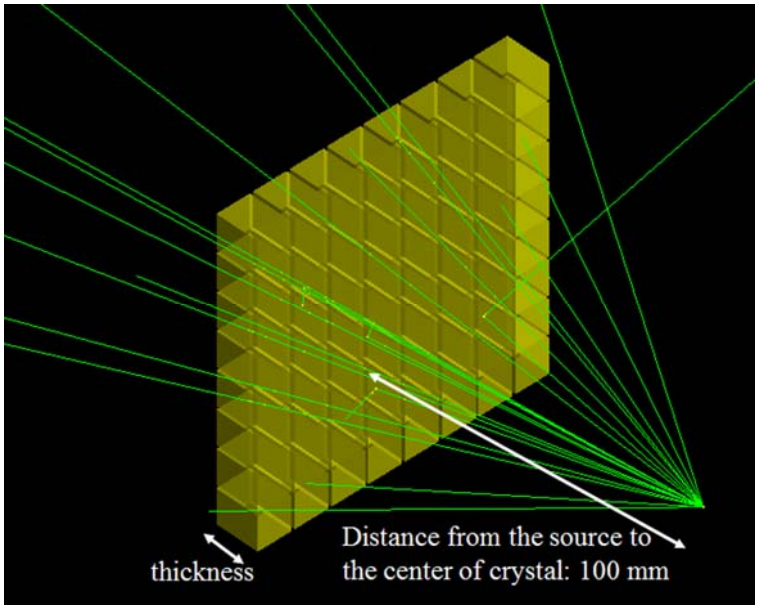

Figure 3.1: Geant4 setup for simulating scatterer thickness's effect on the fraction of useful events.

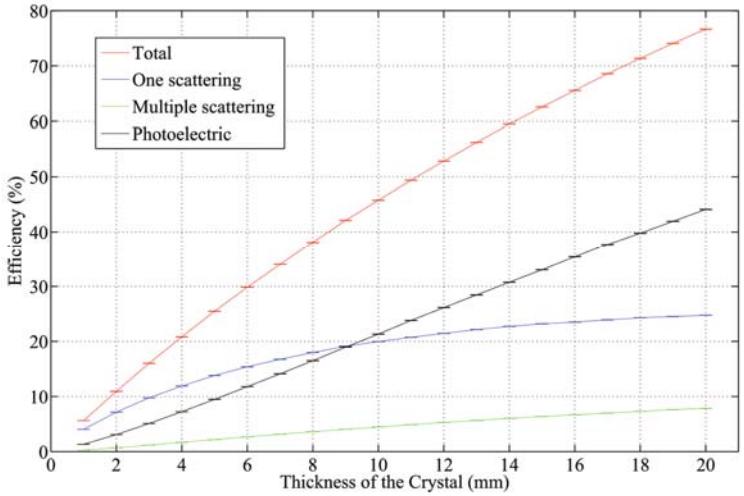

Figure 3.2: Possibilities for photoelectric, one Compton scattering, multiple scattering and total interactions of a gamma ray at 662 keV with GAGG scintillator.

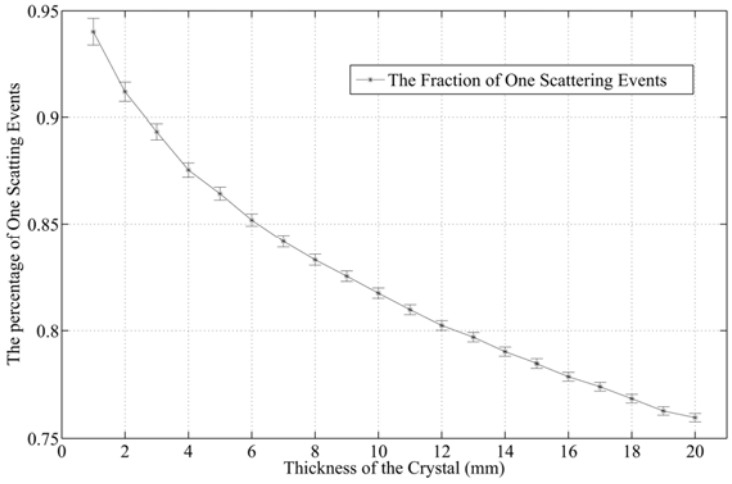

Figure 3.3: Fraction of One scattering events in the total Compton scattering measurements for gamma-rays at 662 keV with GAGG.

Figure 3.3 shows that, along with the increase of the crystal thickness, the fraction of only one scattering events is decreasing. When the thickness is thinner than 5 mm, the fraction is higher than ∼90%.

3.2.1.2 Effect on the total efficiency

As a further step, a Compton camera as shown in Figure 3.4 was built to compute the effect of scatterer thickness on intrinsic efficiency. The Distance between the two detector was set to be 80 mm, the absorber crystal thickness 10 mm, the distance between the source to the scatter 100 mm and gamma-ray energy 662 keV. Multiple scattering events are counted since they cannot be filtered.

As shown in Figure 3.5, the one Compton scattering, or useful events as well as multiple scattering events increase as the thickness of scatterer crystal increases. However, the fraction of only one scattering events is decreasing, as shown in Figure 3.6. When the thickness is thinner than 5 mm, the fraction is about to be higher than 90%，and this is consistent with the result shown in Figure 3.3.

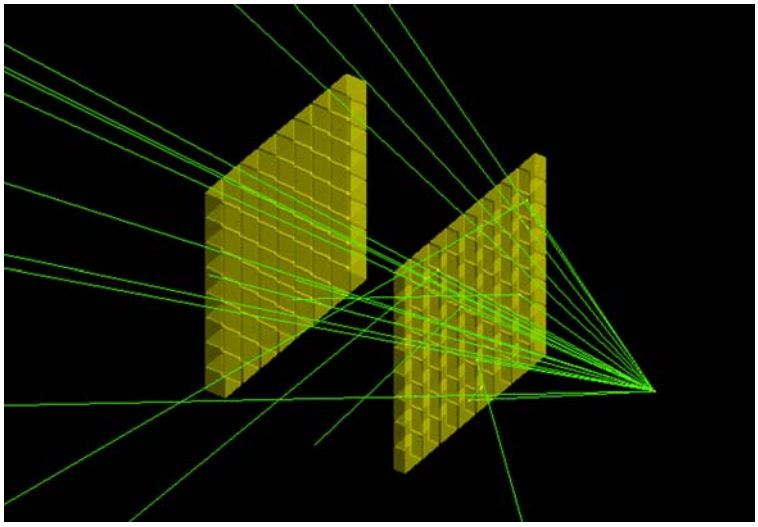

Figure 3.4: Geant4 setup for simulating scatterer thickness's effect on the efficiency of Compton camera.

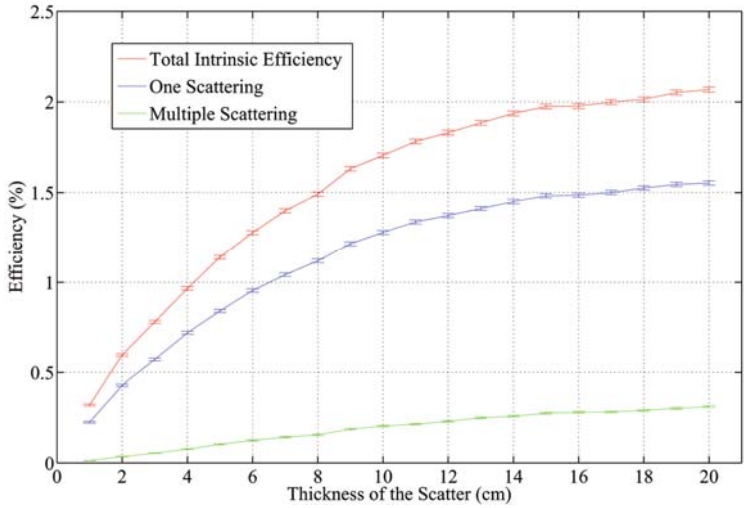

Figure 3.5: Possibilities for one Compton scattering, multiple scattering and Comtpon scattering of a gamma ray at 662 keV with GAGG scintillator.

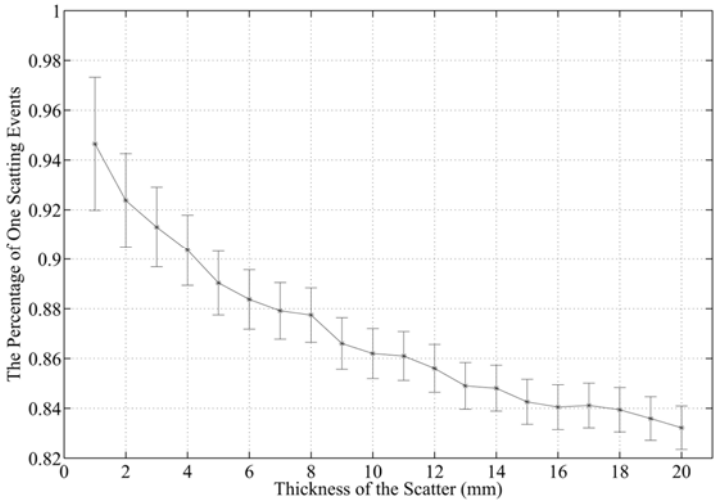

Figure 3.6: Fraction of One scattering events in the total Compton scattering measurements for gamma-rays at 662 keV with GAGG.

3.2.1.3 Effect on the angular resolution

Using the same setup, we collected coincidence events with exact energy deposition information in both detector arrays for reconstruction when gamma rays of 662 keV in energy were incident to the front detector plane. The interaction positions were defined to be the center of the crystals as done in real situation. The thickness of the scatterer crystals are changing from 2 mm to 10 mm while the thickness of the absorber crystals were fixed to be 10 mm. Below are the reconstructed images using FBP when the thickness of the scatterer crystals are 2 mm and 10 mm, respectively. The Doppler broadening effect was ignored during the reconstruction.

As shown in Figure 3.8, as the thickness of scatterer crystals increases, the angular resolution in both directions are getting worse.

3.2.2 Thickness of Absorber

When the scattered gamma ray escapes the first detector array after only one Compton scattering, it must fall into the solid angle subtended by the absorber and undergo interactions with the detector in order to be considered as a useful event.

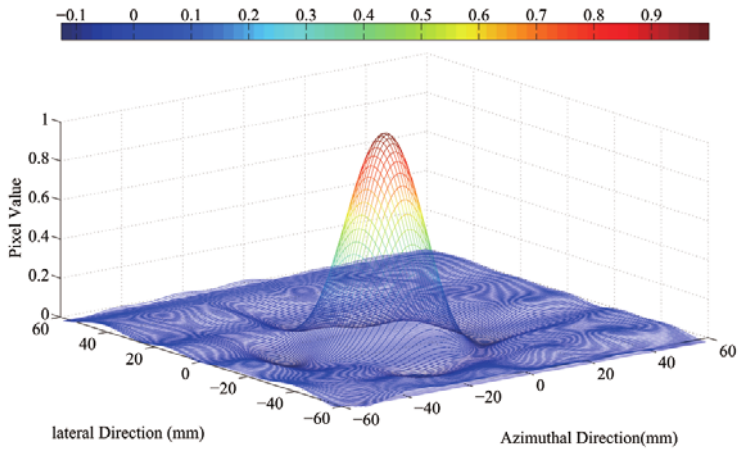

(a) Thickness = 2 mm

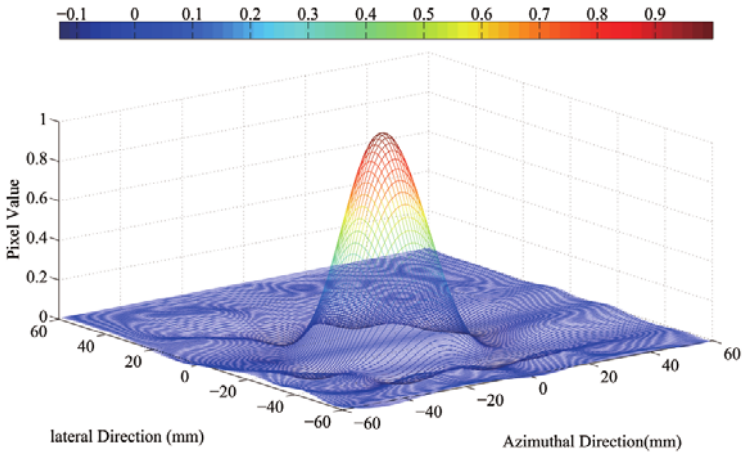

(b) Thickness = 10 mm

Figure 3.7: Point source images through FBP while the scatterer crystals' thicknesses were 2 mm and 10 mm, respectively. The point source was placed at the center of the image plane which was 100 mm away from the scatterer.

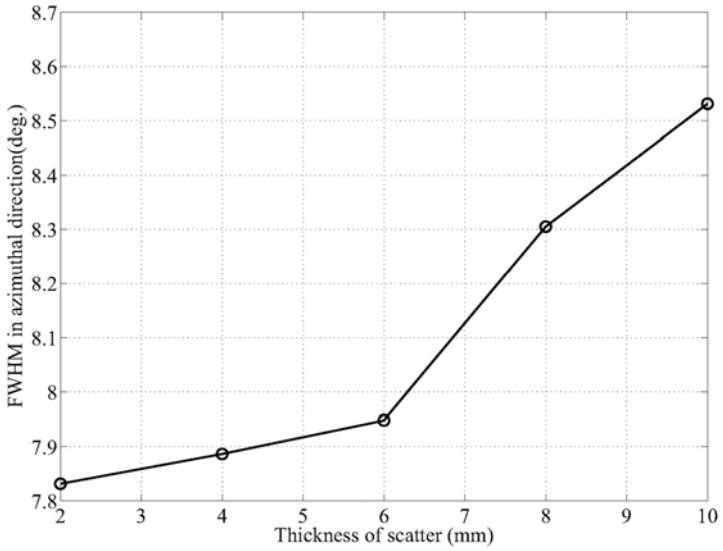

(a) FWHM in Azimuthal direction

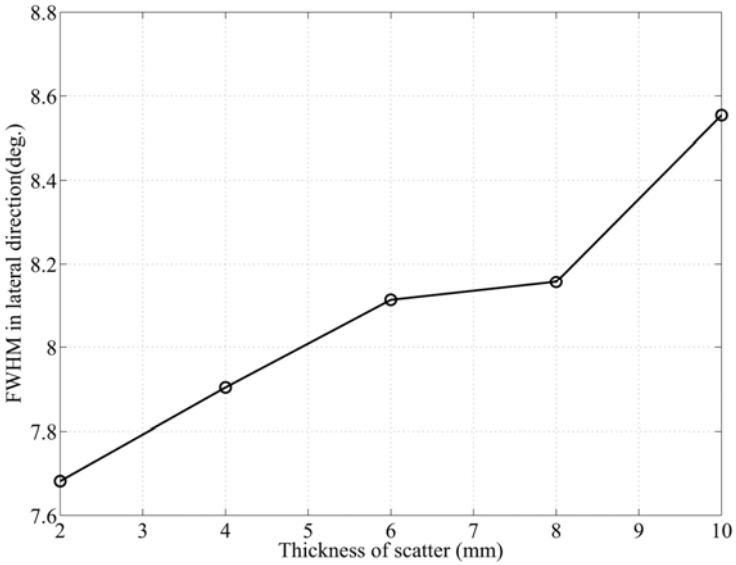

(b) FWHM in Lateral direction

Figure 3.8: Angular resolution Vs. thickness of scatterer using Geant4 simulation.

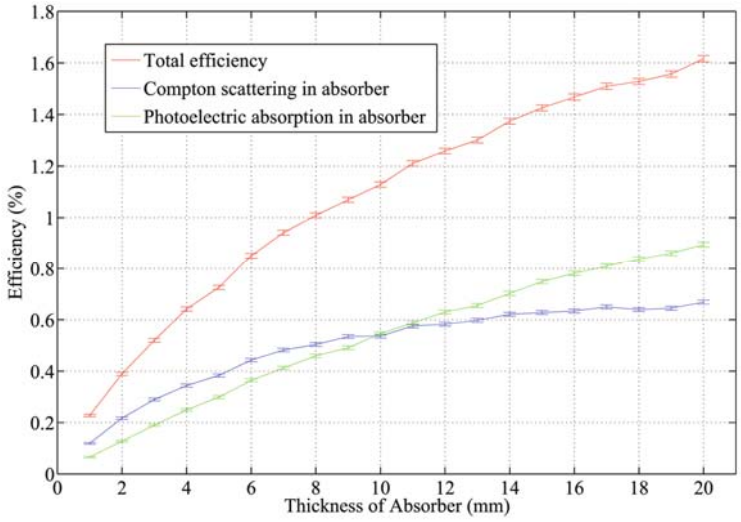

Figure 3.9: Possibilities for Compton scattering, photoelectric absorption and Total efficiency of a scattered gamma ray with GAGG scintillator.

The thickness of the absorber highly influences the possibility of interaction between the scattered photon and the detector. Similarly, as the thickness of the absorber increases, the error of the interaction position in absorber increases, which as a result, degrades the angular resolution. Geant4 simulation that computes the effect of the absorber's crystal thickness on the total efficiency and angular resolution was run.

3.2.2.1 Effect on the total efficiency

As shown in Figure 3.4, in this simulation work, the thickness of the scatterer crystals were set to be 5 mm in order to guarantee the fraction of one scattering events about 90%, the distance from the source to the scatterer 100 mm, the gap between the two arrays 80 mm, the Doppler effect ignored, the interaction position in the center of the crystals, and the energy deposition in both layers exact for reconstruction. Figure 3.9 shows the total efficiency dependence on the thickness of the absorber crystals. As the thickness of the absorber crystals getting thicker, the possibilities for the scattered gamma ray to Compton scatter or photoelectric with the absorber detectors are both becoming higher. The Compton scattering and photoelectric absorption in the

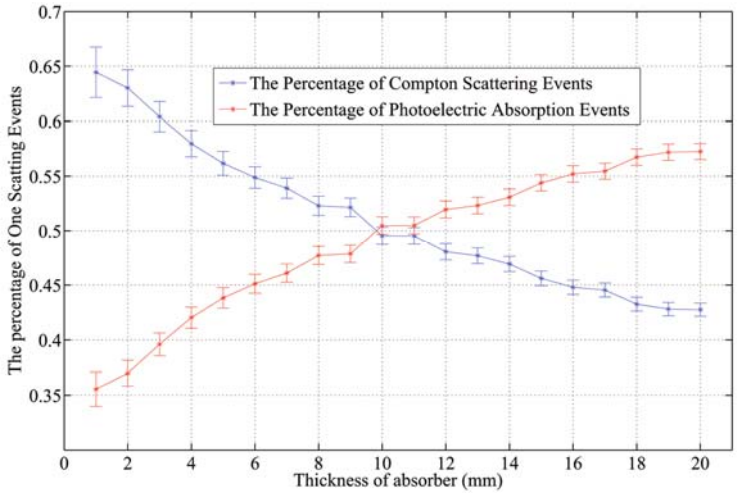

Figure 3.10: Percentage of Compton scattering and photoelectric absorption Vs. the thickness of absorber crystals.

absorber have the same possibility while the thickness of the absorber is 10 mm. This can also be found in Figure 3.10, which presents the fraction of Compton scattering events and absorption events in absorber for the scattered photons, respectively.

Figure 3.11 gives the fraction of one Compton scattering events in scatterer in all the Compton scattering measurements. The fraction has no obvious difference while the thickness of the absorber crystal is changing. This fraction keeps at the level of ~90%, and it is consistent with former results.

3.2.2.2 Effect on the angular resolution

Using the same setup, coincidence events with exact energy deposition information in both detector arrays for 662 keV incident gamma-rays were collected for reconstruction. The interaction positions were defined to be the center of the crystals as done in real situations. The thickness of the absorber crystals are changing from 2 mm to 10 mm while the thickness of scatterer crystals was 5 mm. Below are the reconstructed images through FBP when the thickness are 2 mm and 10 mm respectively.

As shown in Figure 3.13, as the thickness of absorber crystals increases, the

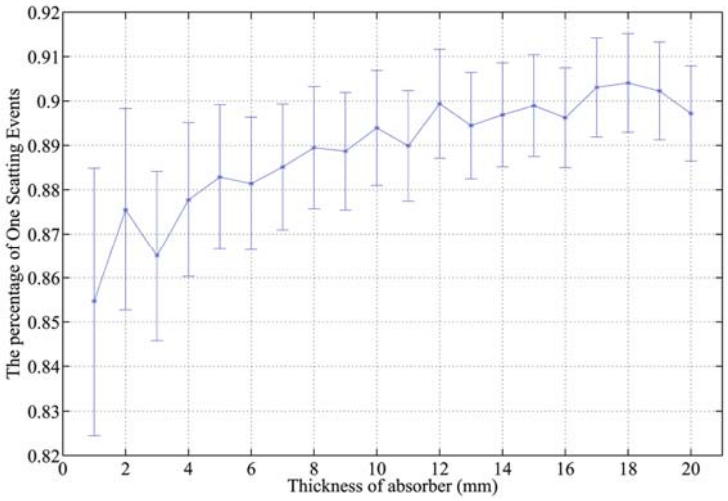

Figure 3.11: Fraction of one scattering events in scatterer Vs. the thickness of absorber crystals.

angular resolution in both directions are also getting worse.

3.2.3 Distance between the Two Arrays

3.2.3.1 Effect on the total efficiency

The effect of gap distance on the performance of efficiency as well as angular resolution were also analyzed using Geant4 simulation. In this simulation, the thickness of the scatterer and absorber crystals were 5 mm and 10 mm, respectively, the distance from the source to the scatter 100 mm. The total efficiency and angular resolution were computed while the gap between the two arrays were changing from 30 mm and 150 mm. As shown in Figure 3.14, as the distance between the two arrays increases, the total efficiency decreases due to the decreases of the possibilities that the Compton scattered photons travel into the solid angle of the second detector. The fraction of the one scattering events keeps at a same level, around 90% because the thickness of the scatterer crystals was the same.

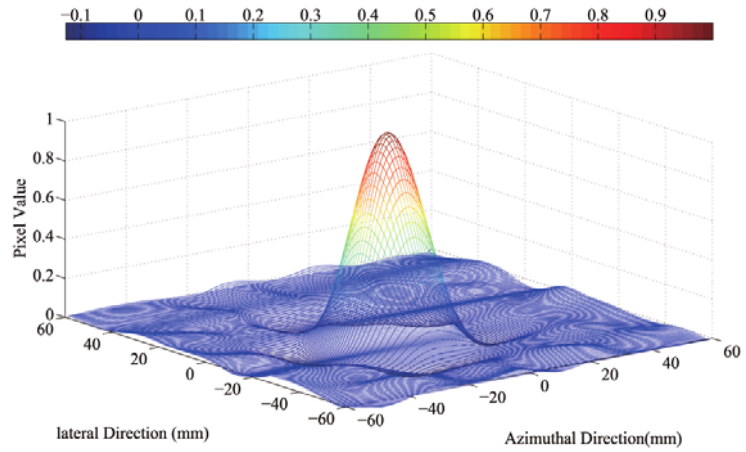

(a) Thickness = 2 mm

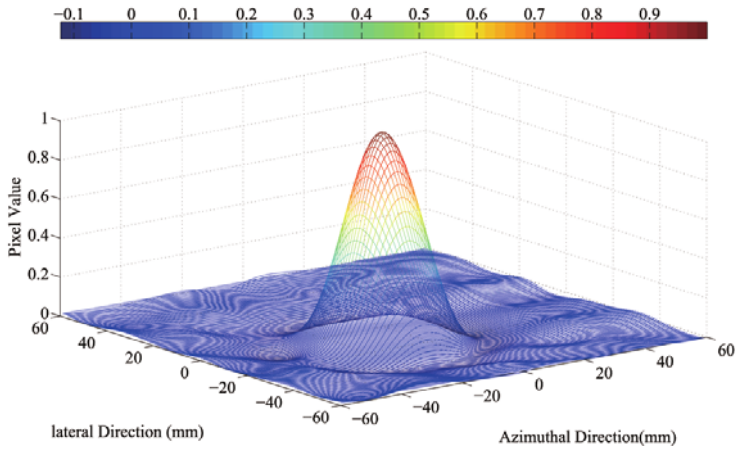

(b) Thickness = 10 mm

Figure 3.12: Point source images while the absorber crystals' thicknesses were 2 mm and 10 mm, respectively. The point source was placed at the center of the image plane which was 100 mm away from the scatterer.

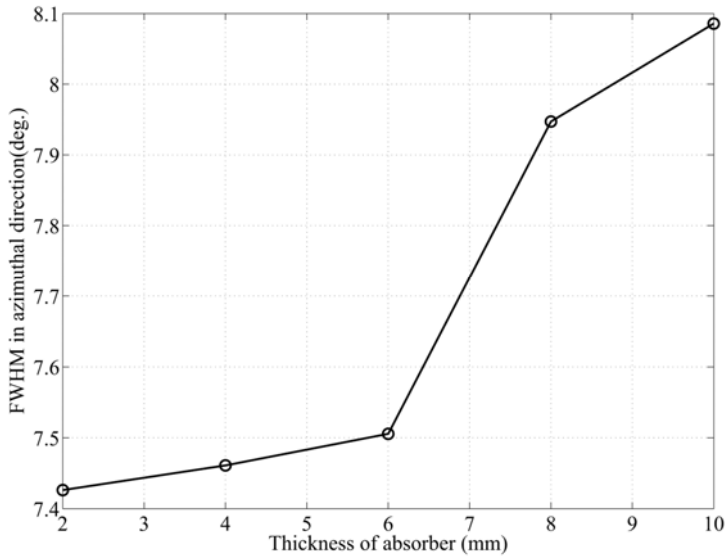

(a) FWHM in Azimuthal direction

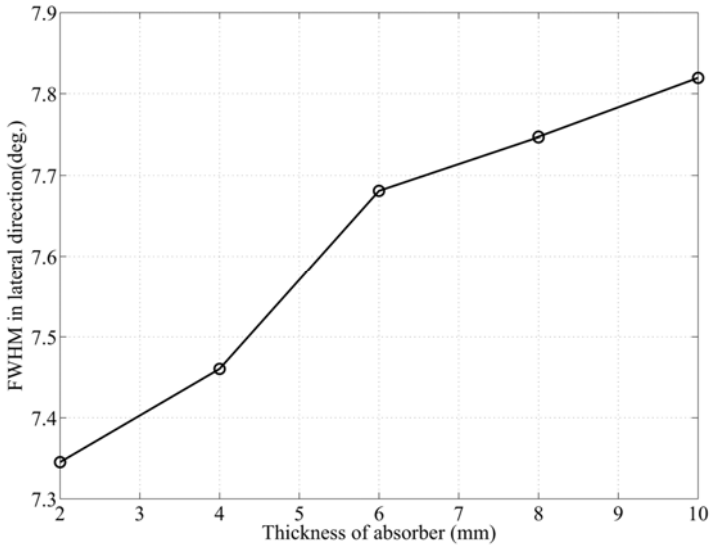

(b) FWHM in Lateral direction

Figure 3.13: Angular resolution Vs. thickness of absorber using Geant4 simulation.

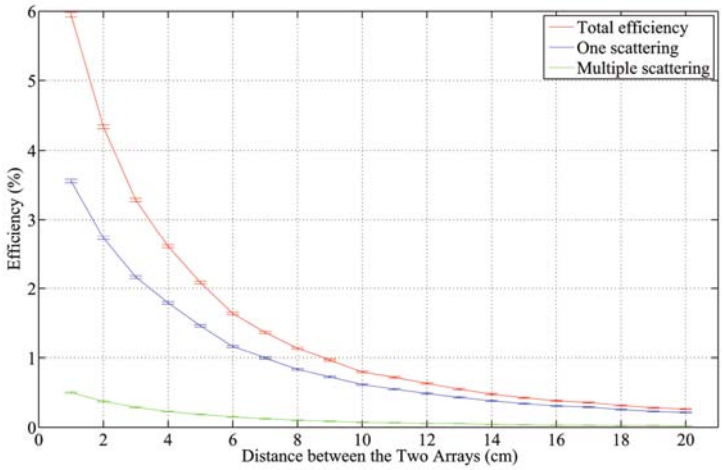

Figure 3.14: Geant4 simulation of dependence of Compton camera efficiency on the gap distance.

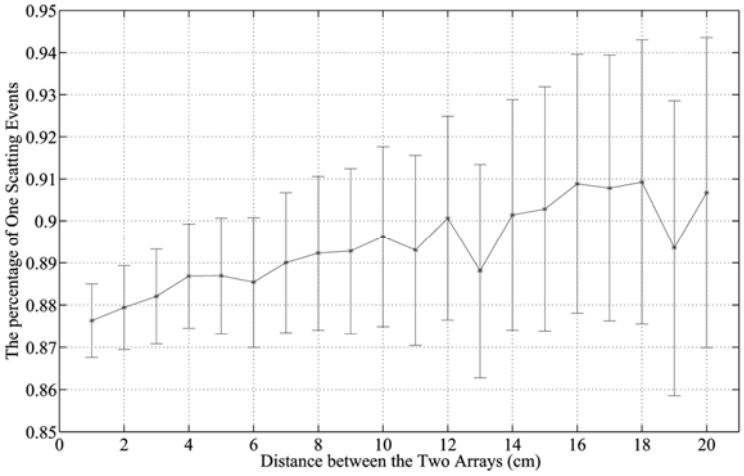

Figure 3.15: Fraction of one scattering events in scatterer detectors.

3.2.3.2 Effect on the angular resolution

Point source images were reconstructed using the coincidence data collected while the gap distance was increased from 30 mm to 150 mm. Figure 3.17 shows the dependence of angular resolution in both azimuthal and lateral directions on the gap distance. As shown in the figures, as the gap distance increases, the angular uncertainties are getting better. This reveals that the gap distance is a tradeoff between the Compton camera efficiency and angular resolution. Point source images while the gap distance was 30 mm and 150 mm are shown in Figure 3.16.

As shown in Figure 3.17, the angular resolutions in both direction are getting better while the gap distance increases.

3.2.4 Overall Consideration

Using Geant4 simulation, the effect of Compton camera parameters, including the thickness of scatterer and absorber crystals as well as the gap distance, on its performance was studied. Another point should be mentioned here is that crystals with smaller size usually have a higher energy resolution which results in a lower contribution to the overall angular resolution. In the above simulation work, we just took account the geometry contribution when the crystal sizes were changed but ignored the energy resolution alternations.

In this work, in order to balance the efficiency and angular resolution of the whole system, we decided to use 5 mm thick crystals as the scatterer detectors, to achieve high fraction of useful events ($\sim$90%), good interaction position resolution and energy resolution. As a compensation to the overall efficiency, crystals with 10 mm in thickness were chosen as the absorber detectors. Another reason for using thick crystals as in the absorber array is that, the energy deposition in the absorber is not as important as that in the scatter, since in real reconstruction, absorber energy will be not applied in the work, but merely used to calibrate the initial energy of the

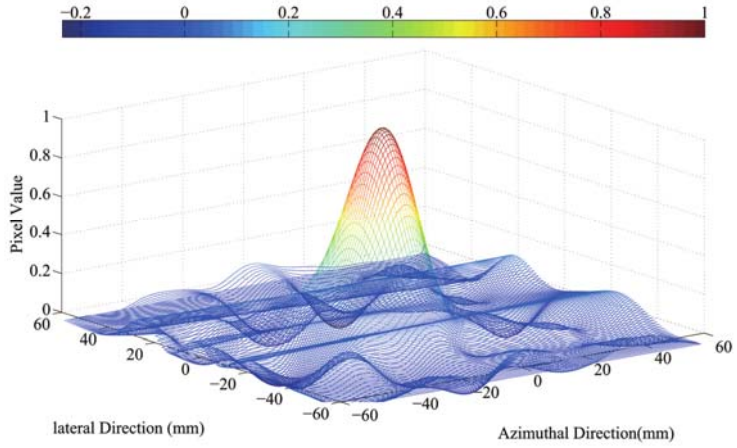

(a) Gap distance = 30 mm

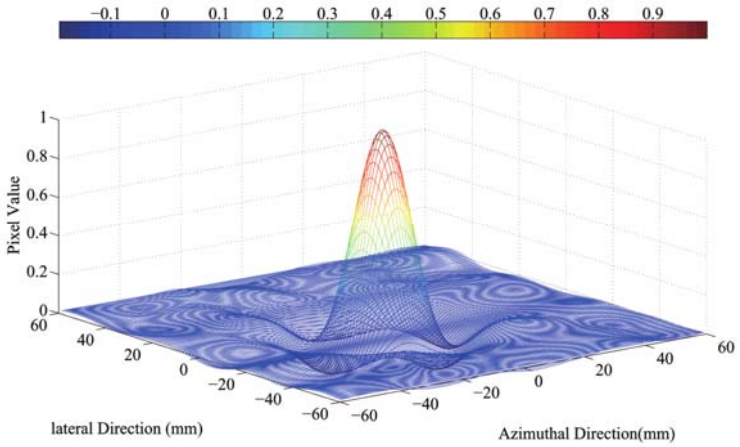

(b) Gap distance = 150 mm

Figure 3.16: Point source images while the gap distance was 30 mm and 150 mm, respectively. The point source was placed at the center of the image plane which was 100 mm away from the scatterer.

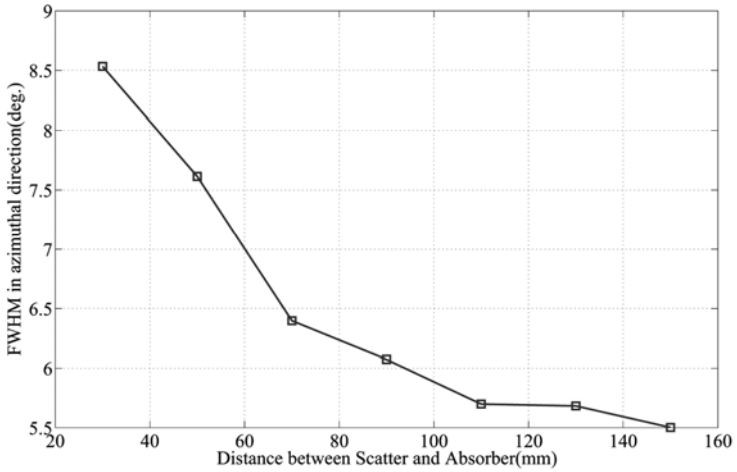

(a) Angular resolution in Azimuthal direction Vs. Gap distance using Geant4 simulation

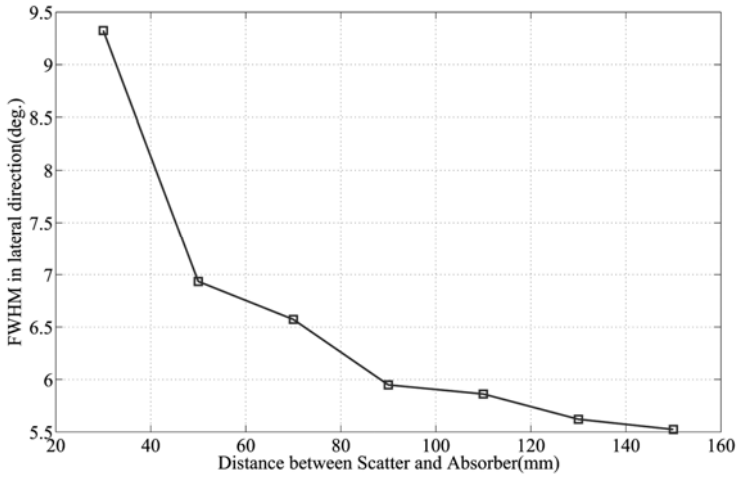

(b) Angular resolution in Lateral direction Vs. Gap distance using Geant4 simulation

Figure 3.17: Angular resolution Vs. Gap distance using Geant4 simulation.

incident photons summed with energy losses in the front plane.

3.3 Geant4 Simulation in CCM

3.3.1 Total Angular Resolution for Point Source

In Section 3.1.3, angular resolution due to geometry contribution of the proposed imager have been simulated and described. In this section, the energy resolution contribution and Doppler broadening contribution are presented. In this simulation, the Compton camera consisted of two 8×8 arrays of GAGG scintillator as the scatterer and absorber, respectively. The thicknesses of the crystals of scatterer and absorber were 5 mm and 10 mm. The gap distance was 80 mm and the distance from the source to the scatterer 100 mm. Gamma rays of 662 keV in energy were incident to the scatterer isotropically. FBP was used to reconstruct the images. The overall angular resolution is provided at the end of this section.

3.3.1.1 Energy Resolution Contribution

The energy information used for reconstruction was obtained by random sampling in a Gaussian probability distribution. The mean value of the Gaussian distribution was the exact energy deposition obtained through Geant4 simulation and the standard deviation was computed using Equation $\Delta E = 2.355 \times \sigma = 0.045 \times E + 9.01$ (keV). The reconstructed image is shown in Figure 3.18. The angular resolution in azimuthal and lateral direction are 4.88° and 4.83°, respectively.

3.3.1.2 Doppler broadening Contribution

The design and understanding of advanced Compton cameras depends critically on the capability of accurately accounting for Doppler broadening effects. In 2004, R. Marc Kippen proposed the first Monte Carlo package, G4LECS, that computes

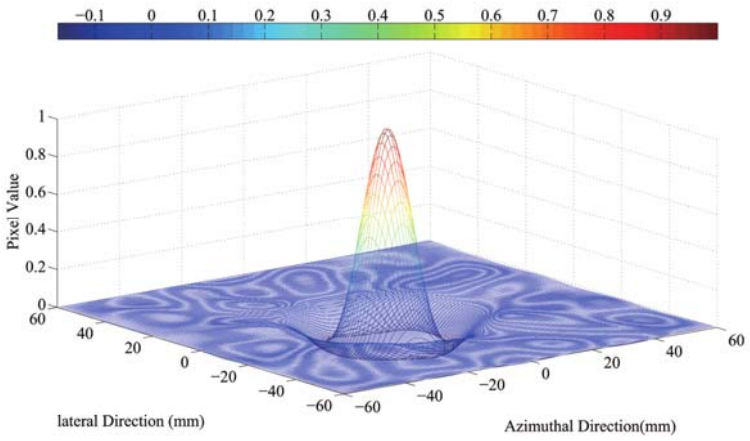

Figure 3.18: Point source image by only considering the energy resolution.

detailed Doppler broadening for use with the powerful, general-purpose Geant3 and Geant4 radiation transport codes [142]. From Geant4.9.2 on, the toolkit has been packaged with the G4LowEnergyCompton physics process that includes a treatment of Doppler broadening very similar to that provided by G4LECS. A set of models to describe the electromagnetic interactions of photons, electrons, hadrons and ions with material down to very low energies (eV scale), including the Geant4-DNA project, has been developed and maintained by the Geant4 Low Energy Electromagnetic Physics Working Group.

For simulating the Doppler broadening effect in our application, the Geant 4 Low Energy Electromagnetic was used. Accurate energy depositions and interaction positions were obtained and applied in the FBP reconstruction. The point source image is shown in Figure 3.19. The angular resolution in azimuthal and lateral direction are 4.81° and 4.87°, respectively.

3.3.1.3 Overall Angular resolution

The overall angular resolution is the quadratic summation of the three components, energy resolution contribution, Doppler broadening contribution, and geometry contribution. Therefore, the relationship between the total angular resolution and the

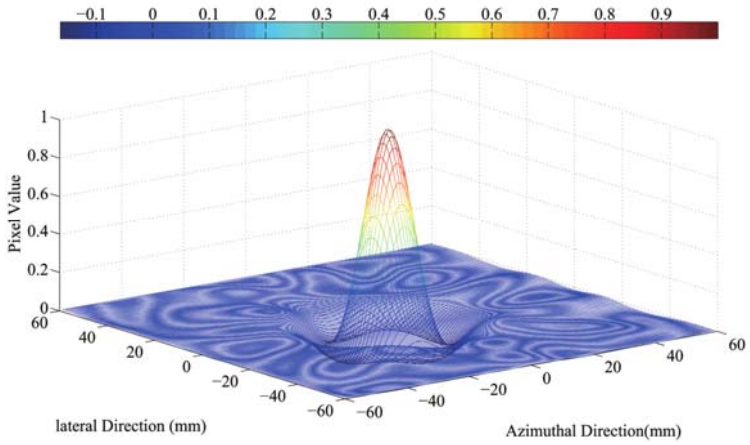

Figure 3.19: Point source image by only considering the doppler broadening effect.

gap distance can be computed and drawn as shown in Figure 3.20.

The results show that GAGG-based Compton camera is capable to achieve an angular resolution of ∼9° while the gap distance is 100 mm. Applying this Compton camera to build the wide area imager, a spatial resolution of ∼1.6 m is expected to be achieved while working CCM at an altitude of 10 m. This would be a huge improvement, Compared with reported results.

3.3.2 Diffuse Radiation Distribution

Imaging of distributed sources at different locations was simulated in order to demonstrate the capabilities of source localization in high background of the wide area imager. The input beam distribution of the Geant4 simulation was exactly the same as Figure 3.21 shows, which was measured by JAEA using a gamma plotter(ES-7410) [143] at 5 cm height along Ukedo river in Namie city in Fukushima prefecture. The emitted radiations were treated as gamma-rays of 662 keV in energy. The intensity of each point was set to be the measured dose rate.

In Figure 3.21(b), a rectangular coordinate system was built. The x axis is parallel to the azimuthal direction of the Compton camera, while the y axis parallel to the lateral direction. 0 point was flexibly set on the axis of the the detector. For

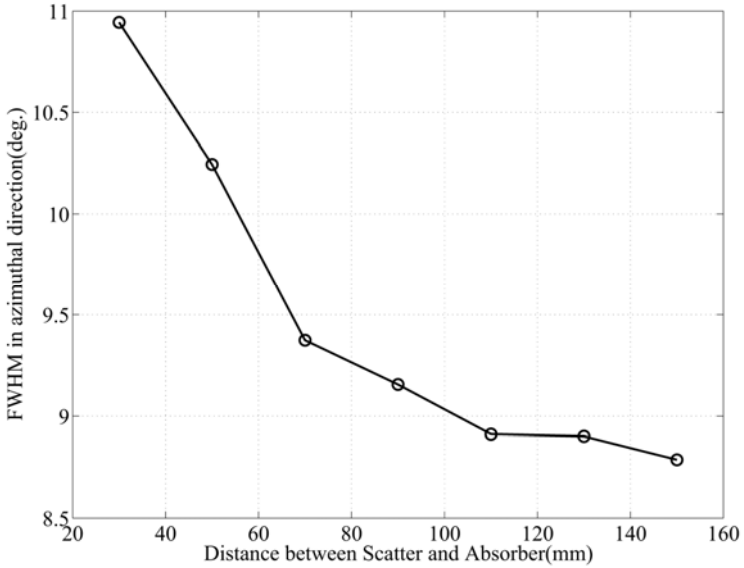

(a) Overal FWHM in Azimuthal direction

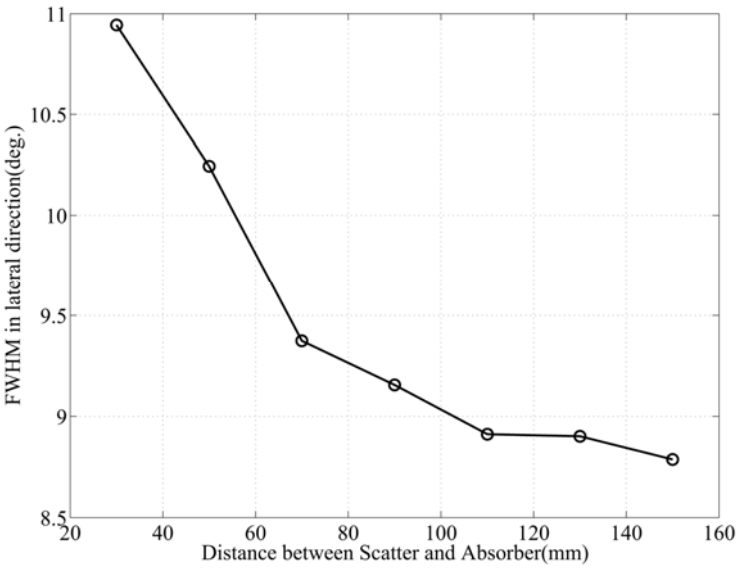

(b) Overal FWHM in Lateral direction

Figure 3.20: Overal FWHM Vs. Gap distance using Geant4 simulation.

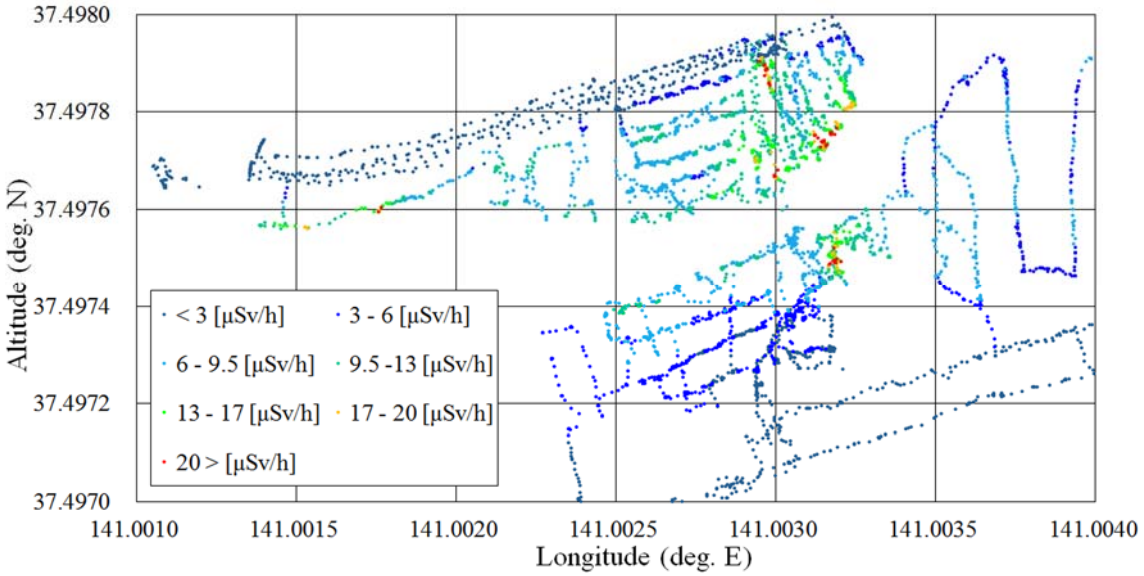

(a) Air dose rate distribution at 5 cm height measured by a gamma plotter(ES-7410)

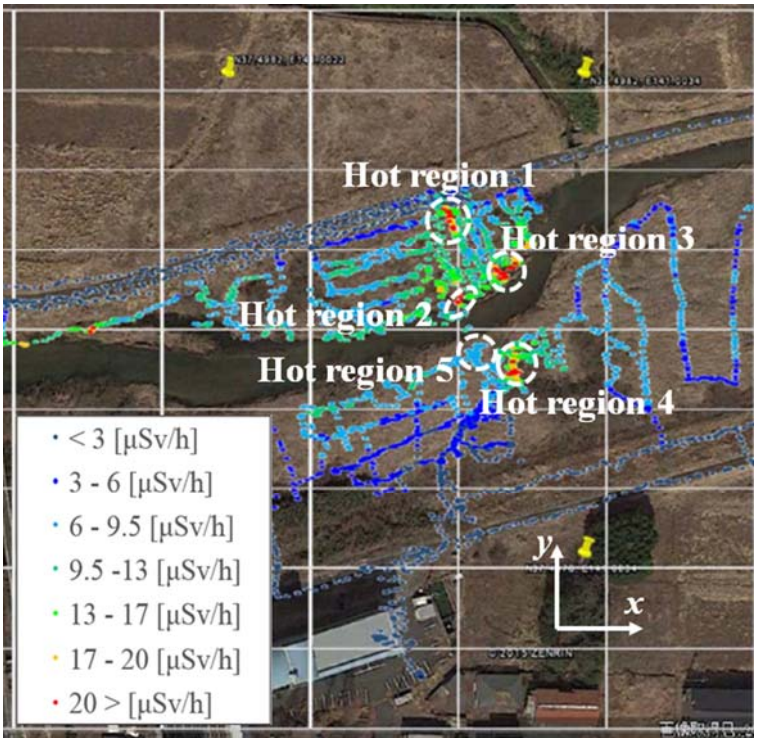

(b) Air dose rate distribution overlapped on Google Earth map

Figure 3.21: Air dose rate distribution at 5 cm height measured by a gamma plotter(ES-7410). This distribution is also the input of the beam for Geant4 simulation. The emitted radiations were treated as gamma-rays of 662 keV in energy. The intensity of each point was set to be the measured dose rate.

Region	Coordinates (m)
Hot region 1	(-3.1, 25.4)
Hot region 2	(0, 0)
Hot region 3	(11.9, 6.3)
Hot region 4	(15.9, -19.3)
Hot region 5	(4.2, -14.3)

Table 3.1: Coordinates of each region relative to region 2.

example, while the detector is on the top of hot region 2, the point with the highest measured air dose rate in region 2 was regarded as the point on the axis of the detector and set to be 0. Points with the highest measured air dose rates in other regions can be computed according to the measured altitude and longitude. Coordinates of each region relative to region 2 are show in table 3.1.

Simulations were implemented when the Compton camera was placed at the top of each hot region at an altitude of 10 m and 20 m, respectively. Coincidence event4 with energy threshold of 40 keV for both detector arrays were collected for filtered back projection. The energy uncertainties, interaction location errors as well as Doppler broadening effect were all taken into account for the reconstruction. Another point worth mentioning is that there are two small hot areas located in the northwest of hot region 2 that can be found in Figure 3.21(b) and would appear in the reconstructed images. Figure 3.22 are the images while the detector was at different locations and heights.

Shown in Figure 3.22(c) and Figure 3.22(c) were when the Compton camera was placed on the top of hot region 2. In these two images, the five hot regions rung out in Figure 3.21(b) were all clearly discovered. Images at 10 m height are clearer than those at 20 m height. However, Compton camera at higher altitude could receive higher fraction of photons from places other than area just under it, resulting in much lighter distribution in those places. In image 3.22(a) hot region 4 could not be identified due to the long distance to the Compton camera (41.6 m, 4 times longer

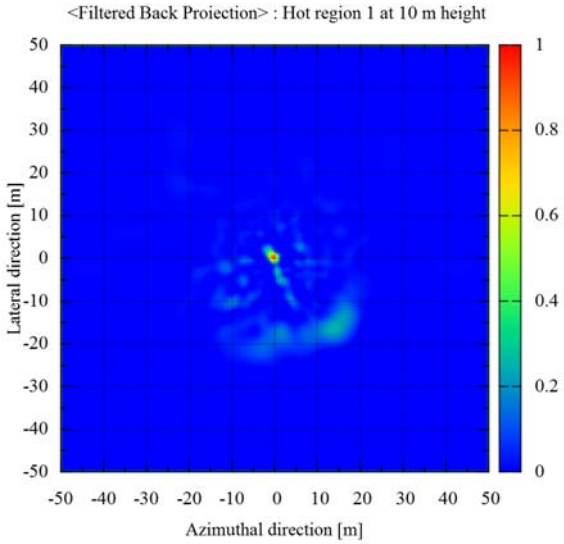

(a) Hot region 1 at 10 m height

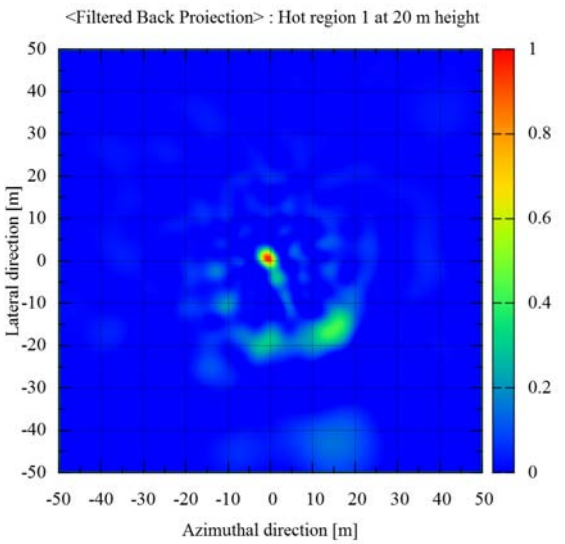

(b) Hot region 1 at 20 m height

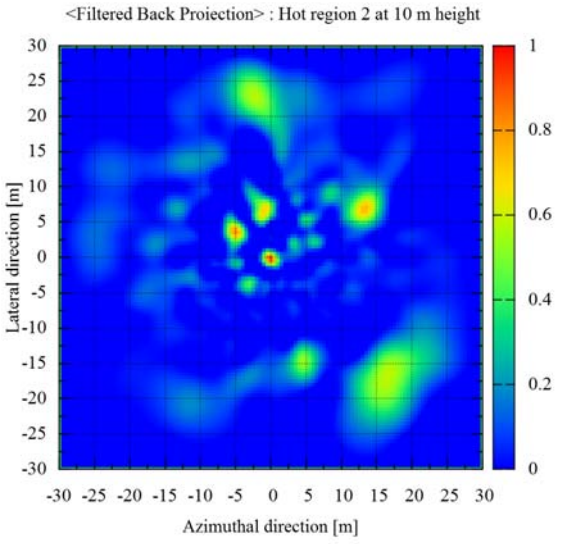

(c) Hot region 2 at 10 m height

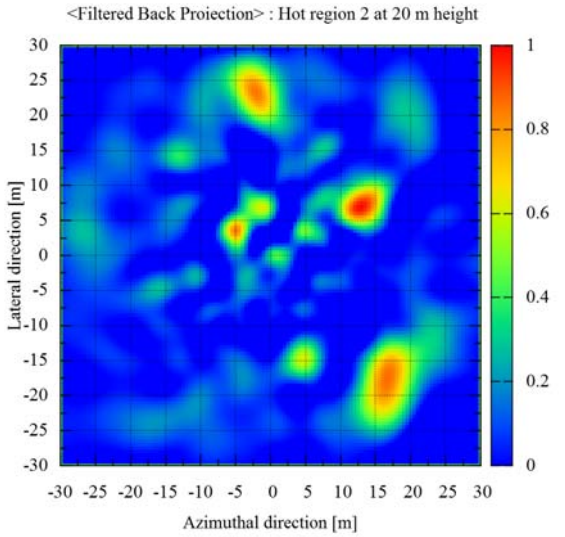

(d) Hot region 2 at 20 m height

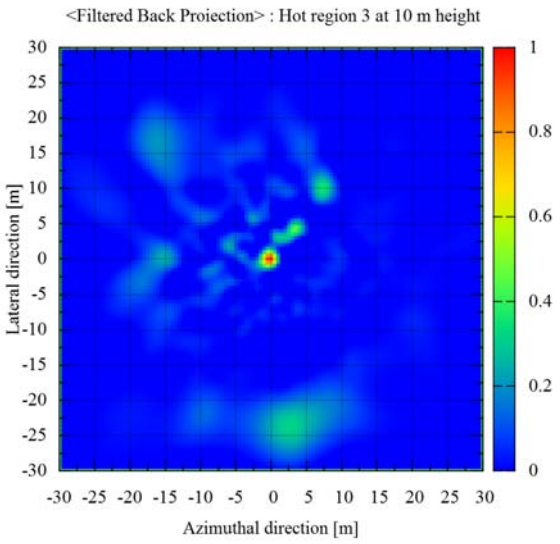

(e) Hot region 3 at 10 m height

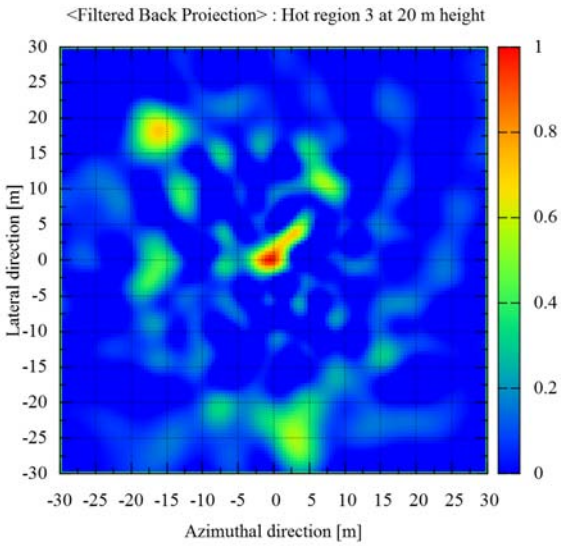

(f) Hot region 3 at 20 m height

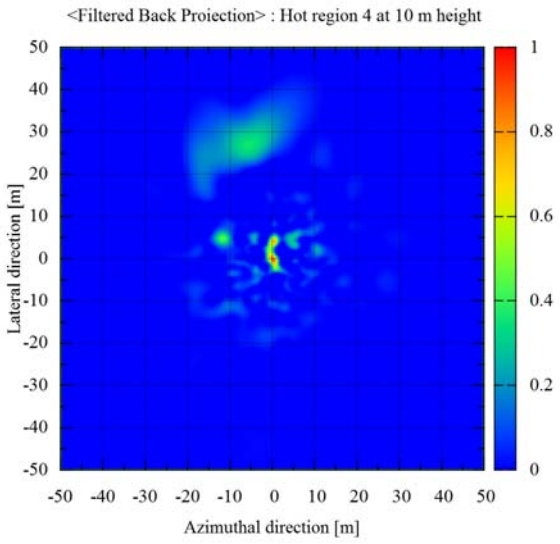

(g) Hot region 4 at 10 m height

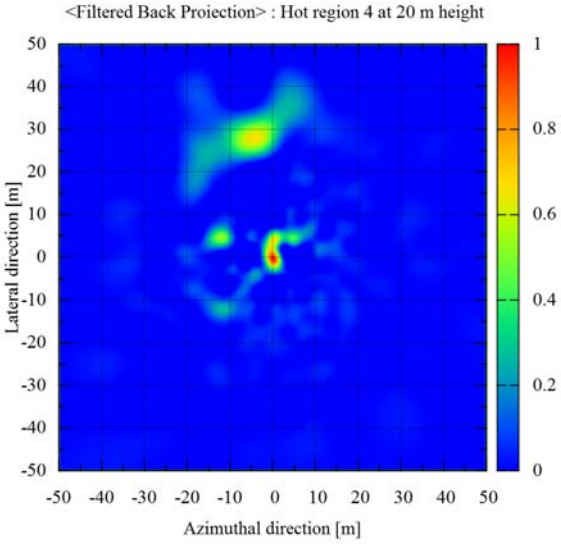

(h) Hot region 4 at 20 m height

Figure 3.22: Reconstructed images when the Compton camera was place at different hot regions at different heights.

than hot region 1), while in image 3.22(b), it was point out because the distance (45.0 m) was decreased to be 2 times longer than hot region 1. Another important reason why the Compton camera could recognize hot region 4 in image 3.22(b) was that hot region 4 was larger and have higher intensity than hot region 1. This was also the reason why the hot region 1 was not observed in image 3.22(h). Geant 4 simulations show very promising results for our proposed wide area imager to image diffuse distribution sources in field, although some simplifications were applied.

3.4 Geant4 Simulation in GCM

In Chapter II, we have introduced that the wide area gamma ray imager is designed to work in two modes. One is Compton camera mode by back projecting Compton cones to the image plane, the other one is Gamma camera mode that using coincidence count rates to map the radionuclides distribution as a function of position. In GCM, by only taking account the events whose energy losses on the scatter are in a certain energy range, due to the consideration of the relationship between E_s and Compton scattering angle, the spatial resolution is expected to be further improved.

In this section, Geant4 simulation to assess the idea of GCM working modes is reported. The performance of a Compton camera that works in GCM is studied, described, and compared with a single array detector that also works in GCM. We use SDM as the short for single array detector working in GCM. Figure 3.23 are the setups for the simulation.

The Compton camera consisted of two detector arrays, of which the front plane was composed by a 8 $\times$ 8 array of 10 mm $\times$ 10 mm $\times$ 5 mm GAGG scintillators and the back plane was comprised of a 8 $\times$ 8 array of 10 mm $\times$ 10 mm $\times$ 10 mm GAGG scintillators. The gap distance between was 80 mm. A point source was placed at 17 different positions along a line which is parallel to the azimuthal direction of the Compton camera. The ninth position just located on the axis of the detector.

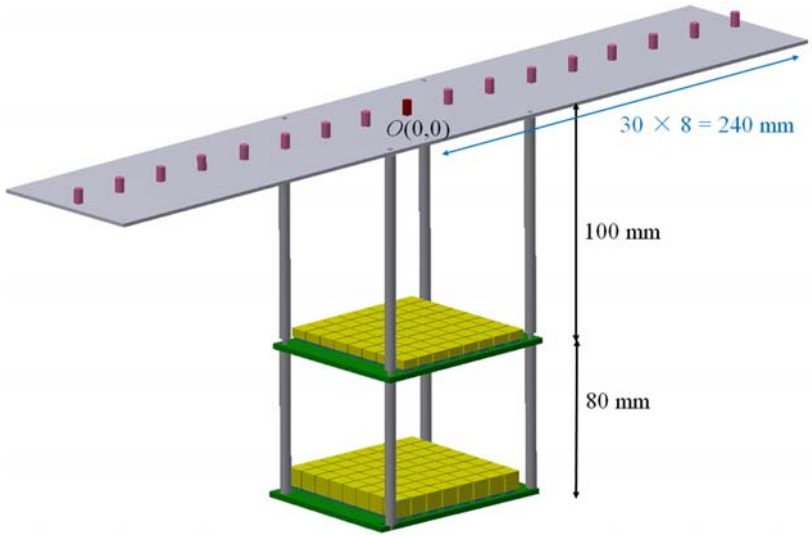

(a) Compton camera working in GCM

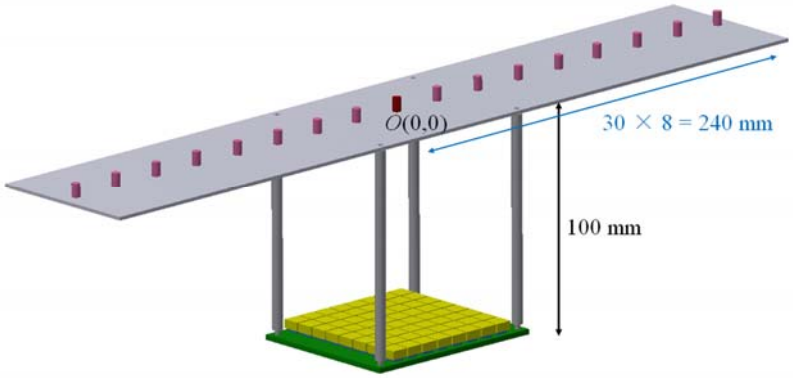

(b) SDM

Figure 3.23: The setups of a Compton camera working in GCM and SDM.

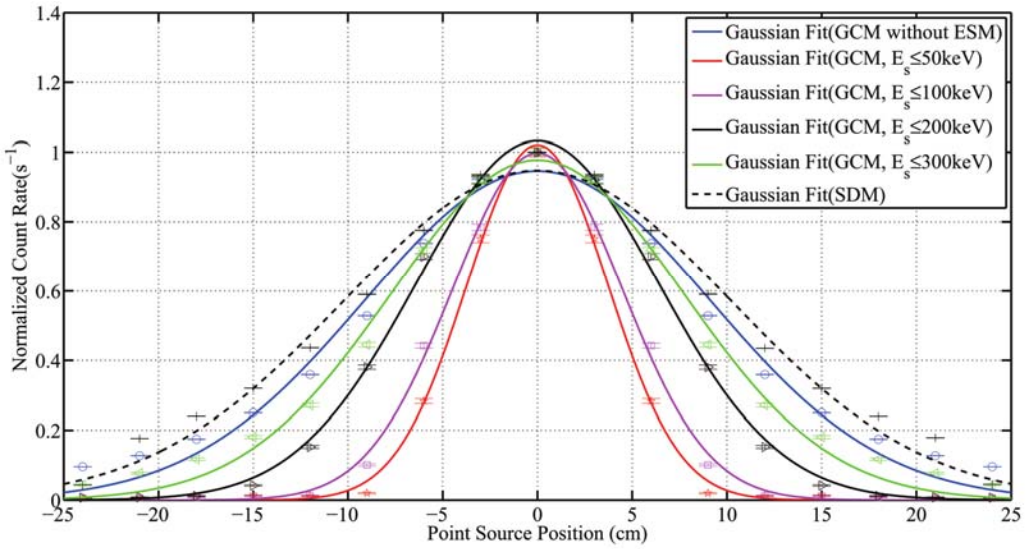

Figure 3.24: Count rates as a function of the point source position in different modes.

The separation distance between two locations was 30 mm. Coincidence events were recorded while the source was at different locations. The distance from the source to the front plane was 100 mm.

For SDM, the detector array was exact the same as the front detector plane of the Compton camera described above. The interaction events were also recorded when the point source was placed at the same 17 locations.

ESM were applied in the analysis of data obtained in GCM. 4 different upper limits of energy losses on the scatter were selected and the results are shown in Figure 4.13. The spatial resolutions when the upper limit was 50 keV, 100 keV, 200 keV, 300 keV and without ESM applied were 8.8 cm(FWHM), 10.6 cm(FWHM), 15.0 cm(FWHM), 18.2 cm(FWHM) and 21.4 cm(FWHM) respectively. And the spatial resolution in SDM was 24.0 cm(FWHM). In GCM with ESM applied, the spatial resolution can be largely improved compared with that in SDM. If a Compton camera with the same performance is equipped on an unmanned helicopter and applied in field to locate radioactive materials, it is estimated that the spatial resolution of this prototype detector could achieve 8.8 m(FWHM)while the altitude of the system is

10 m, while it is 24.0 m(FWHM) in SDM. The spatial resolution was improved by 3 times better by employing ESM in GCM compared with SDM.

CHAPTER IV

A Prototype of Wide Area Gamma-ray Imager

For the first step, a prototype of the proposed Wide Area Gamma-ray Imager was designed and fabricated. For the Compton camera of the prototype imager, 32 Ce:$Gd_3(Al,Ga)_5O_{12}$(GAGG) crystals were coupled to 16 silicon photomultipliers and 16 avalanched photodiodes as the scatterer and absorber, respectively. The performance of the system was fully characterized in both GCM and CCM. In this Chapter, the design, fabrication, evaluation, as well field as tests are introduced.

4.1 Design and Fabrication of the Prototype System

As discussed in Chapter II and Chapter III, GAGG crystals with 10 mm × 10 mm × 5 mm and 10 mm × 10 mm × 10 mm in size are decided to be applied as the scatterer and absorber detectors, respectively. The photo detectors, used to collect the visible photons and convert them to electronic signals for front-end electronics, should be appropriately chosen. In this section, the comparison of different photon detectors will be firstly given. After that, the linearity and dynamic range of the specific electronics for this system will be described, followed by an introduction of the whole structure of the prototype system.

4.1.1 Photo Detectors

Since this proposed system is going to be applied in field, where the temperature might have huge differences in different seasons, or even in different days. In order to ensure the system having a stable performance, the photon detectors chosen are expected to have a low temperature dependence. In addition, equipped in an unmanned helicopter, the detector itself will be charged by batteries. In this case, the lower the power consumption of the system is, the longer the measurement time can be. Furthermore, the signal to noise ratio of the photo detectors should be also taken into consideration in order to obtain high energy resolution. In summary, temperature dependence, power consumption and the signal to noise ratio are the three benchmarks for selecting the proper photon detector.

Currently, the most popular available photon detectors are PD, APD and SiPM. The amplitude of the output signal of a typically PD(Hamamatsu, S3590-08) coupled to GAGG at 662 keV is calculated as,

$$v_o = 0.662\text{keV} \times 57000\text{photons/MeV} \times 80\% \times 1.6 \times 10^{-19}\text{C/photon} \approx 4.8 \quad \text{fC} \tag{4.1}$$

here, the photon collection efficiency is assumed to be 80% [144]. With this amplitude, an Equivalent Noise Charge(ENC) [145]of 637 electrons in root mean square(rms) of the front-end electronics should be realized if an energy resolution of 5% is demanded at 662 keV, as shown in table 4.1.

Expected Energy resolution at 662 keV	ENC in rms (electrons)
5%	637
10%	1274

Table 4.1: Expected ENC level when PD is used as the photon detectors.

Unfortunately, at the moment when we planned to fabricate the prototype sys-

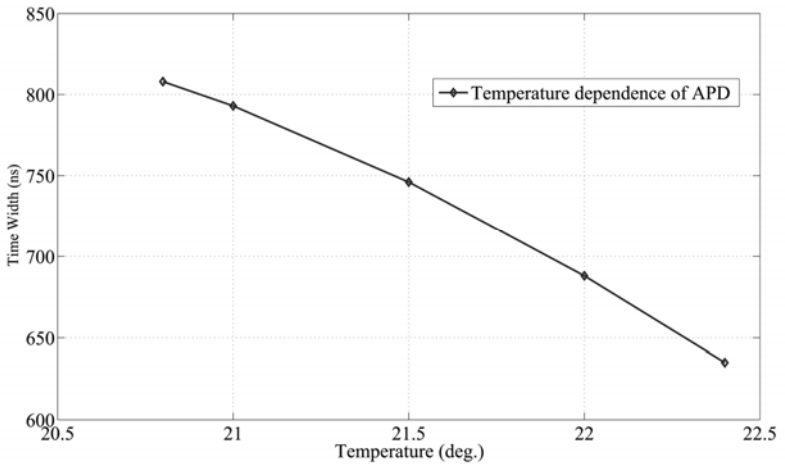

Figure 4.1: Temperature dependence of APD(Hamamatsu, S8664-55).

tem, there were no electronics that can achieve such low ENC level at hand in our lab. Therefore, PD is filtered due to the low signal to noise level. While for APD(Hamamatsu, S8664-55) and SiPM(KETEK, PM6660), a relatively high signal to noise level could be easily achieved due to their high gain, ∼50 and ∼10^7 for APD and SiPM respectively. However, for the same reason, the performance of the gain of APD and SiPM are both temperature dependent.

Temperature dependence of both APD and SiPM were measured using SH-242 temperature and humidity chamber. The results are shown in following figures.

In Figure 4.1, the y axis denotes the DToT time width. The power supply for the APD is +435V. The calculated temperature dependence is ∼15% per degree. While as shown in Figure 4.2, the dependence is 1∼2% at room temperature with a power supply of -28.5 V for SiPM. Standing at the point of temperature dependence, SiPM is superior to APD.

However, ASICs with DToT method integrated for APD [146]were designed and fabricated, while only printed circuit boards with discrete components were available for SiPM at that time. The power comsumption of the ASIC is ∼ 100 mW for 16 channels while that of discrete circuits is ∼ 300 mW. Figure 4.3 is the schematic of one channel in the APD ASIC.

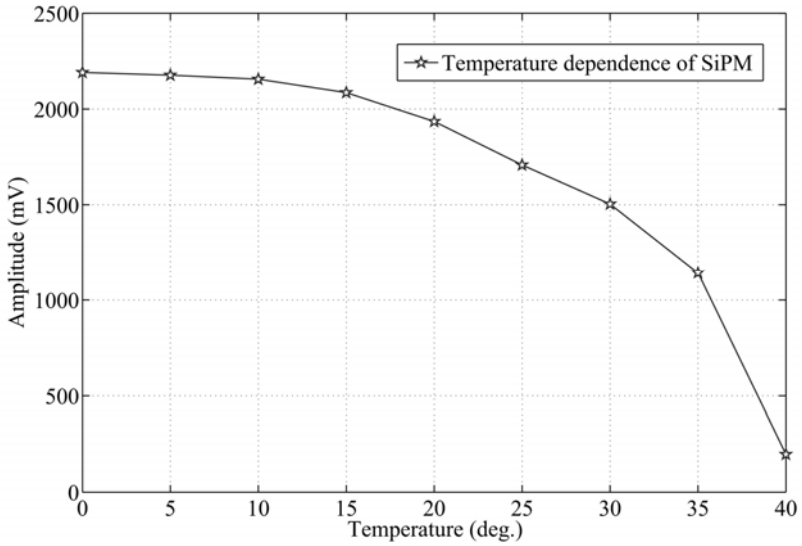

Figure 4.2: Temperature dependence of SiPM(KETEK, PM6660).

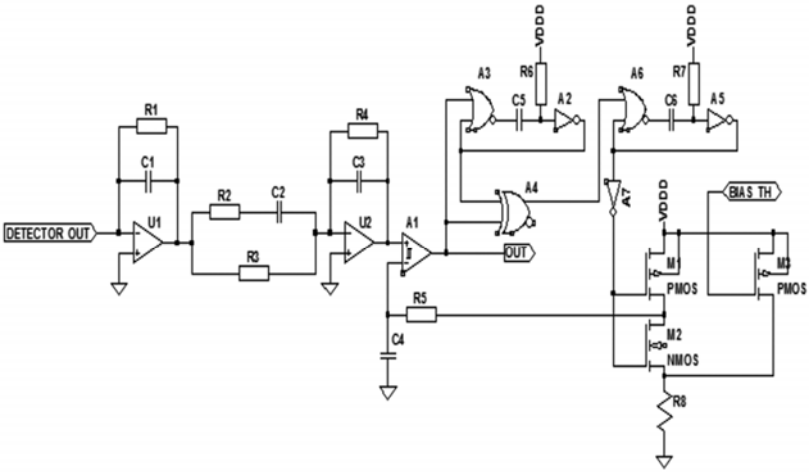

Figure 4.3: Schematic of one channel in APD ASIC.

Finally, as a tradeoff, SiPM was chosen as the photon detectors for scatterer crystals for achieving more accurate energy information with lower temperature dependence and APD for absorber crystals for low power consumption by employing the ASICs.

4.1.2 Front-end Electronics

As mentioned in last section, discrete circuits(4×4 channels) and ASICs were employed as the front-end electronics for SiPM and APD, respectively. Both are with DToT method integrated to convert CR-RC shaping signals to digital signals for multi-channel spectra and coincidence acquisition. Figure 4.4 shows the linearity between the amplitude of input waveform and time width of the digital signal of the discrete circuits. Amplitude of the signal from a SiPM with a 1 kΩ shunt resistor and 29 V power supply is around 86 mV at 662 keV. A spectrum of ^{137}Cs source was also obtained (see Figure 4.5) with an energy resolution(FWHM) of 6.5% at the photopeak. The energy resolution(FWHM) was around 9% at 662 keV for APD with GAGG scintillator. The total power consumption of the system including the DAQ, was 1125 mW.

4.1.3 Prototype System

The whole structure of the prototype system is given in Figure 4.6. In this structure, a box containing the Compton camera, a computer with the data logger installed and a Wi-Fi module, is mounted on the AUH. A GPS module is also mounted on the helicopter and capable of offering three dimension position information of the helicopter. Then all the information is sent to the computer in the box via a USB connection. Through the Wi-Fi module, the coincidence count rate and GPS information are also sent to the ground station which can be used to check whether the system is working correctly in real time. Figure 4.7 is a diagram of the prototype

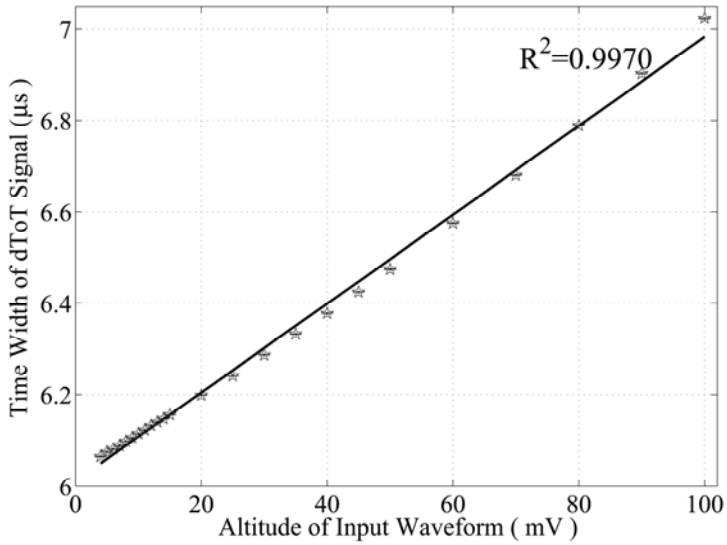

Figure 4.4: Linearity between the amplitude of input waveform and time width of the digital signal of the discrete circuits.

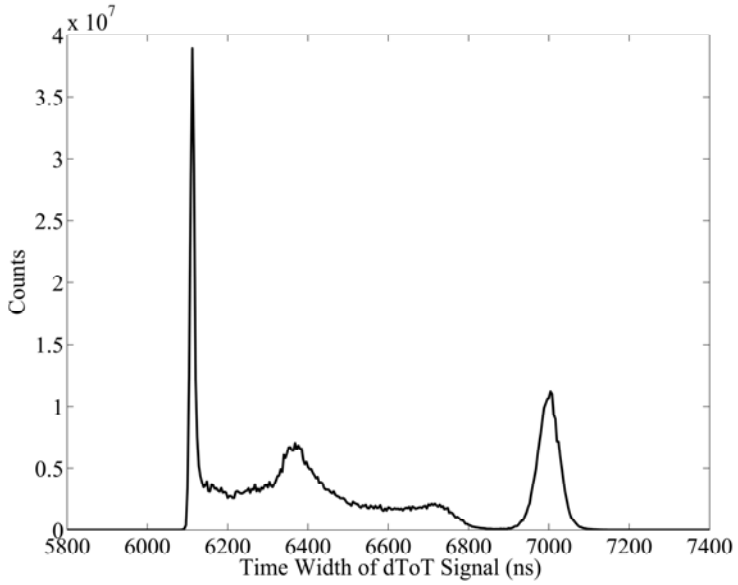

Figure 4.5: Spectrum of ^{137}Cs.

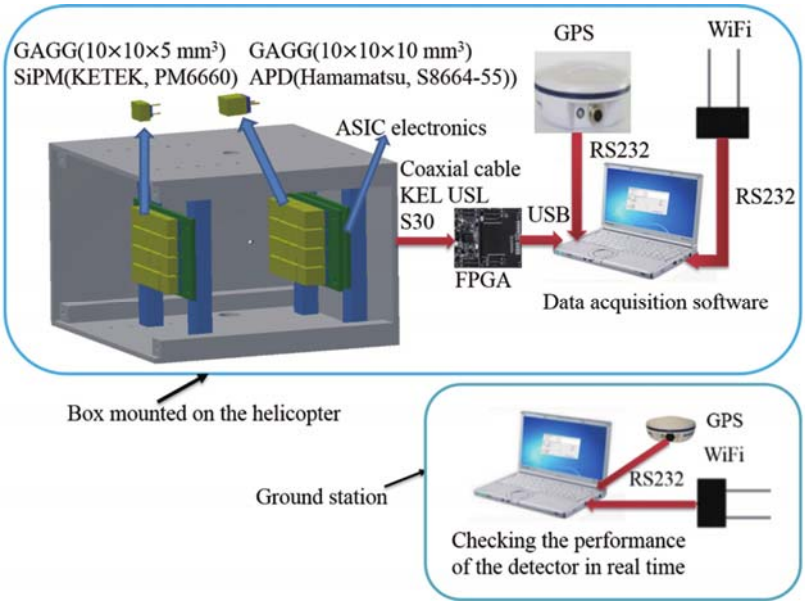

Figure 4.6: Structure for the prototype detector system.

system.

4.2 Experimental Results in the Lab

4.2.1 Experiments in CCM and Results

Firstly, the relationship between the intrinsic efficiency and the distance from the scatter array to the absorber array was measured. A ^{137}Cs source(2.5 mm in diameter × 8 mm in height, 1 MBq activity) was placed at position O as shown in Figure 4.8, whose center was 109.5 mm away from the center of the scatter. The distance between the two arrays was changed from 32.5 mm to 68.5 mm. The coincidence time window was set to be 1.2 μs. The efficiency was the largest, 1.68±0.04% at 662 keV, while the distance was 32.5 mm and decreasing while the distance increased as shown in Figure 4.9.

Then, the ^{137}Cs point source images were obtained while the distance between the two detector arrays was set to be 32.5 mm. The source was placed at three different positions (20°, 20°), (0°, 0°), (-20°, -20°) and the reconstructed images are

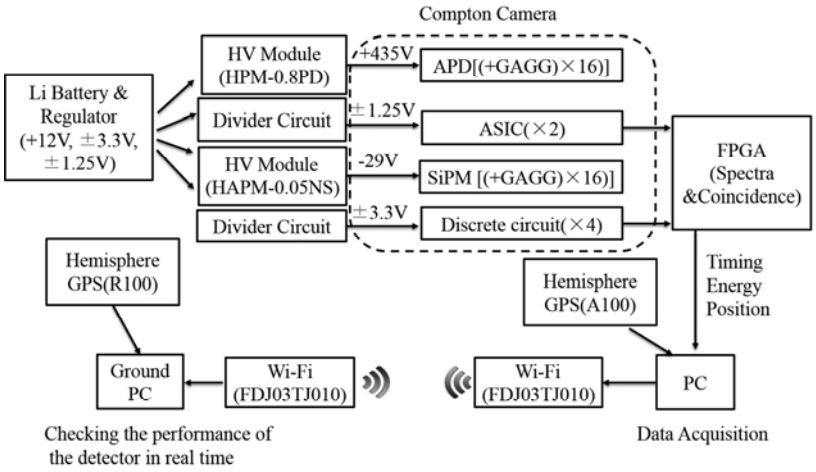

Figure 4.7: Diagram of the prototype detector system.

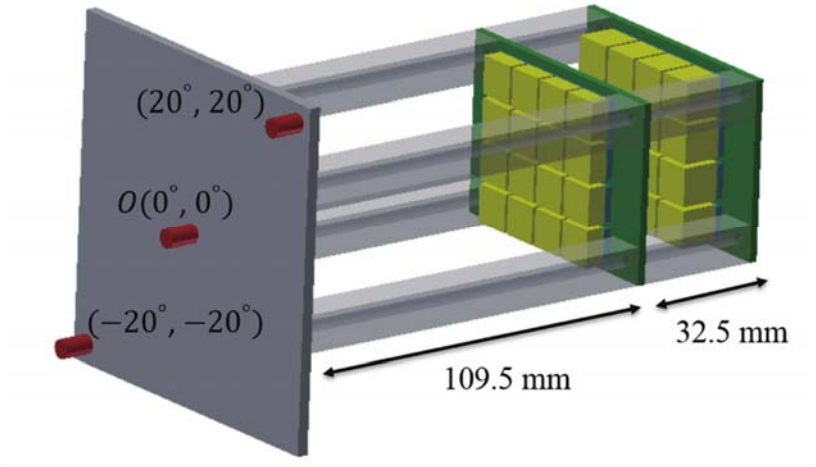

Figure 4.8: Point source imaging experiment setup.

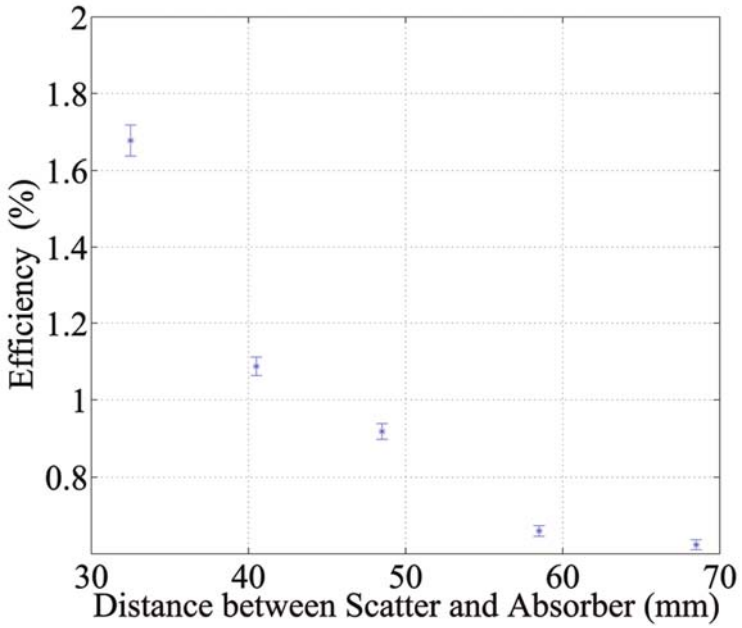

Figure 4.9: Relationship between the intrinsic efficiency and the distance from the scatter array to the absorber array.

shown in Figure 4.10. Here, FBP was applied for the reconstruction. The angular resolution(FWHM) of the images are 14.8°, 13.9° and 16° respectively. With this angular resolution, the prototype wide area imager is expected to achieve a spatial resolution of 2.4 m at the position under the detector while it is working in CCM at an altitude of 10 m.

The dependence of the angular resolution on the distance between the two detector arrays were also measured, as shown in Figure 4.11. As the distance increases, the angular error decreases. The angular resolution is the best, 11.2°, when the gap is 67.5 mm.

4.2.2 Experiments in GCM and Results

Experiments in GCM were carried out to demonstrate its feasibility. The distance between the two arrays was set to be 32.5 mm. The same ^{137}Cs source was placed at 15 different positions which were on a line parallel with and 112.3 mm away from the surface of the scatter, as shown in Figure 4.12. Measurements in SDM were also

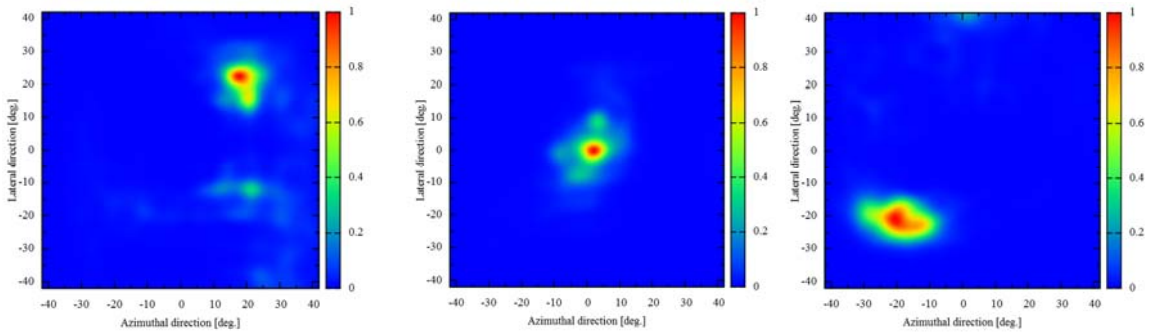

(a) Point source image while the source was put at position (20°, 20°)

(b) Point source image while the source was put at position (0°, 0°)

(c) Point source image while the source was put at position (-20°, -20°)

Figure 4.10: Point source images while the source was place at three different locations.

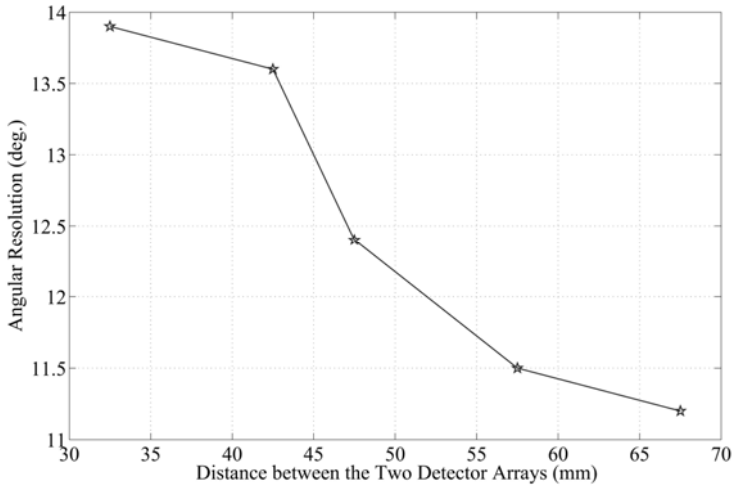

Figure 4.11: Relationship between the angular resolution and the distance from the scatter array to the absorber array.

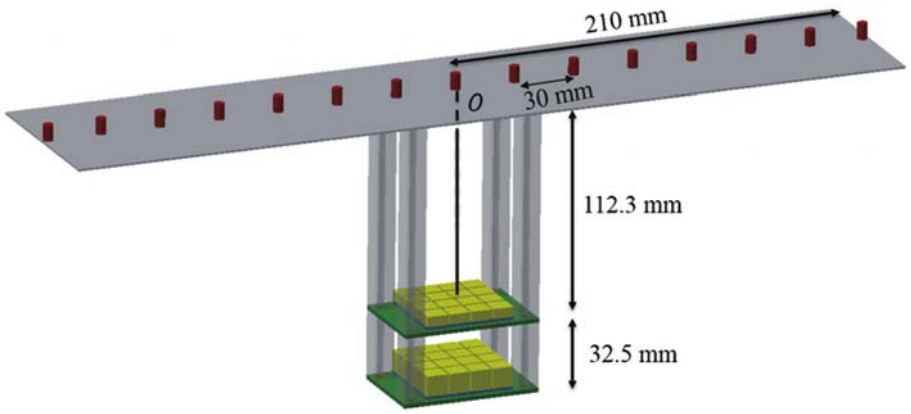

Figure 4.12: Experiment setup in the Gamma-camera mode.

done while the source was placed at these 15 positions. ESM were applied in the analysis of data obtained in GCM. 4 different upper limits of energy losses on the scatter were selected and the results are shown in Figure 4.13. The spatial resolutions when the upper limit was 50 keV, 100 keV, 200 keV 300 keV and 662 keV(without energy selection) were 10.7 cm(FWHM), 11.7 cm(FWHM), 16.0 cm(FWHM), 19.9 cm(FWHM) and 20.2 cm(FWHM) respectively. And the spatial resolution in SDM was 27.5 cm(FWHM). In GCM with ESM applied, the spatial resolution can be largely improved compared with that in SDM. It is estimated that the spatial resolution of this prototype detector could achieve 9.5 m(FWHM) in field while the altitude of the system is 10 m, while it is 24.5 m(FWHM) in SDM.

4.3 Experimental Results in Field

Field experiments at Namie in Fukushima prefecture were carried out on April 22nd and 23rd, 2014 using this prototype system. The purpose of this test was to demonstrate the wide area imaging capability of the developed prototype imager with high spatial resolution. Figure 4.14 shows the place where the measurements were done and gives the air dose distribution measured by a Ce:$LaBr_3$ detector mounted on an unmanned helicopter at an altitude of 80 m by Japan Atomic Energy Agen-

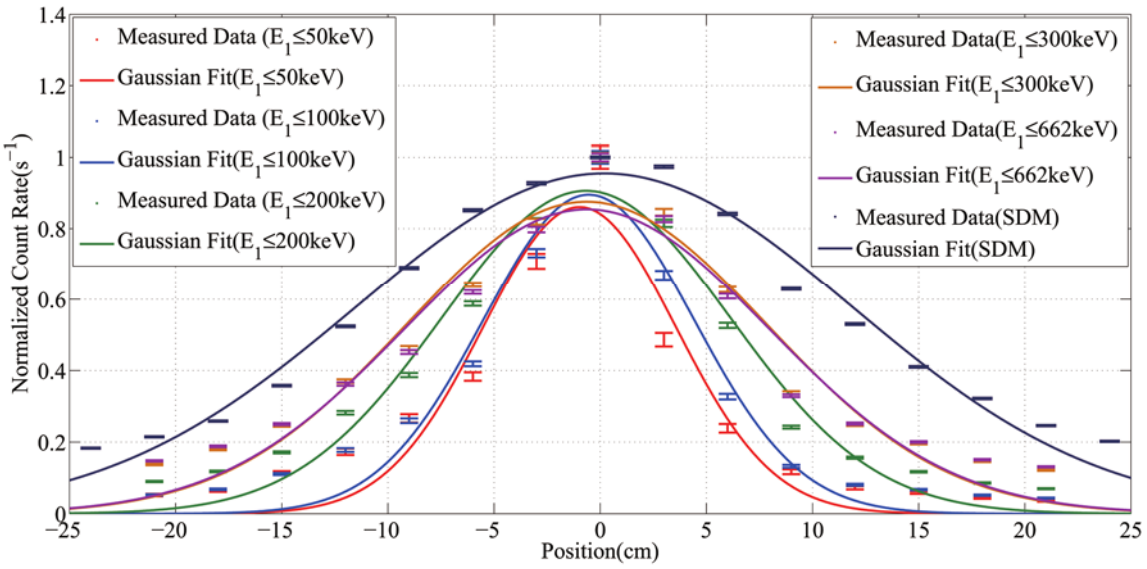

Figure 4.13: Results of the lab experiment in Gamma-camera mode.

cy(JAEA).

4.3.1 Experimental Results in GCM

In this section, we focus on the discussion of the experimental results in GCM and SDM. In SDM, the total count rate of the 16 channels were recorded to map the radiation distribution. In Figure 4.15, the straggled colorful dot are the air dose rate through ground measurements results by a gamma plotter(ES-7410) [143], whose accuracy is within 4%. The black line is the flight route at 10 m height. In order to do detailed analysis, 6 elliptic areas are selected and numbered from 1 to 6. Area 1 and 2 are almost with dose rates lower than 5 μSv/h while area 3 around 5 μSv/h to 9 μSv/h. Area 4, 5, and 6 are the hottest parts with dose rates higher than 11 μSv/h. The point with highest dose rate in area 6 is about 6.5 m away from the road where the radioactivity is quite low.

The ground truths showed in Figure 3.21 and Figure 4.15 were obtained using the same gamma plotter in the same place in February, 2015 and April, 2014 , respectively. Hot regions 1, 2, 3 in Figure 3.21 correspond to hot areas 6, 4, 5 in Figure 4.15,

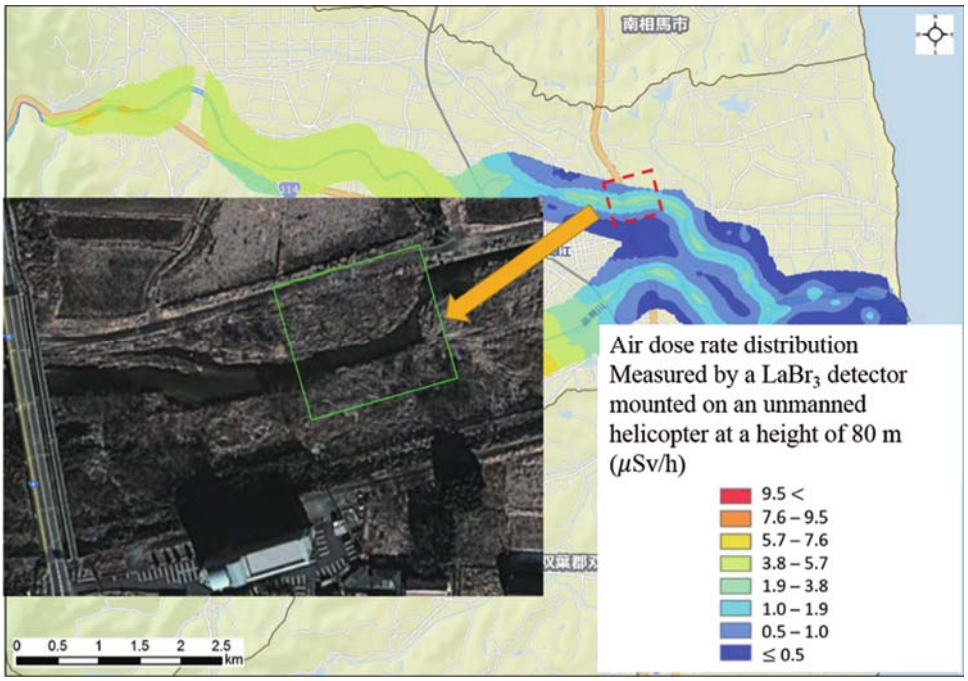

Figure 4.14: The place indicated in the green square was the place where the field experiment was carried out and the rough distribution of air dose rate was shown.

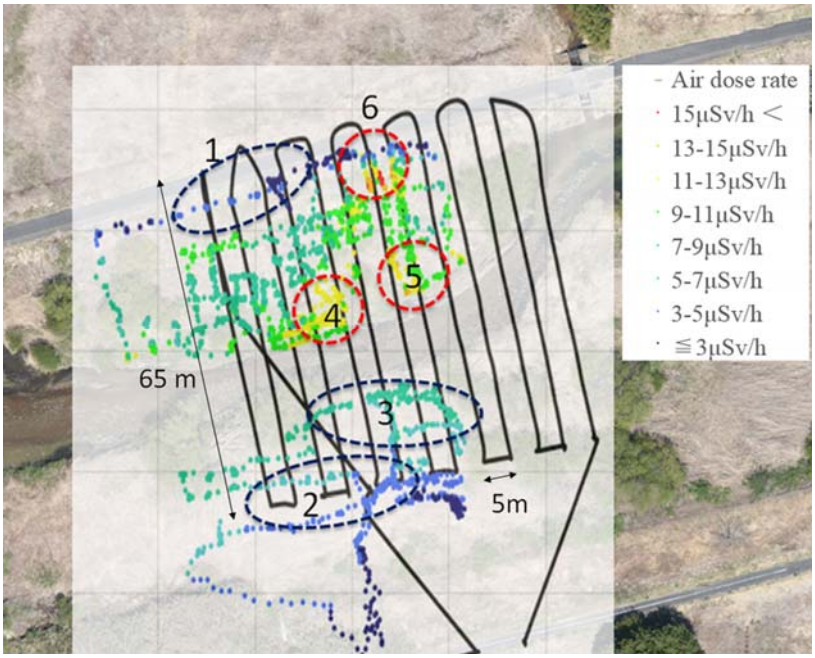

Figure 4.15: Ground measurement results of the air dose rate at 1 m height and the flight route at 10 m height. 6 elliptic areas were selected in order to do detailed analysis.

respectively. Hot region 4 in Figure 3.21 is absent in Figure 4.15, and this shows that the radiological and nuclear materials deposited in Fukushima are transporting which is mentioned in Chapter I.

Measurements were done via programmed flights at the speed of 1 m/s at an altitude of 10 m, 20 m and 30 m. The detection area is 60 m × 65 m, while the space interval between two neighboring routes was set to be 5 m at 10 m height(measurement time = 20 mins) and 10m at the other two heights(measurement time = 10 mins).

Figure 4.16(a)∼Figure 4.16(f) shows the images obtained under the two modes at 10 m, 20 m ,and 30 m height respectively and Figure 4.16(g)∼ Figure4.16(i) shows the images in GCM with ESM employed. Those images are obtained based on the measured count rates using Kriging interpolation by ArcGIS software. Because not enough counts at amplitude of 20 m, 30m were obtained, higher energy threshold were set for events selection. Image 4.16(a)∼image 4.16(c) are obtained in SDM, and their spatial resolution are calculated to be 24.5 m(FWHM), 49.0 m(FWHM) and 73.5 m(FWHM) respectively. In SDM, the contribution to the count rate of one hot spot is effected only by the solid angle from the source to the surface of the detector. Hot areas 4, 5 and 6 can not be identified in these three images, and the image is getting rougher while the altitude increases. In GCM, not merely the solid angle, but also the combination of the detector is effecting the contribution to the count rate of one hot spot. As a result, the spatial resolution is improved. In image 4.16(d), hot areas of 4 and 5 are somehow separated. With ESM applied, hot areas 4 and 5 are successfully separated in image 4.16(g). Low count rates are also obtained in the cold area 1, 2, and 3. In image 4.16(g) which has the best spatial resolution, area 6 still can not be exactly identified because the area is narrow($\sim 1 \times 2$ m^2) and the spatial resolution is beyond the distance to the road where the radioactivity is low.

Figure 4.17 performs the count rate vs the measured air dose rate by gamma plotter. From the comparison, the increasing of the count rate is the fastest in GCM

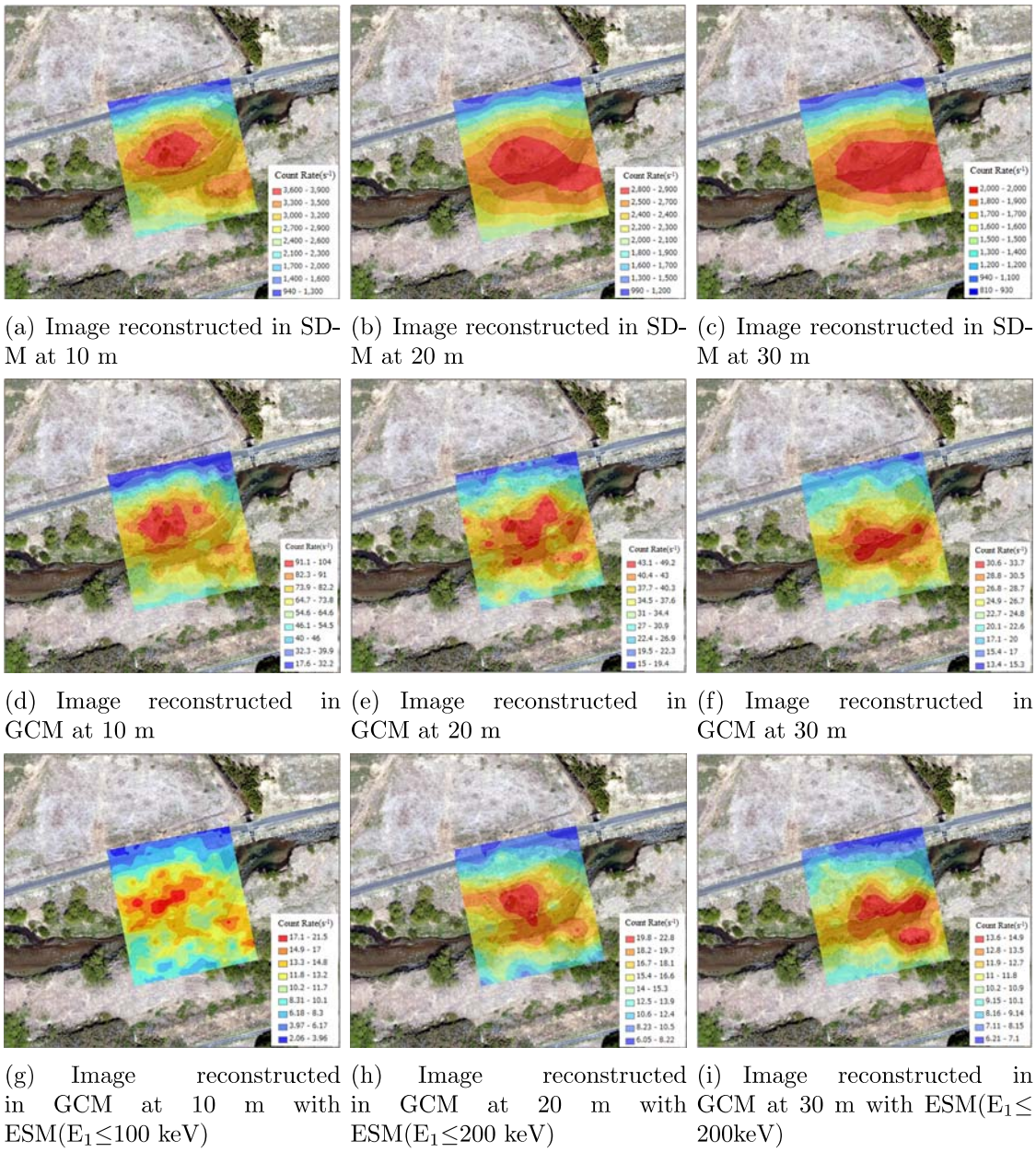

(a) Image reconstructed in SDM at 10 m

(b) Image reconstructed in SDM at 20 m

(c) Image reconstructed in SDM at 30 m

(d) Image reconstructed in GCM at 10 m

(e) Image reconstructed in GCM at 20 m

(f) Image reconstructed in GCM at 30 m

(g) Image reconstructed in GCM at 10 m with ESM($E_1 \leq 100$ keV)

(h) Image reconstructed in GCM at 20 m with ESM($E_1 \leq 200$ keV)

(i) Image reconstructed in GCM at 30 m with ESM($E_1 \leq$ 200keV)

Figure 4.16: Images reconstructed via count rate(s^{-1}) using Kriging interpolation in (a)SDM at 10 m; (b)SDM at 20 m; (c)SDM at 30 m; (d)GCM at 10 m; (e)GCM at 20 m; (f)GCM at 30 m; (g)GCM at 10 m with ESM($E_1 \leq 100$ keV); (h)GCM at 20 m with ESM($E_1 \leq 200$ keV); (i)GCM at 30 m with ESM($E_1 \leq$ 200keV).

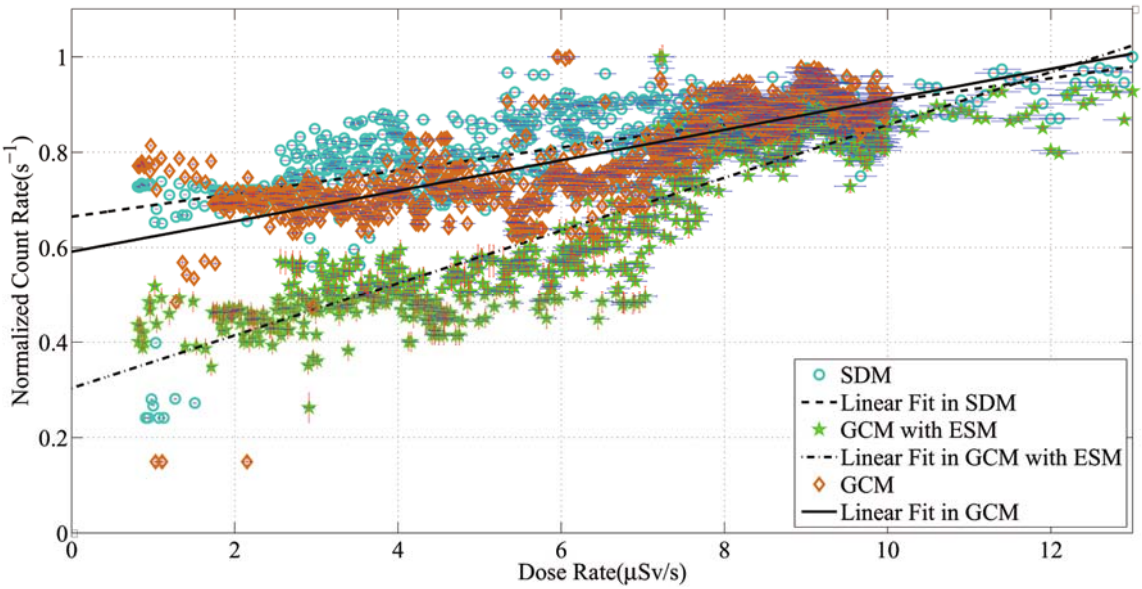

Figure 4.17: Count rate vs. dose rate in different modes.

with ESM ($E_1 \leq 100$ keV) applied, while it is the slowest in SDM. This also shows that the detector in GCM with ESM applied is with the highest spatial resolution. Considering the spatial resolution in Figure 4.16(g), the expected count rate of hot area 6 was estimated using the relation in Figure 4.17. Considering the uncertainties of measured dose rate, count rate and the fitting, the expected count rate was 10.8±1.6 cps while the detected count rate was 9.9±1.3 cps.

4.3.2 Experimental Results in CCM

Hovering flights were also carried out to study the performance of this prototype system working in CCM. Coincidence events were recorded while the helicopter carrying the Compton camera hovering on the top of hot area 5 at an altitude of 10 m and 20 m. Measurement time was both 15 mins. Reconstructed images using FBP are shown in Figure 4.18.

The system successfully pointed out hot area 4 and 5 as shown in the images. Although the images were not as clear as those obtained in simulation works, this was

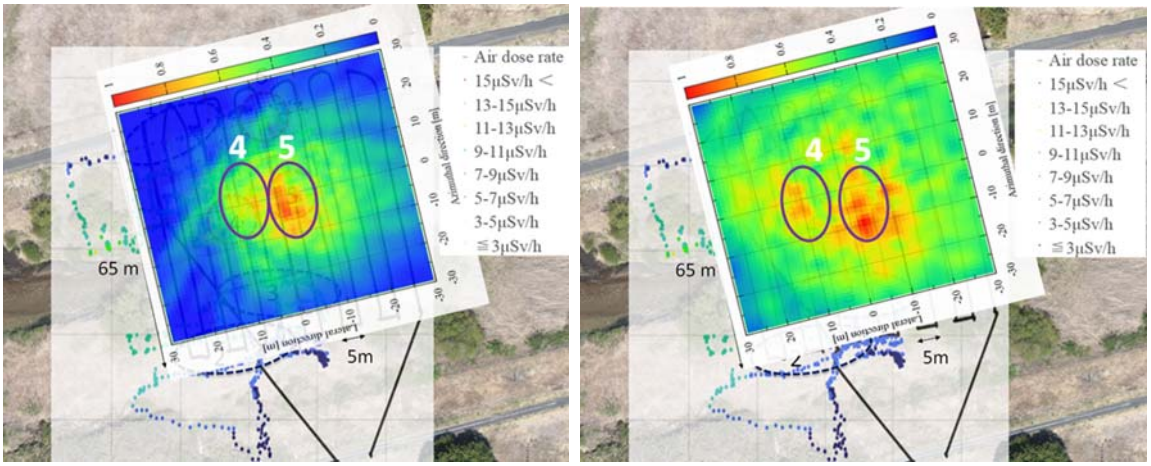

(a) Altitude = 10 m (b) Altitude = 20 m

Figure 4.18: Filtered back projected images while the prototype system was hovering on the top of hot area 5. Shown in the left was when the altitude was 10 m.

by far, the first successful application of a Compton camera in airborne measurements. Since the spatial resolutions at hot area 6 were 6.6 m and 7.8 m at altitude of 10 m and 20 m respectively, and both of the resolutions were longer than the distance from hot area 6 to the very cold area, road, it was not observed in both images. And from the comparison of the images, we could conclude that, as the altitude increases, the system was tend to see more wide areas at the expense of decrease of spatial resolution, which is consistent with the simulation results in Chapter III.

4.4 Summary

In this chapter, a prototype system with high resolution for detecting the distribution of the radioactive isotopes in a wide area is proposed and developed. A GAGG based Compton camera mounted on an unmanned helicopter was designed to detect and localize radioactive sources. The prototype system achieved an efficiency of 1.68%±0.04% and an angular resolution of 13.9°(FWHM) while working in CCM in the experiment at the laboratory. In GCM with ESM applied, a spatial resolution

of 10.7 cm(FWHM) was obtained when the distance of the detecting area is 11.2 cm away from the detector while it was 27.5 cm(FWHM) in SDM. In addition, dToT was applied to Compton camera for signal processing to achieve low power consumption and digitalization.

Field experiments were carried out in Fukushima prefecture and results obtained demonstrate the system is useful for radiation detection and localization in a wide scale. Before this prototype imager, there was not any report about a successfully built and evaluated wide area imaging system. It is also very meaningful to mention that, this prototype was also the first one to demonstrate the application of a Compton camera for aerial imaging in field.

For the next step, the detector volume of the Compton camera is planned to be enlarged to 8×8 channels for improving the sensitivity. The challenges for this wide area imager applied to imaging diffuse radiation in field would be also concluded in the next Chapter.

CHAPTER V

Wide Area and High Resolution Gamma-ray Imager with Large Volume

Encouraged by the results obtained from the prototype wide area imager through laboratory and field tests, the detector volume of the Compton camera, or the overall sensitive area of the detector, are enlarged by 4 times with the purpose to increase the detection efficiency and angular resolution. In this chapter, two approaches of building large volume imagers are introduced. We will meticulously describe the design, fabrication, evaluation, advantages, and shortcomings of these two paths for developing wide area and high resolution gamma-ray imagers.

5.1 8×8 System using SiPM

Considering the high gain and low temperature dependence of SiPM(KETEK, PM6660), a Compton camera with 64 SiPMs coupled to an 8 × 8 array of 10 mm × 10 mm × 5 mm GAGG crystals and another 64 SiPMs coupled to an 8 × 8 array of 10 mm × 10 mm × 10 mm GAGG crystals, was built and evaluated. In this section, the temperature compensation electronics, as well as point source imaging experimental results will be discussed.

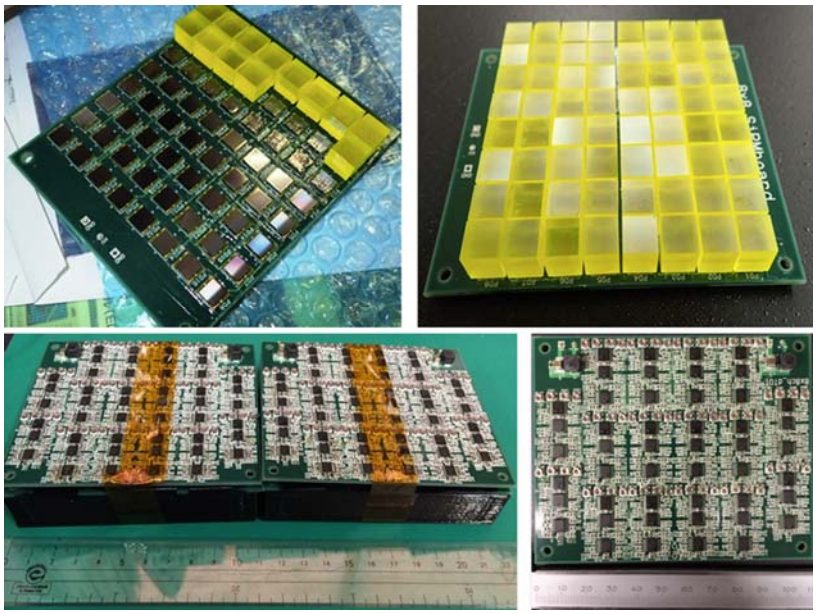

Figure 5.1: Photos of the SiPM arrays, GAGG arrays and electronic boards.

5.1.1 Overall Introduction of the System

A compact electronic circuit with single power supply(+3.3V), thus very low power consumption, was designed and fabricated to process the signals from SiPMs. The size of each electronic board, as shown in Figure 5.1 is about 10 cm × 10 cm. Each board with 64 channels of DToT circuit integrated, is of 396 mW in power consumption. In each channel, there is a CR-RC shaper followed by a comparator which compares pulse height with the amplitude of a dynamic threshold generated by a RC circuit.

Figure 5.2 shows the linearity between the amplitude of input waveform and time width of the digital signal of the compact circuits. A spectrum of ^{137}Cs source was also obtained (see Figure 5.3) with an energy resolution(FWHM) of ∼6% at the photopeak.

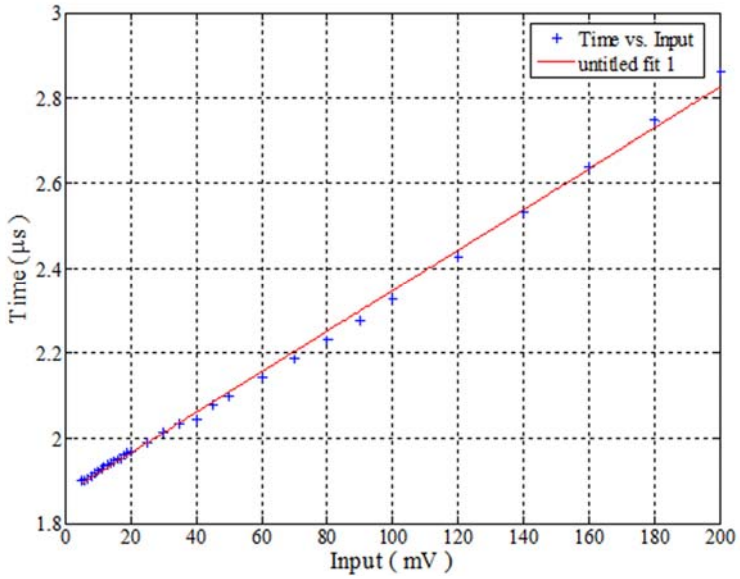

Figure 5.2: Linearity between the amplitude of input waveform and time width of the digital signal of the compact circuits.

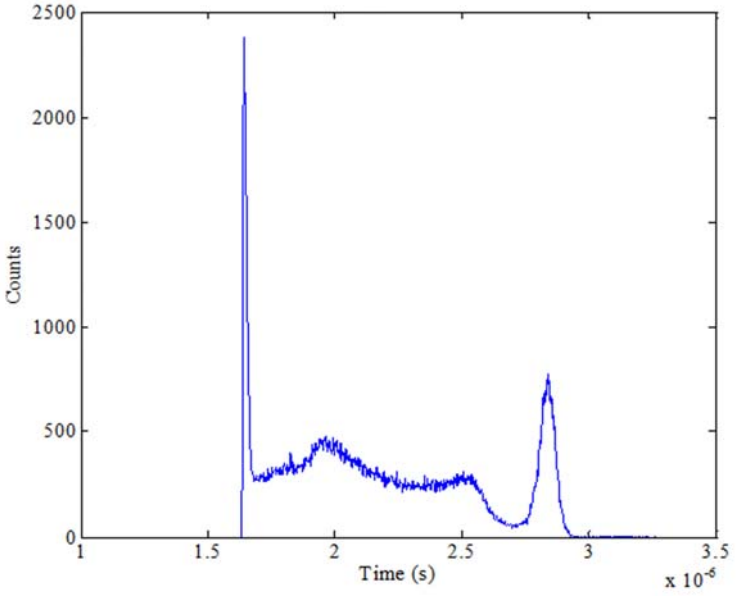

Figure 5.3: DToT Spectrum of ^{137}Cs.

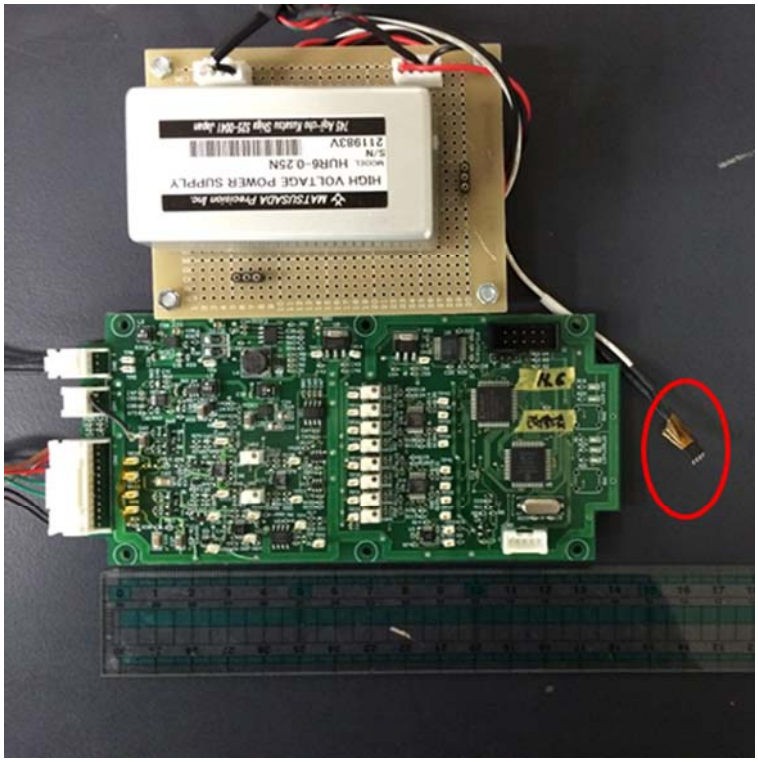

Figure 5.4: Temperature compensation circuit. The part in red circle is the temperature sensor.

5.1.2 Temperature Compensation Electronics

Although the temperature dependence of SiPM in room temperature is very small , it is relatively high when operated in high temperature environment, like in summer, as shown in Figure 4.2. In order to ensure the system the ability of working in high temperature situations properly, a temperature compensation circuit was designed and assessed for the gamma-ray imager. As the temperature goes down, the SiPM gets more sensitive to the incident visible photons, thus the output signals becomes higher. To compensate the effect coming from the temperature, one direct way is to change the power supply. For example, as the temperature goes down, the high voltage is also appropriately turned down to keep the overall gain of the SiPM at a stable level. Figure 5.4 is a photo of the devised circuit, in which the temperature sensor is shown in a red circle.

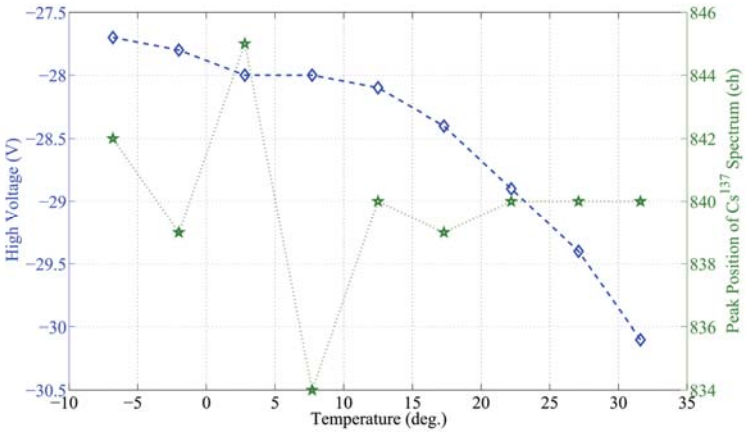

Figure 5.5: Performance of the temperature compensation circuit.

Temperature (°C)	Radioisotope	High Voltage (V)	Peak Positions(ch)
31.6	^{137}Cs	-30.1	840
27.1	^{137}Cs	-29.4	840
22.2	^{137}Cs	-28.9	840
17.3	^{137}Cs	-28.4	839
12.5	^{137}Cs	-28.1	840
7.7	^{137}Cs	-28	834
2.8	^{137}Cs	-28	845
-2	^{137}Cs	-27.8	839
-6.8	^{137}Cs	-27.7	842

Table 5.1: Performance of the temperature compensation circuit.

d Figure 5.5 shows the performance of the circuit. The x axis is temperature, the y axis in the left hand side is the corresponding high voltage for SiPM. With the temperature and corresponding high voltage, a set of spectra of ^{137}Cs were obtained using a multi channel analyzer. The y axis in the right hand side are the peak positions of the spectra. From the result we can see that, the temperature compensation circuit successfully compensate the gain change due to the temperature shift by changing the power supply and keep the overall gain of the SiPM at a relatively stable level. Table 5.1 is the exact value of the measured results used to plot Figure 5.5.

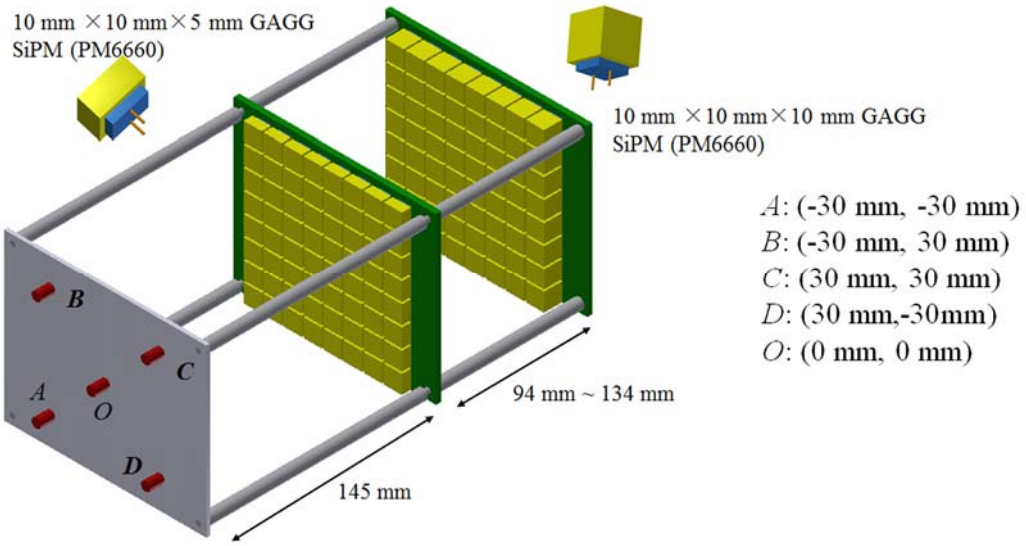

Figure 5.6: Setup of the 8×8 GAGG Compton camera using SiPM as photon detectors

5.1.3 Point Source Imaging

With 128 GAGG crystals coupled to 128 SiPMs, a Compton camera was built as shown in Figure 5.6. The points source imaging experiment was carried out based on this setup. Before the imaging experiment, spectra of ^{241}Am, ^{57}Co, ^{22}Na, and ^{137}Cs sources were collected for all the 128 channels. Photo peaks of those spectra were used to transform the DToT to the corresponding energy information. Figure 5.7 shows spectra of ^{137}Cs of all the 128 channels. From the spectra, we can see that all the channels were work correctly, and clear photo peaks as well as back scatter peaks were clear shown in the spectra.

After collecting the spectra for energy calibration, the same point ^{137}Cs source was placed at five different positions, A, B, C, D, and O, as shown in Figure 5.6 in order to calibrate the angular resolution and efficiency of the Compton camera. The distance from the source to the scatter was set to be 145 mm, the gap between the two detector arrays were 114 mm. Coincidence events were collected while the high voltage for he SiPM was -28.3V. The whole system was put into the temperature and

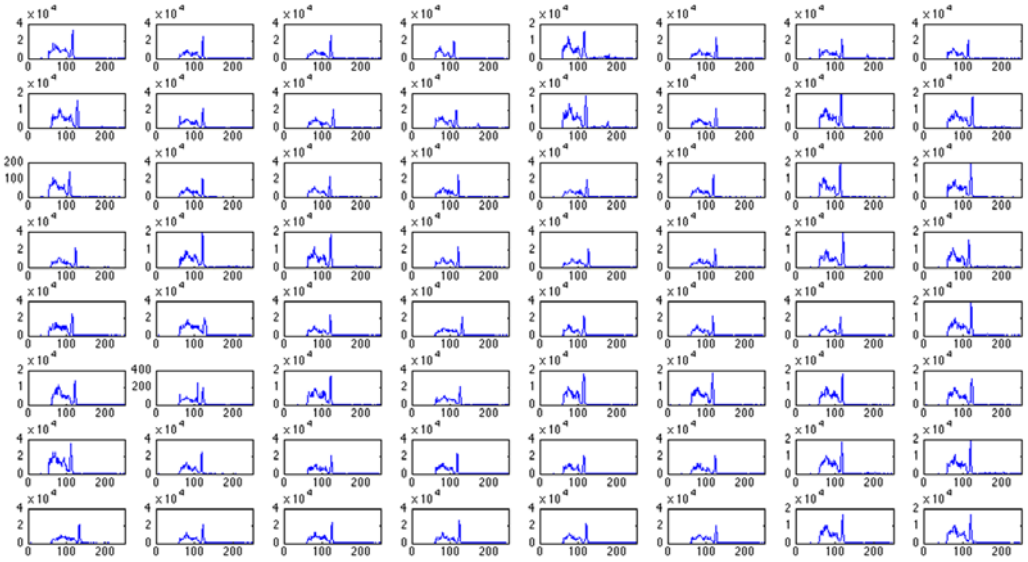

(a) Spectra of ^{137}Cs of all the 64 scatterer channels

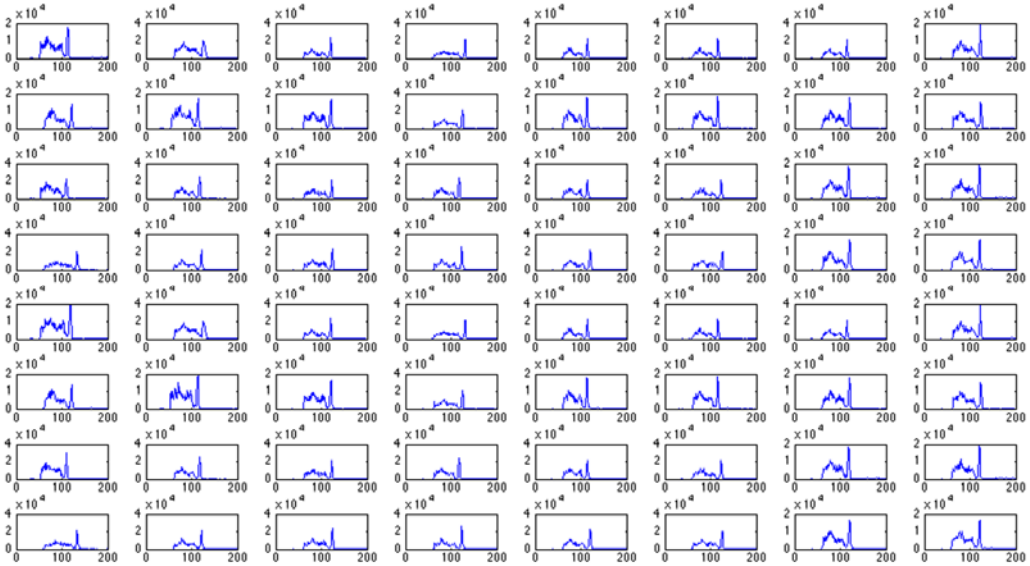

(b) Spectra of ^{137}Cs of all the 64 absorber channels

Figure 5.7: Spectra of ^{137}Cs of all the 128 channels.

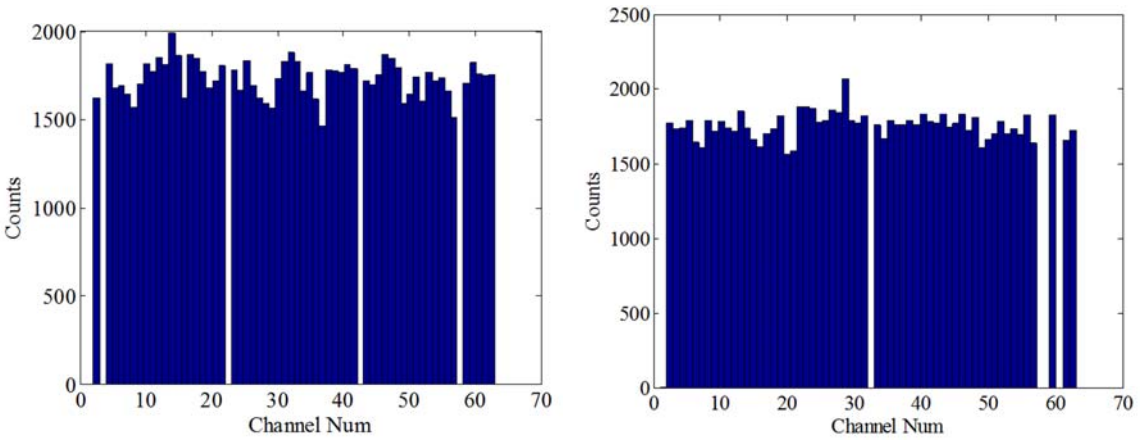

(a) Count rate performance of all the 64 scatterer channels

(b) Count rate performance of all the 64 absorber channels

Figure 5.8: Count rate performance of all the 128 channels.

humidity chamber(SH-242), whose temperature was set to be 15°C. The time window for the coincidence measurement was still 1.2μs.

Figure 5.8 shows the count rate performance of each channel. Although 128 spectra were obtained, there were still 4 channels in the scatterer and 5 channels in the absorber dead while conducting coincidence measurements. This is because some unknown problems of the verilog software running on the FPGA. The alive channels have a uniform performance in count rate. Point source images reconstructed using FBP were shown in Figure 5.9.

For Image 5.9(e), while the source was placed at location O, cross sections which pass through the high light point was drawn as shown in Figure 5.10. From the cross section, we can easily estimate the angular resolution was 9.4° FWHM in azimuthal direction and 9.0° FWHM in lateral direction. The intrinsic efficiency was also calculated to be 1.01pm0.02%. The angular resolution of images at different locations are provided in table 5.2. With this angular resolution, the detector system is expected to achieve a spatial resolution of 1.6 m FWHM in azimuthal direction and 1.6 FWHM m in lateral direction at the position under the detector while it is working in CCM at an altitude of 10 m.

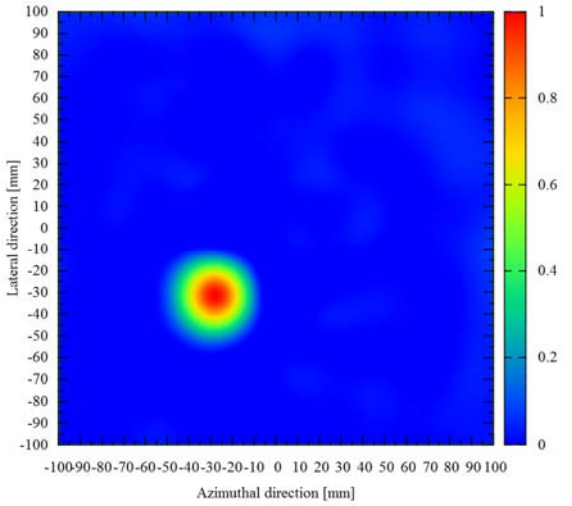

(a) Point source image while the source was put at position A

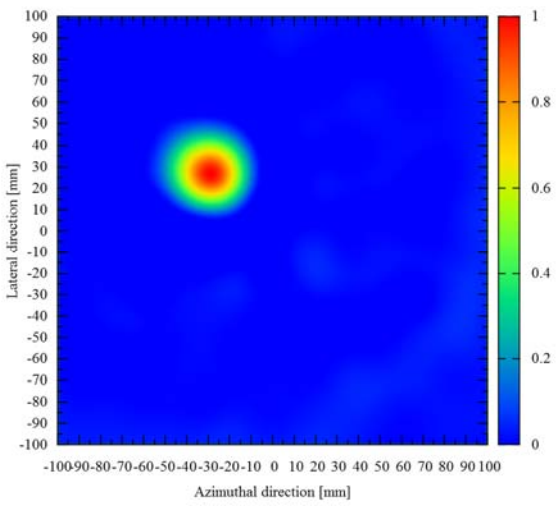

(b) Point source image while the source was put at position B

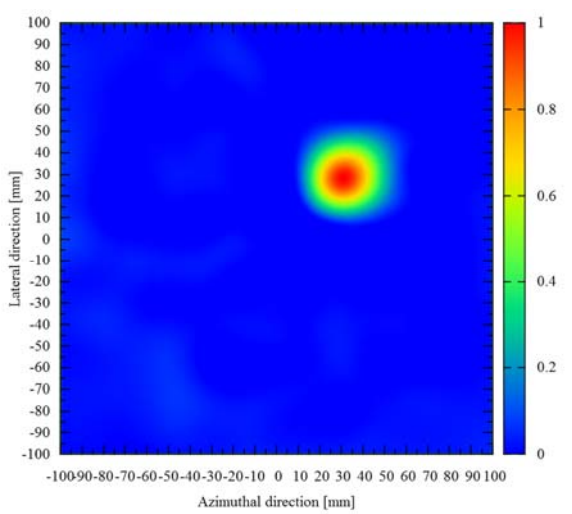

(c) Point source image while the source was put at position C

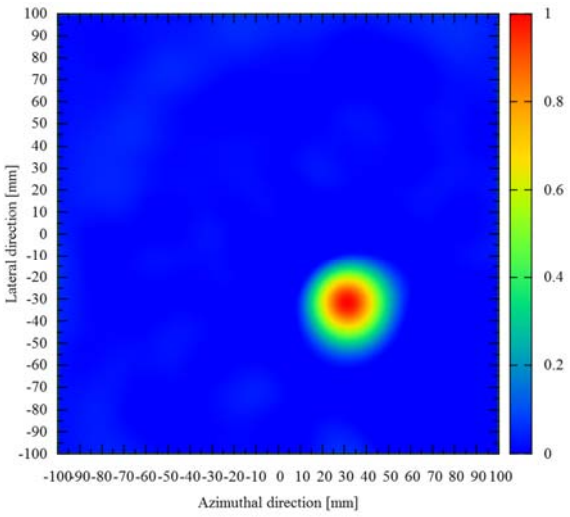

(d) Point source image while the source was put at position D

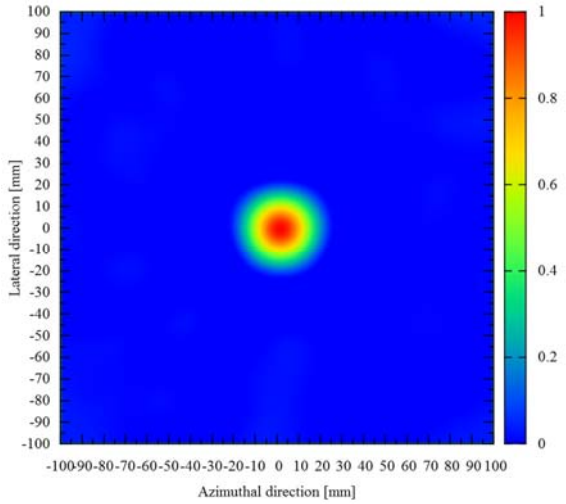

(e) Point source image while the source was put at position O

Figure 5.9: Point source images while the source was place at five different locations.

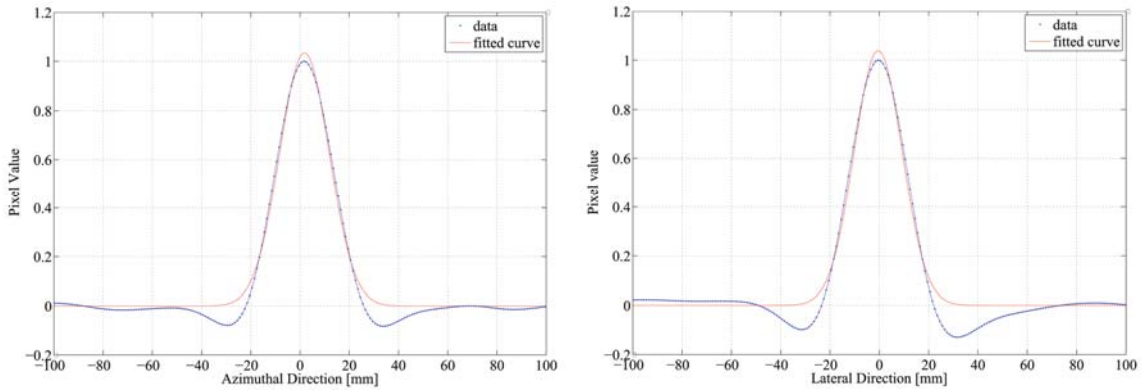

(a) Cross section in the azimuthal direction of image 5.9(e)

(b) Cross section in the lateral direction of image 5.9(e)

Figure 5.10: Cross section of the point source image 5.2

	Image at A	Image at B	Image at C	Image at D	Image at O
Source position (mm)	(-30, -30)	(-30, 30)	(30, 30)	(30, -30)	(0, 0)
FWHM in azimuthal direction (deg.)	9.3	10.0	10.0	9.9	9.4
FWHM in lateral direction (deg.)	9.4	9.3	9.5	10.0	9.0

Table 5.2: Angular resolution of images at different locations.

5.1.4 Dependence of Detector Performance on the Gap Distance

The imager performance, including the angular resolution and the intrinsic efficiency, is highly dependent on the gap distance between the two detector arrays. In this section, the relationships between the angular resolution as well as intrinsic efficiency and the gap distance were studied and reported. The same point ^{137}Cs source was place at position O in Figure 5.6. Coincidence was measurement while the distance between the scatterer and the absorber was increased from 94 mm to 134 mm. Distance from the source to the scatter array was still 145 mm. Operation conditions of the Compton camera were exact the same as above. Reconstructed images using FBP were shown in Figure 5.11.

The angular resolution and intrinsic efficiency were calculated as shown in table 5.3. The angular resolution was the best, 8.9° FWHM in azimuthal direction and 8.6° FWHM in lateral direction while the gap distance was 134 mm. On the contrary, when the distance was 94 mm, the intrinsic efficiency was the highest, 1.30±0.03%.

Using the data in table 5.3, the relationships between the angular resolution as well as intrinsic efficiency and the gap distance were drawn as shown in Figure 5.12 and Figure 5.13.

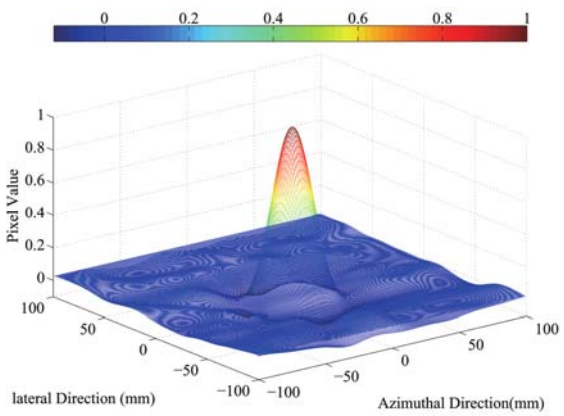

(a) Point source image while the gap distance was 94 mm

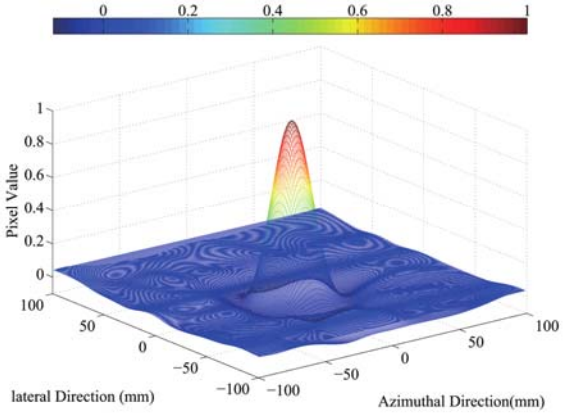

(b) Point source image while the gap distance was 104 mm

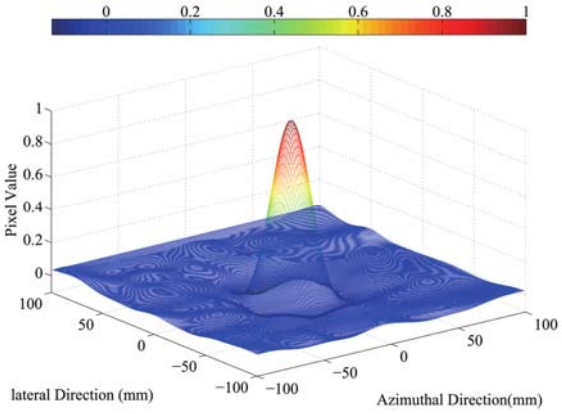

(c) Point source image while the gap distance was 114 mm

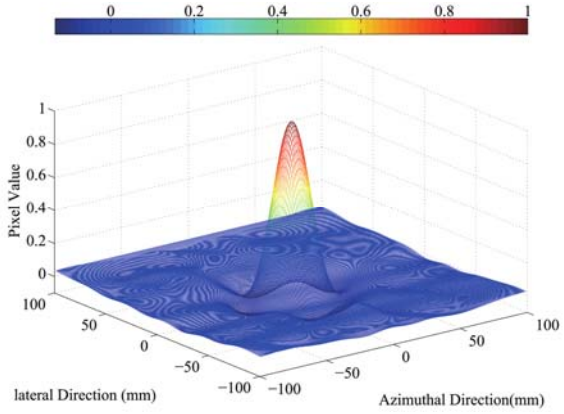

(d) Point source image while the gap distance was 124 mm

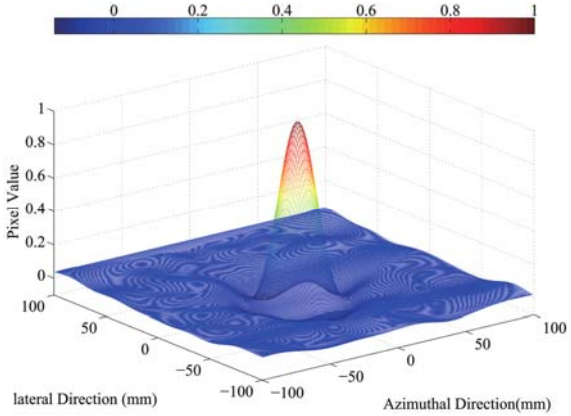

(e) Point source image while the gap distance was 134 mm

Figure 5.11: Point source images while the distance between the scatterer and the absorber was increased from 94 mm to 134 mm.

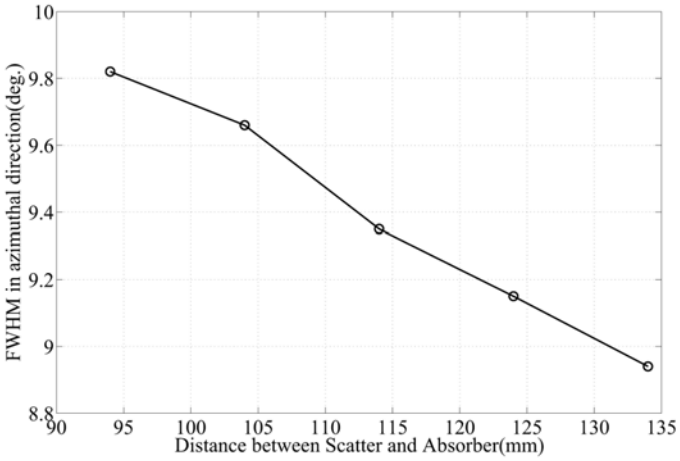

(a) Angular resolution in Azimuthal direction Vs. Gap distance

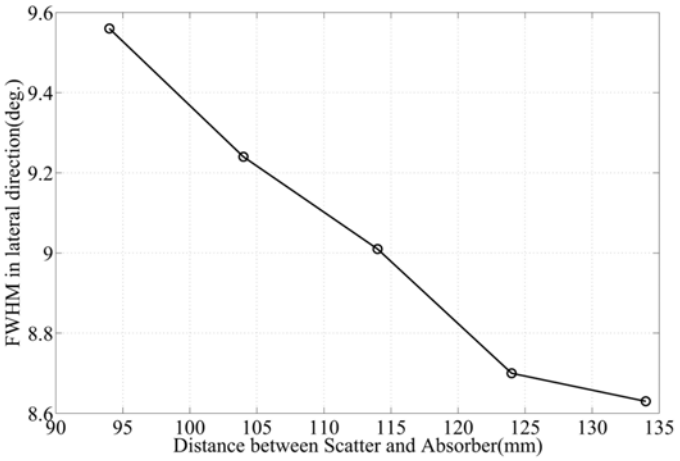

(b) Angular resolution in Lateral direction Vs. Gap distance

Figure 5.12: Angular resolution Vs. Gap distance.

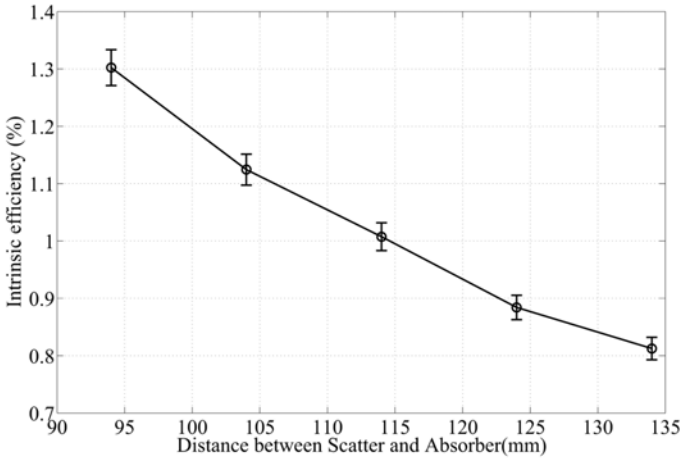

Figure 5.13: Intrinsic efficiency Vs. Gap distance.

	Image 5.11(a)	Image 5.11(b)	Image 5.11(c)	Image 5.11(d)	Image 5.11(e)
Source position (mm)	(0, 0)	(0, 0)	(0, 0)	(0, 0)	(0, 0)
Gap distance (mm)	94	104	114	124	134
FWHM in azimuthal direction (deg.)	9.8	9.7	9.4	9.2	8.9
FWHM in lateral direction (deg.)	9.6	9.2	9.0	8.7	8.6
Intrinsic efficiency (%)	1.30	1.12	1.01	0.88	0.81

Table 5.3: The dependence of the Compton camera performance on the gap distance.

From Firgure 5.12 and Figure 5.13, it is concluded that, as the gap distance increases, the intrinsic efficiency decreases due to the decrease of the solid angle subtend by the absorber to the scattered photons, and the angular resolution turns better because of the decline of the geometry contribution to the angular uncertainty.

With this Compton camera, when the gap distance is 94 mm and 134 mm, the detector system is expected to achieve a spatial resolution of 1.7 m FWHM and 1.6 m FWHM in azimuthal direction, 1.7 m FWHM and 1.5 m FWHM in lateral direction, respectively, at the position under the detector while it is working in CCM at an altitude of 10 m.

5.1.5 Effect of the Size of the Point Source on the Angular Resolution

When calibrating the angular resolution of a imager, a point source imging was always the best choice. However, it is impossible to apply a real point source in

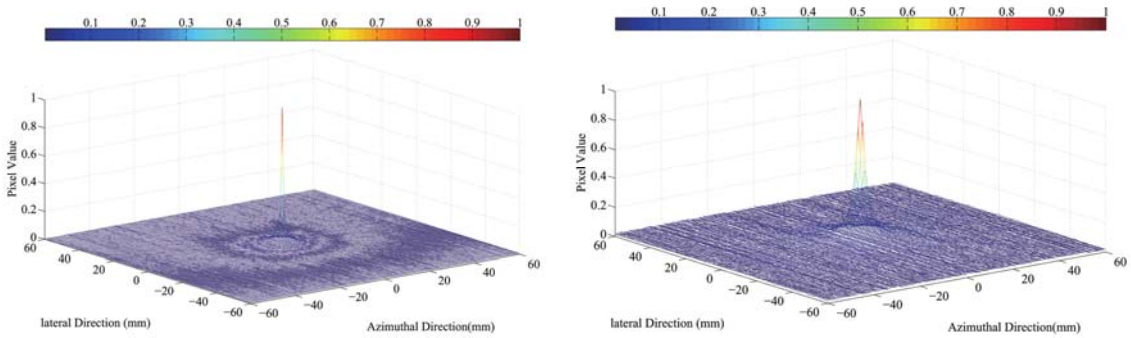

(a) Point source

(b) Cylinder source (2.5 mm in diameter × 8 mm in height)

Figure 5.14: Images using a point source and a cylinder source. Accurate information of energy depositions and interaction locations were used. We merely considered events with only one scattering in the scatter. Doppler broadening effect was ignored.

laboratory environment. No matter how small the point source is, it has some size. Analytical computation of the effect on the angular resolution contributed by the geometry of the point source was difficult. Here, Monte Carlo simulation by Geant4 was carried out to estimate the effect.

A Compton camera with two planar detector planes was built. Each plane consisted of 64 pixels of GAGG detector. Gap distacne between the two plane was 80 mm. A real point source and another cylinder source was imaged when they were place 100 mm in front of and on the axis of the detector using 662 keV gamma rays. The size of the cylinder source was 2.5 mm in diameter and 8 mm in height, that was also the size of the point ^{137}Cs source used for the experimental calibration in laboratory for the Compton camera. A SBP reconstruction algorithm was applied. In the reconstruction, accurate information of energy depositions and interaction locations were used. We merely considered events with only one scattering in the scatter. Doppler broadening effect was ignored. The reconstructed images are shown in Figure 5.14.

The angular resolution of both images are summarized in table 5.4. Bin size in

Angular Resolution	Point Source	Cylinder Source
FWHM in azimuthal direction (deg.)	0.5	1.9
FWHM in lateral direction (deg.)	0.6	1.9

Table 5.4: Angular uncertainties of images 5.14. Bin size in the image plane was 1 mm, which corresponded to 0.3°. The thickness of the back projected cone was 1°.

the image plane was 1 mm, which corresponded to 0.3°. The thickness of the back projected cone was 1°.

Angular resolutions of the image using a cylinder source were about 2° in both azimuthal and lateral directions. These were much worse compared with the results when a real point source was applied. Given the overall angular resolutions of the newly developed GAGG-SiPM Compton camera around 9°, the contribution from the size of the source can be ignored. However, when calibrating a Compton camera with good angular resolution performance, e.g. the Compton camera developed by JAXA which an angular resolution of 3.5° at 662 keV[35], the contribution from the source geometry should be seriously studied.

5.2 8×8 System using PD

PD is almost temperature independent because it has no gain. At this point, PD is a good candidate for applications in which the temperature is difficult to be controlled. For employing PD as the photo detectors in our work, a new ASIC with DToT technology integrated was designed and evaluated. In this section, the attempt of building a wide area imager using PD is briefly introduced.

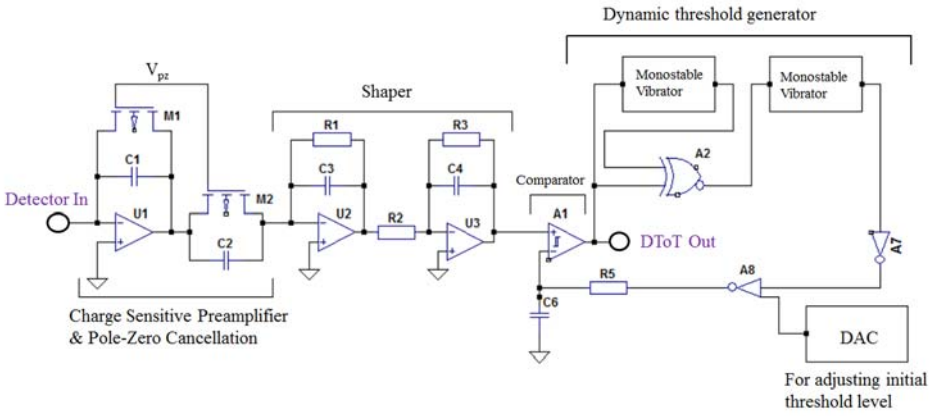

Figure 5.15: One channel schematic of the ASIC.

5.2.1 ASIC for PD

For the purpose of building a wide area gamma ray imager whose performance can not be affected by the temperature, a new ASIC which was integrated with 64 channels DToT technology has been designed and fabricated [147]. Figure 5.15 is the schematic of one channel of this new ASIC. In each channel, A charge sensitive preamplifier followed with a pole-zero cancellation circuit was applied. The signal was sent to a comparator after filtered by a CR-RC shapper. Two Monostable Vibrators combined with a RC circuit performed as the dynamic threshold generator. A DAC component was included to adjust the initial threshold level. The ASIC was fabricated using Taiwan Semiconductor Company complementary metal oxide semiconductor (TSMC CMOS) Process technology. The printed electronic board with the ASIC soldered is shown in Figure 5.16. The ASIC is of both 2.5 V power supply for analog and digital circuits. The total power consumption for one chip is about 300 mW.

5.2.2 ENC Level and ENC Slope Measurement

As discussed in Section4.1.1, an Equivalent Noise Charge(ENC) of 637 electrons in root mean square(rms) of the front-end electronics for PD(Hamamatsu, S3590-08) should be realized if a 5% of energy resolution is demanded at 662 keV, due to the low

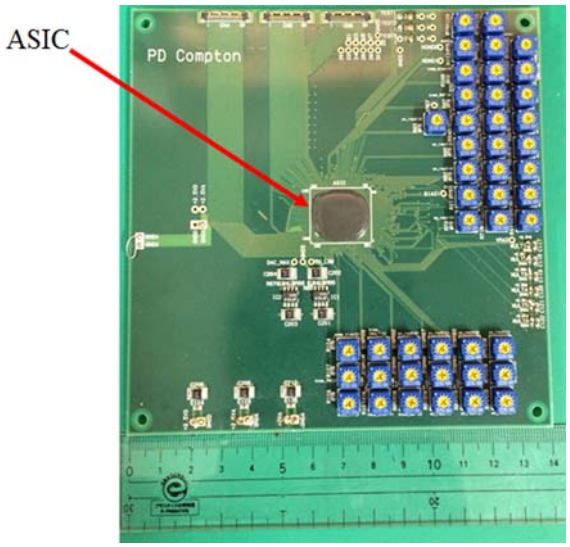

Figure 5.16: Printed electronic board with ASIC soldered.

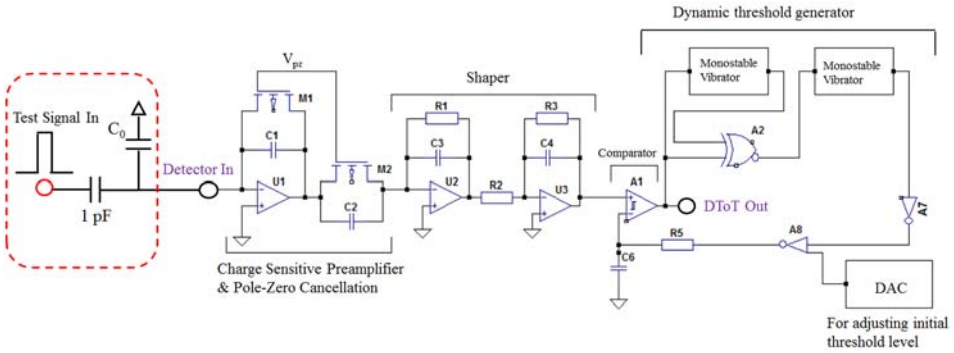

Figure 5.17: Evaluation circuit for test channel of the ASIC.

pulse height(∼4.8 fC). Therefore, ENC level is one of the kernel criteria for evaluation. Figure 5.17 shows the evaluation circuit for test channels of the ASIC.

Capacitor C_0 was removed when measuring ENC level. Spectra of shaper signals were obtained when the input charge was changing from 1 fC to 10 fC, in order to compute the ENC values. The measured result was plot as show in Figure 5.18. Figure 5.19 represents the linearity between the DToT time width and the input charge was also measured.

As shown in Figure 5.18, the ENC level was measured to be about ∼1200 electrons(rms). This was a little bit high if PD was coupled to GAGG and used as the

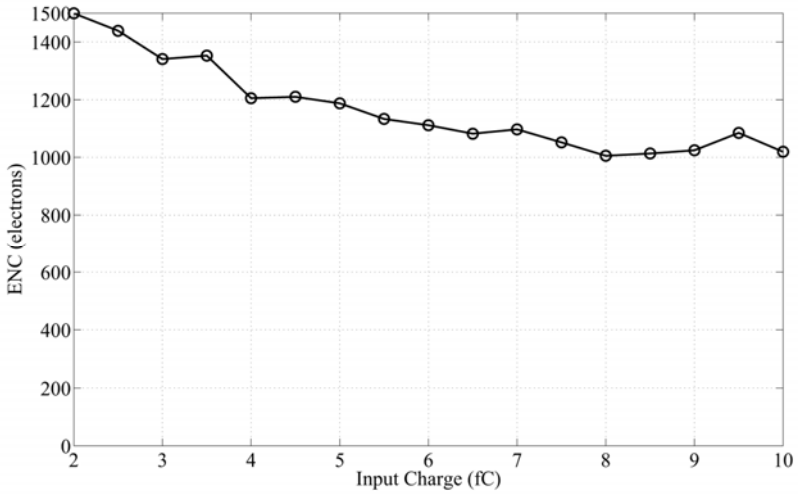

Figure 5.18: Measured ENC level(rms) of the test CH24 of the ASIC.

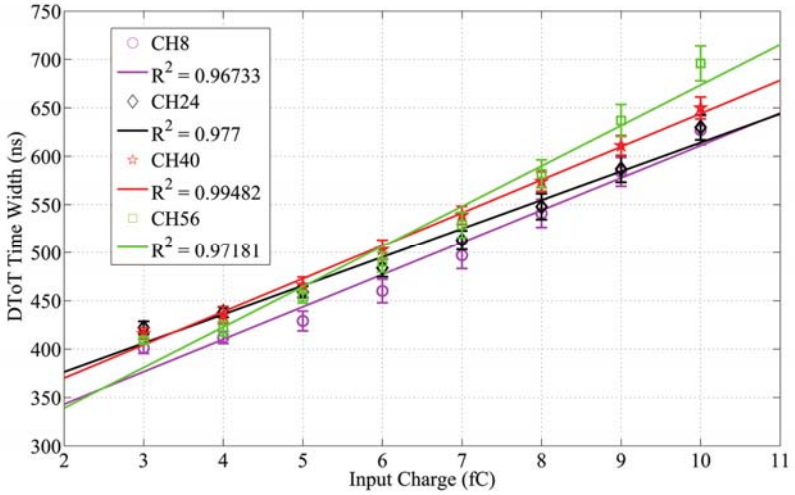

Figure 5.19: Linearity between the DToT time width and the input charge.

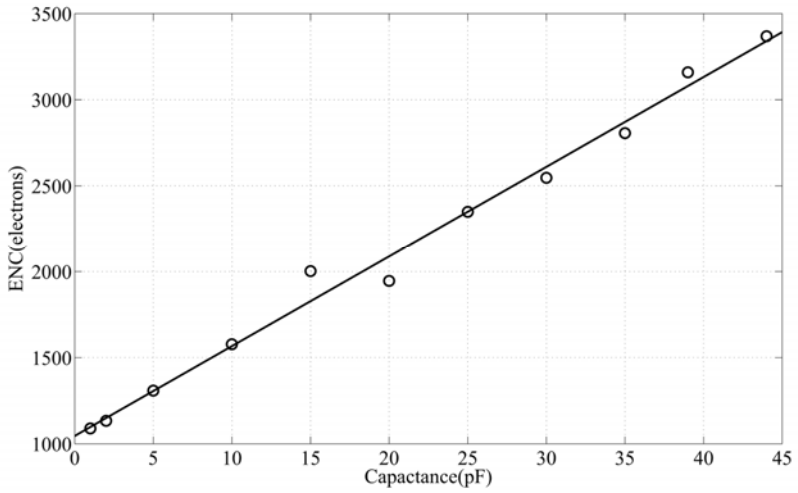

Figure 5.20: Measured ENC slope(rms) of the test CH24 of the ASIC.

photon detectors. What made the situation even worse was the high capacitance of typically PD. It was 40 pF for S3590-08 made by Hamamatsu. Thus, not only ENC at 0 input capacitance, but also ENC slope is significant for the front-end electronics when using PD. ENC values were measured and plotted when the input capacitance C_0 was changed from 1 pF to 44 pF. Figure 5.20 shows the result with a input charge of 5 fC. From the fit in Figure 5.20, a ENC slope of 52 electrons/pF(rms) was obtained. And it is also easily to compute that the ENC level with 40 pF input capacitance and 5 fC input charge is about ∼3200 electrons(rms). The corresponding energy resolution(FWHM) at 662 keV is estimated to be ∼25%, which is obviously far from enough to build a Compton camera with high angular resolution.

5.2.3 Summary

A new ASIC with 64ch DToT technology integrated was devised and evaluated in order to be applied as the front-end electronics for PD which is temperature independent. A very good linearity between the DToT time width and the input charge has been achieved. However, the ENC level obtained was a little bit high which cannot be used to process the signals from PDs. For semiconductors, e.g. Silicon strip

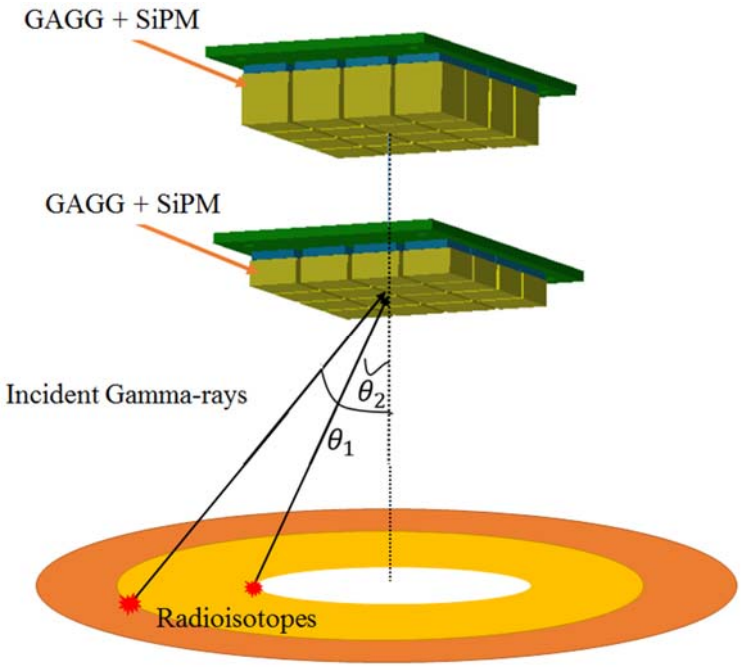

Figure 5.21: Typically geometry of a Compton camera.

detectors, or CdZnTe detectors, whose output pulse heights are much larger than those from PDs, this ASIC can be applied. Currently, we are designing another ASIC with a better ENC performance. In the coming future, PD will be employed to build a wide area gamma ray imager.

5.3 A new Reverse Geometry for Compton camera

5.3.1 Concept of the Reverse Geometry

In this work, the Compton camera of the wide area imager is consisted of two detector planes and placed parallel to each other with a gap distance. As shown in Figure 5.23(a), this typical geometry actually draws an amount of rings randomly on the image plane where radioisotopes locate.

Those rings are not highly concentrates on one certain point, or small part when measuring diffuse distributed radiation. Inspired the originality of the concept of GCM, especially GCM with ESM applied, whose detection targets are much more

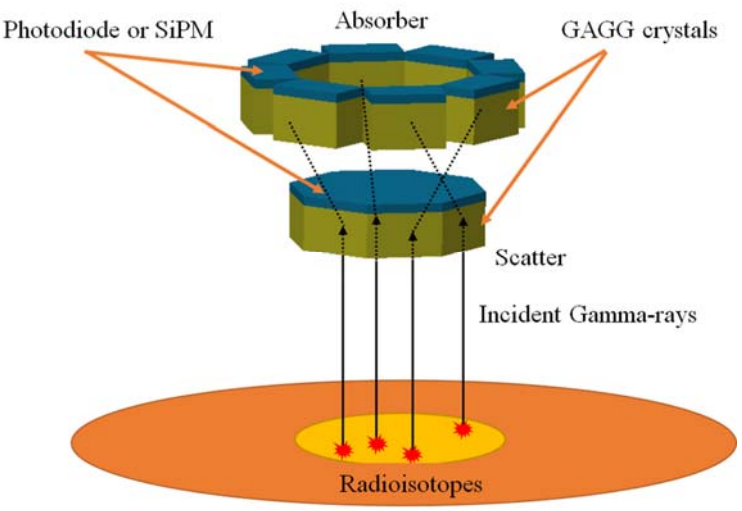

Figure 5.22: A new reverse geometry for Compton camera.

concentrate than SDM, we think whether it is possible to build a Compton telescope that can highly concentrate on some certain direction so as to improve its detection efficiency at this direction and subsequently improve the spatial resolution. Thus, a new reverse geometry for Compton camera came to our mind as shown in Figure 5.23(b).

In this design, with the reverse geometry, scattered gamma rays absorbed by the second ring shape detector planes, could be estimated coming from just the bottom of the telescope. In this manner, we hope the detection efficiency for the source located just under the camera system could be improved, however it might decrease the efficiency of detecting sources located in other areas. Experimental results show that, not only the efficiency, but also the angular resolution for detecting the sources just under the detector are highly improved by employing this new concept of geometry. It would benefit enormously for the fabrication of next generation of wide area and high resolution gamma-ray imager.

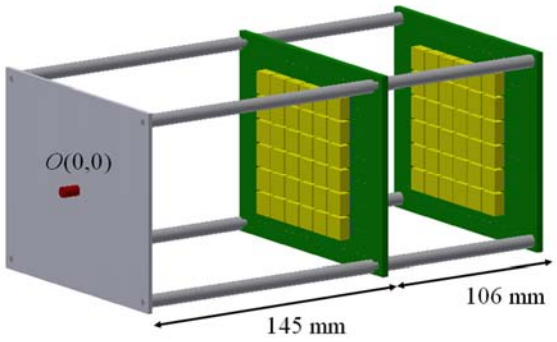

(a) Compton camera with normal geometry

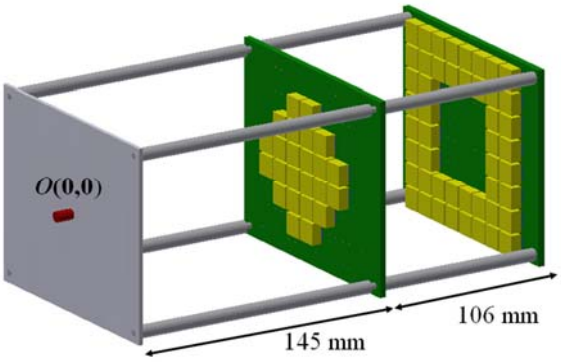

(b) Compton camera with reverse geometry

Figure 5.23: The setups of both cameras.

5.3.2 Experimental Results of the Reverse Geometry

To demonstrate the idea of this reverse geometry, two Compton cameras of which one is with normal geometry and the other rever geometry, have been built and their efficiency as well as angular resolution were evaluated. The setups of both cameras are shown in Figure 5.23.

Both of these two telescopes are consisted of 72 pixels, of which each is formed by coupling one SiPM(KETEK, PM6660) to a 10 mm $\times$ 10 mm $\times$ 5 mm GAGG crystal. Specifically, the Compton camera in normal geometry contains two 6 $\times$ 6 arrays, which are placed parallel to each other with 106 mm in gap distance, while the Compton camera in reverse geometry includes 24 pixels for the scatterer and 48 pixels for absorber. A point source was placed 145 mm away from the center of the

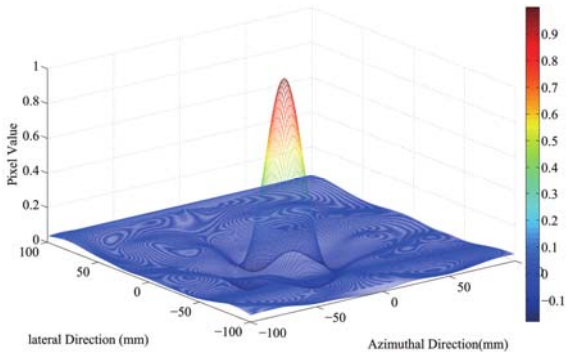

(a) Point source image for normal geometry

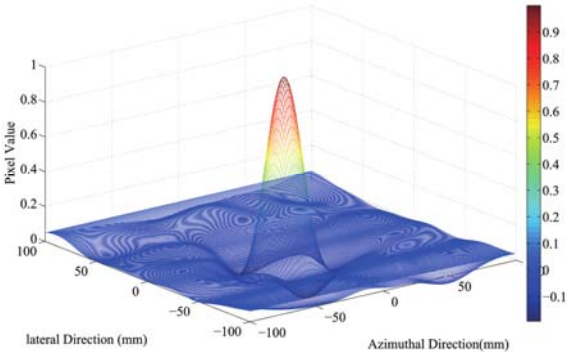

(b) Point source image for reverse geometry

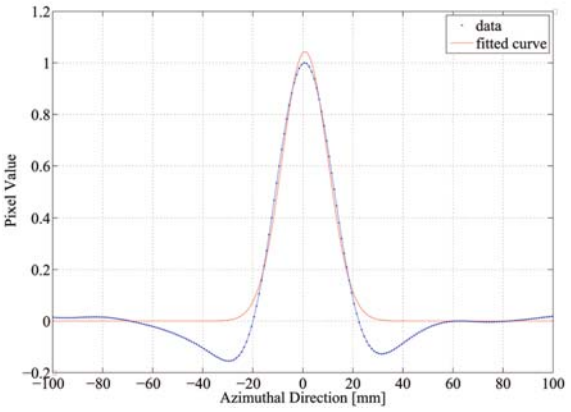

(c) Cross section in azimuthal direction for Image5.24(a)

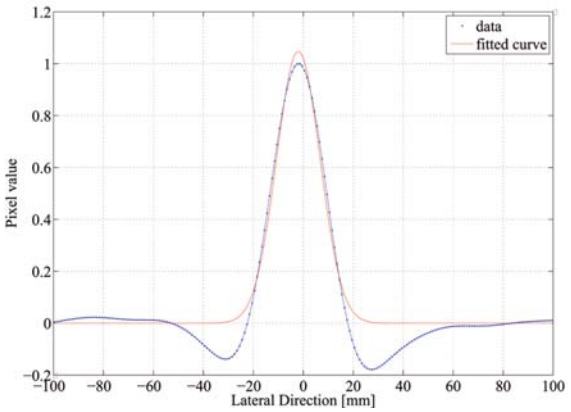

(d) Cross section in lateral direction for Image5.24(a)

both scatterers, successively, to perform efficiency and angular resolution calibration experiments.

The measured intrinsic efficiencies of both system were 0.55% and 0.66% respectively. The efficiency in reverse geometry was improved by 20% compared with that in normal geometry. Point source images were reconstructed using FBP. The images and their cross sections in both azimuthal and lateral directions are shown in Figure 5.24.

The results of the angular resolutions, as well as efficiency were summarized in table 5.5. From the results we can conclude that, angular resolutions in both azimuthal and lateral directions were both improved by applying this new concept of reverse geometry for Compton camera, though the improvement were not so ob-

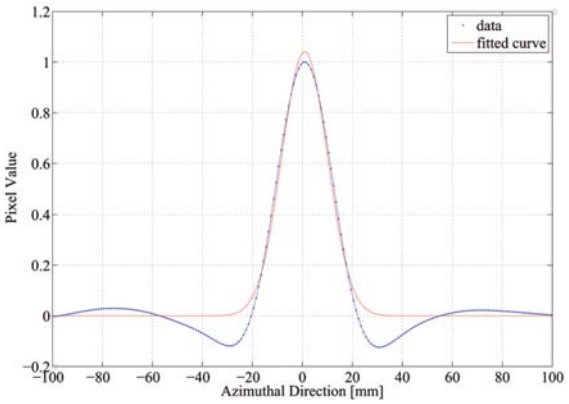

(e) Cross section in azimuthal direction for Image5.24(b)

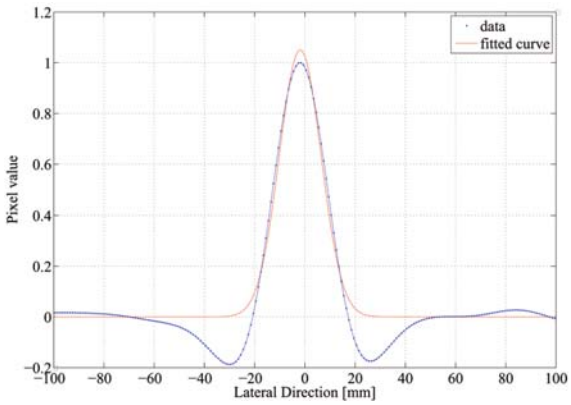

(f) Cross section in lateral direction for Image5.24(b)

Figure 5.24: Point source images their cross sections in both azimuthal and lateral directions for both geometries.

viously. Additionally, the reverse geometry for the experiment was not optimized yet. Simulation works is demanded to determine various parameters for this concept. These parameters includes the shape of both detector planes and the gap distance between them.

5.3.3 Summary

A new concept of reverse geometry for Compton camera to improve the detection efficiency as well as angular resolution for detecting radioactive sources just under the detector was proposed in this section. Two Compton cameras were built with a same number of pixels to demonstrate the concept. Comparison of experimental results shows that efficiency was improved by 20% in reverse geometry compared with that in normal geometry. Meanwhile, angular resolutions in both azimuthal and lateral directions were also improved.

Additionally, the reverse geometry for the evaluation experiments was very coarse and not optimized yet. Simulation works is demanded to determine various parameters for this concept so as to obtain a maximized geometry. These parameters include but not limit to the shape of both detector planes and the gap distance between them.

	Reverse geometry	Normal geometry
FWHM in azimuthal direction (deg.)	8.4	8.6
FWHM in lateral direction (deg.)	7.7	7.9
Intrinsic efficiency (%)	0.66	0.55

Table 5.5: Experimental results for Compton cameras in both normal and reverse geometries.

5.4 Field Experiment and Results

Field experiment using the 8 × 8 SiPM system was conducted on Feb, 23rd, at the same place as discussed in Chaper III, with the ground measured distribution shown in Figure 3.20 and 3.21. The field experiment this time was focus on the Compton imaging using the newly developed large volume wide area gamma ray imager. The purpose of this field experiment was to calibrate, evaluated this newly developed system to image diffuse distribution in situations of complicated terrain and temperature. The speed of the wind were about 7∼10 m/s, roughly obtained from my iphone 5S.

5.4.1 Instrument Preparation and Deployment

Based on the point source imaging performance in laboratory environment of the Compton camera, we decided to set the gap distance to be 94 mm, in order to achieve good efficiency as well as reasonable angular resolution. The basis line of the dynamic threshold was set to be 17.5 mV which equals to 70 keV due to the consideration that the temperature outside at that time in Fukushima was around 5 ∼ 10 ℃. The gps

Location	Height (m)	Hovering time(min:sec)	Count Rate Range (cps)
Hot region 1	5	15:00	250∼390
Hot region 1	10	15:00	180∼350
Hot region 1 with 3.6 m shift to the west	10	15:30	180∼450
Hot region 1	20	20:00	120∼260
Hot region 1 with 7.3 m shift to the west	20	20:00	100∼220

Table 5.6: The aerial hover measurements taken during the wide area imager field testing campaign in Fukushima.

module was set to renew the position information of the imager while the total events increased every 512 counts. The mass of the whole system was around 5 kg.

The field testing consisted of 5 aerial deployments as summarized in table 5.6. Hot region 1 refers to the hot areas pointed out in Figure 3.21. The five deployments were fulfilled in two flights, of which, the first one carried out the first three measurements, the last flight conducted the last two tests. Figure 5.25 shows the newly developed Compton camera being mounted underneath the unmanned helicopter and prepared to take-off. To reliably obtain a signal, the GPS antennae was equipped on the top of the AUH tail using green tapes during flight. The wifi module can be also seen being mounted on the white enclosure. Figure 5.26 shows the wide area imager in flight. The ground communicable devices were used to collect the data which was sent from the flying system to check the working status of the imager.

Figure 5.25: The newly developed wide area imager in the white enclosure mounted on the unmanned helicopter prior to take-off for the first flight measurement.

Figure 5.26: The wide area imaging in flight. The communicable devices on ground is also shown in this figure.

Figure 5.27: Temperature recorder, TR-71ui.

5.4.2 Temperature Recording

The temperature compensation circuit was firstly used in this field test. The gain of the SiPM can be controlled stable in a wide temperature range due to the automatical power supply adjustment according to the measured temperature in real time. As a supplement, a temperature recoder was also used to record the temperature during the flights. Figure 5.27 is a photo of the temperature recorder, TR-71*ui* [148]. The recorded temperature for the two flights are shown in Figure 5.28. The wide area imager was working approximately in a 18∼26 ℃ temperature range, in which, the temperature compensation circuit can properly work.

5.4.3 Field Performance

DToT technology was applied to the front-end circuit board for this system. It only consists of a CR-RC shaper, a comparator and a monostable vibrator for each channel. This method is of very simple components thus leading to a very low power consumption and capability of being applied to multi-channel systems. The dynamic

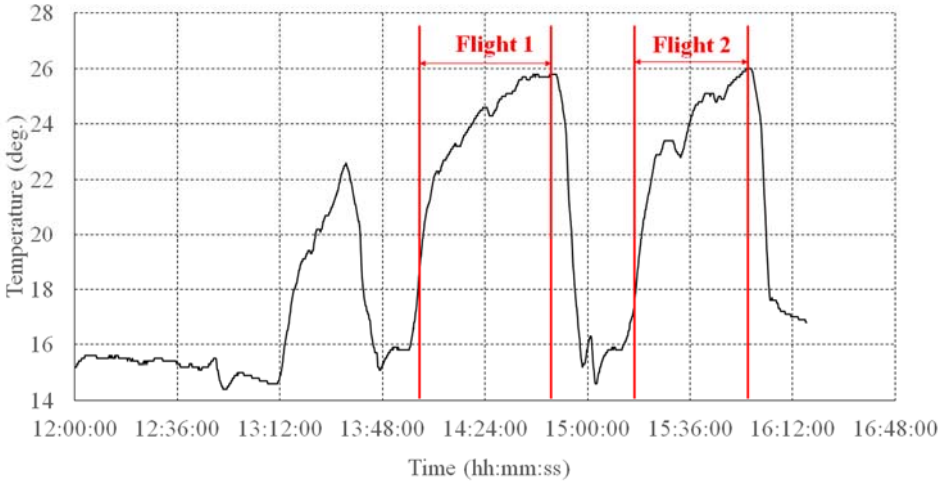

Figure 5.28: Recorded temperature during flights.

threshold is typically generated using a RC circuit plus a DC initial value. This DC base line should be higher than the noise level in order to filter them. If the basis value is not high enough, then many of the output digital signals are trigger by the noise thus resulting in an unpredictable high count rate. If this happens in some certain channel of a multichannel system, then this channel will keep sending signals to the FPGA which performs digital data processing. As a result, signals from other channels can not be read due to the stack of signals from the abnormal channel. This might be happen when the gain of the SiPM can not be controlled in field environment, although the threshold for this field test was set to be two times high of that for laboratory calibration experiments.

The first goal of the measurement in field this time was to calibrate the performance of each channel of the wide area imager. To this end, the GAGG plus SiPM detectors as well as DToT front end electronics performed very well. For example, the count rate performance of each channel for the first flight are very similar with each other as shown in Figure 5.29.

Shown in the left of Figure 5.29 is the total count of each channel in the scatterer of the first flight, in the right is that in the absorber. Only signals of 6 channels in

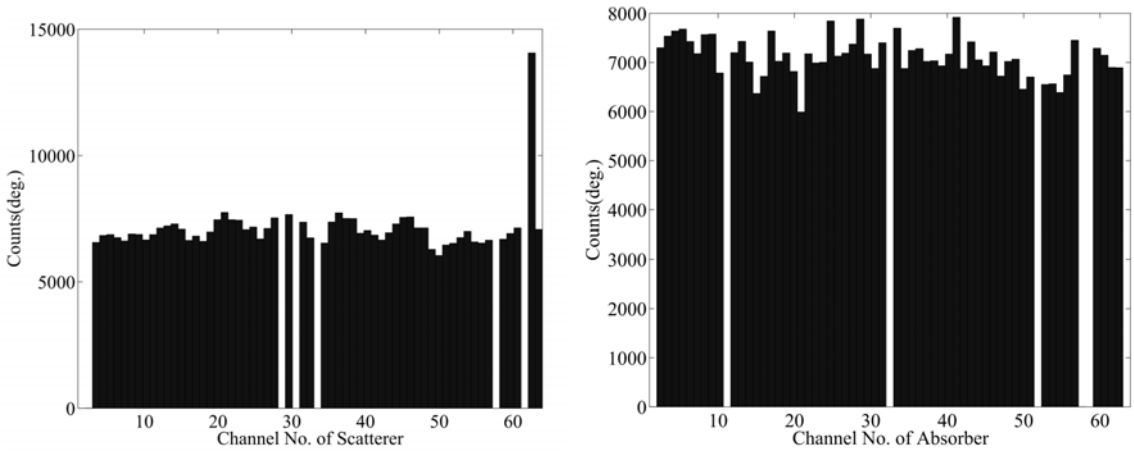

(a) Count performance of each channel in scatterer

(b) Count performance of each channel in absorber

Figure 5.29: Count performance of each channel of the wide area imager.

the scatterer and 5 channels in the absorber can not be read due to some unknown problem of the DAQ software. The wide area imager performed almost the same in field as operated in the laboratory.

5.4.4 Preliminary Compton Image Reconstruction

In table 5.6, the 5 aerial deployments which were conducted in two flights, were summarized. The routes of the two flights according to the GPS information were drawn in Figure 5.30 and Figure 5.31.

From the flight routes, the AUH vibrations can be easily observed. In the first flight, as shown in route 5.30, the vibrations in latitude, longitude and altitude directions were all sub-500 mm, while in the second flight, as shown in route 5.31, the vibrations in altitude direction were around 2∼3 m. This is mainly because the strong wind during the flights. The altitude in the figure the the distance from the AUH to the sea level.

The strong AUH vibrations, mainly caused by the wind, arose challenges to achieve accurate images. In order to alleviate the influence from the vibrations,

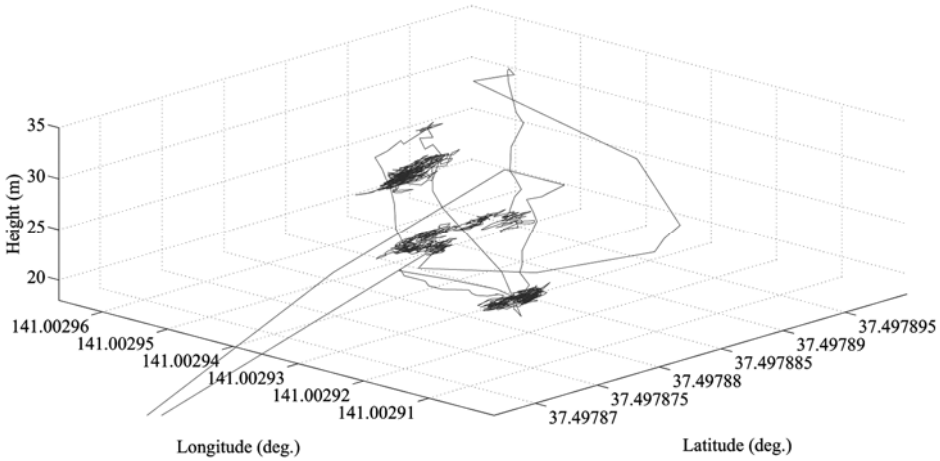

(a) 3D route of the first flight

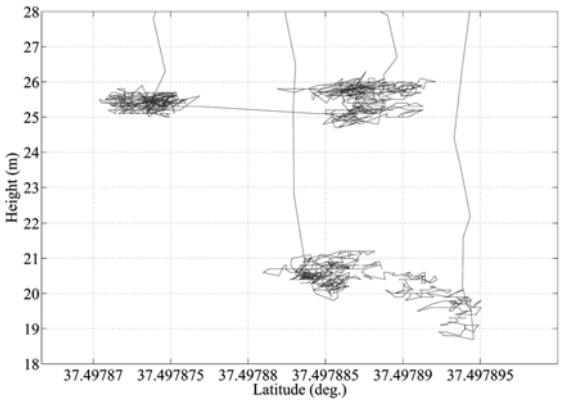

(b) Latitude

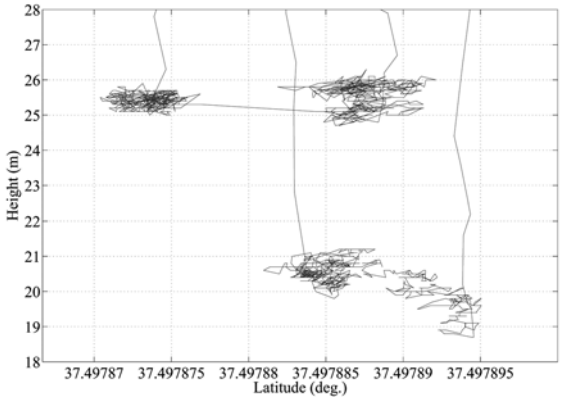

(c) Longitude

Figure 5.30: Route of the first flight. Show in the bottom-left was the route in latitude direction, in the bottom-right the route in longitude direction.

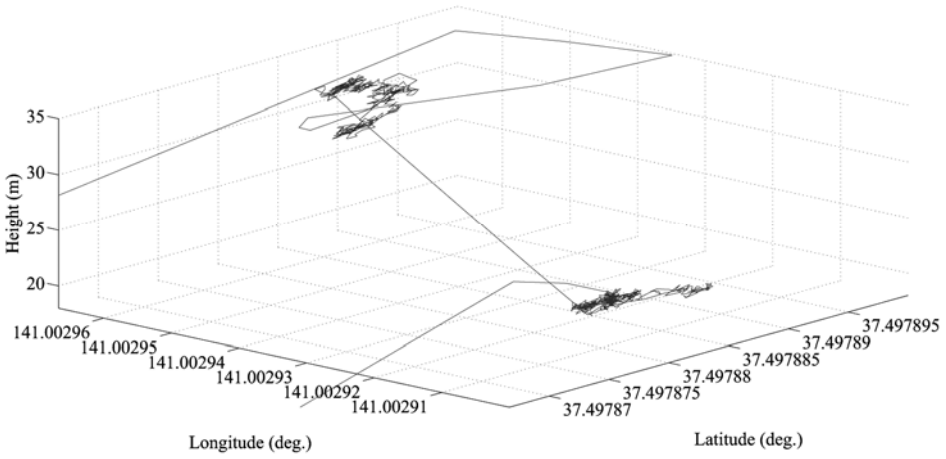

(a) 3D route of the second flight

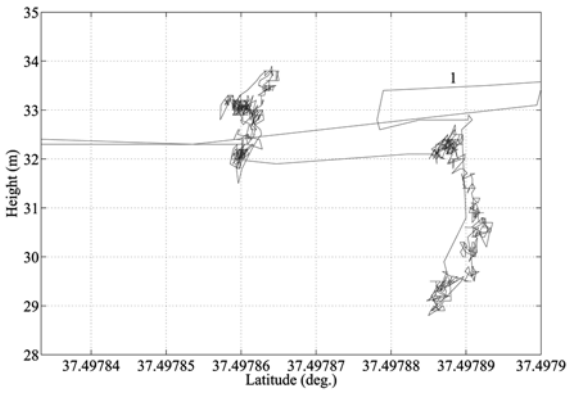

(b) Latitude

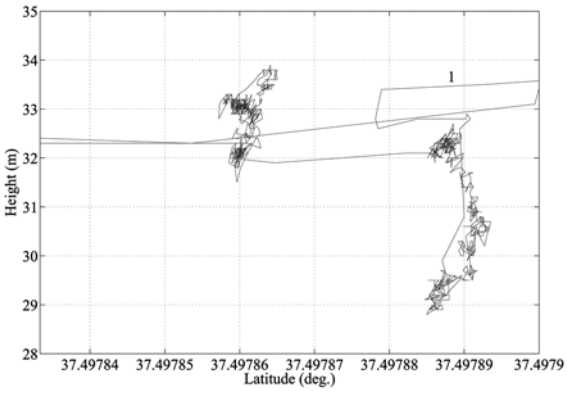

(c) Longitude

Figure 5.31: Route of the second flight. Show in the bottom-left was the route in latitude direction, in the bottom-right the route in longitude direction.

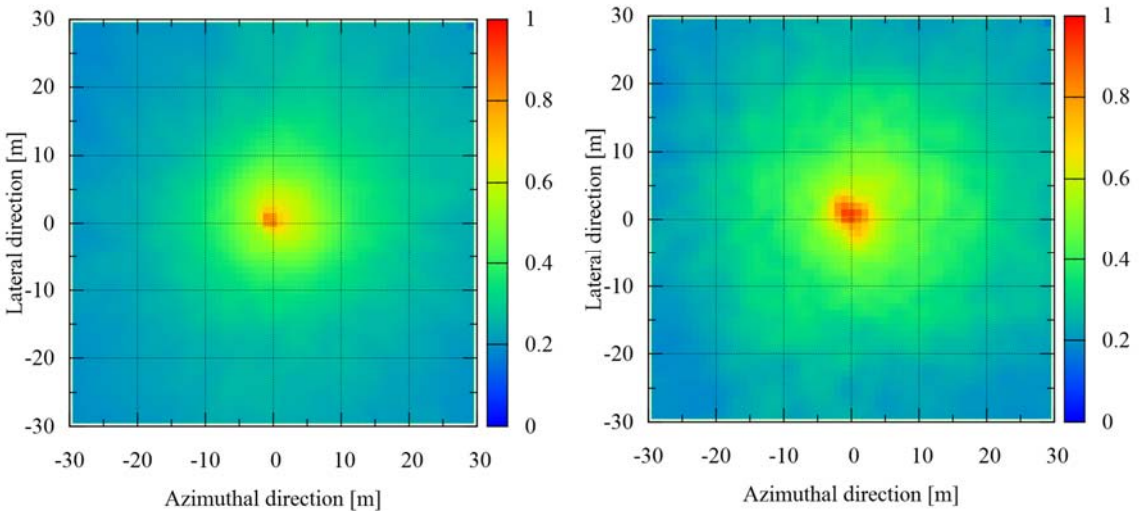

(a) Image at 5 m height.

(b) Image at 10 m height.

Figure 5.32: Images at 5 m and 10 m height on the top of hot region 1.

events collected when the AUH locations were in a certain zone were selected from reconstruction. The zones should be small enough to decline the effect as much as possible, but not too small to filter too much events. By trying different sizes of the zones for the reconstruction, a size of 20 mm × 20 mm × 20 mm in each dimension was decided. Meanwhile only those event with E_s+E_a larger than0.88×662 keV and smaller than 1.12×662 keV were used in imaging.

In addition to the regular geometric cuts and energy cut applied to the reconstruction, several other event cuts were attempted in analyzing the field. These includes subtraction of an off-peak reconstructed image to eliminate background and energy depositions in the scatter larger than 450 keV. With all these methods applied, images of the first and second deployment were obtained and shown in Figure 5.32. The preliminary Compton imaging results are promising as the hot areas under the imager can be rightly discovered. When the hovering height increases, the wide area imager tends to work in a wider field of view with the comprise of spatial resolution. This was also demonstrated in simulation works and field tests with prototype system. Measurements in other deployments failed to produce clear and accurate images,

mainly due to the vibrations. Although, promising images in this calibration test in Fukushima were obtained, there are still serval challenges that should be addressed prior to the wide application of the developed wide area imager.

5.4.5 Challenges of Imaging in the Field

The characterization of Compton camera(which was fixed in a SH-242 temperature and humidity chamber) in the laboratory focused on imaging of far field point sources within a low intensity background environment. For field tests using the wide area imager, the combination of a Compton camera and an unmanned helicopter, there exists several obvious differences that make imaging much more challenging.

Predominately, the vibration of the helicopter during flight was perhaps the biggest challenge for creating accurate images. This vibration contributed to the uncertainties of interaction positions and finally deteriorate the angular resolution of the images. The uncertainties of the interaction positions caused by this vibration can be as high as meters. Compton camera with those high uncertainties in interaction locations almost lose its ability of position localization of radioactive materials. The vibration can be smaller in very good temperature, however, very serious in windy days.

The diffuse distribution of both the radionuclides and the background was also a primary challenge to successful imaging. In laboratory environment, back projected Compton cones overlap in one specific location corresponding to the origin of the point source. Although, simulation works has demonstrate that the GAGG based Compton camera was capable of imaging distributed sources that emit single energy photons. However, in the case of field measurements, the distribution of the radioactive materials are much more complicated. Unlike the spaced dot point sources used in the simulation, the real radionuclides spread continuously in field. Additionally, the emitted photons are of various energies, e.g., 569 keV, 605 keV, 796 keV, 1039

keV, 1168 keV and 1365 keV from ^{134}Cs.

The complicated terrain of the field in real tests is another challenge to yield accurate images. In this work, we use 2D reconstruction methods. Given the height of the imager was known, reconstructed Compton cones were projected to the ground level. For point source imaging in laboratory, the image plane was flat, the distance between the image plane to the scatter was fixed. However, the ground in field can not be always so ideal, especially at places where rivers, mountains locate, 2D reconstruction is apparently not enough. 3D reconstruction [149, 150]could be a possible solution for this challenge. However, much larger number of events are required which demands longer measurement time. Typically, 3D reconstruction methods required longer computation time, resulting in the difficulty of real time imaging [151–154].

Another important issue that has long been ignored was the radioactivity in the vegetation. The activity as measured by personal dosimetry was observed 1$\sim$3 μSv/hr as shown in Figure 5.33. High intensity as over 10 μSv/hr has also been observed in tall trees and bushes in places close to the river and hot regions. Photons emitted from those vegetation were also able to reach the detector, especially from the tall trees that were much closer to the detector. In this case, 2D reconstruction was far from enough to generate accurate images.

Issues such as noises caused by the temperature compensation circuit, by the vibration of the helicopter, the complete ground truth measurements including the intensity of the vegetation, the accurate truth of the detector temperature, should be studied and addressed prior to the next run. In addition, appropriate reconstruction algorithms should be developed to better adapt to the specific detection scenarios of the wide area imager for test in wide scale.

Figure 5.33: Measurement using personal dosimetry. Note, the measured vegetation were very close to the road. Higher dose has been observed in places close to the hot areas.

5.4.6 Recommendations for the Future Tests

For future measurements using wide area imager, several recommendations can be made based upon the calibration flights.

(1) A windless day would be preferred to carry out the flights in order to decrease the vibration of the helicopter. If possible, unmanned helicopters with better and stable performance would be better choices to be applied as the carrier of the Compton camera.

(2) Compact temperature chamber would be a great help to keep the working temperature of detectors stable. In this case, the gain of the detectors keep at a stable value. Thus, the energy information obtained would be much more accurate. Another advantage for employing a temperature chamber is that the initial threshold could be set to be lower without any worry that the noise level would surpass it. As a result, the imager can obtained events with much lower energy losses in the detectors. And as discussed in Chapter II, those events with small

scattering angles can help to achieve better angular resolution. Meanwhile, the efficiency can be also improved.

(3) Better detector energy resolution would increase the angular resolution of the imager. For germanium, there is a tradeoff between energy resolution and simplicity of operation. Meanwhile, the price of germanium is also very high. A silicon tracker in front of an absorber plane would be a good choice for achieving better spatial resolution, because silicon devices have good energy resolution and do not require cooling. However, sensitivity of silicon materials to gamma-rays are very low, especially at energy as high as 662 keV. Recently, a newly Sr_2I scintillator, which can achieve an energy resolution of better than 3% at 662 keV with APD and light yield of 80000 photons/MeV, is being evaluating in our lab. This crystal could be a very good candidate for achieving high angular resolution without loss in efficiency.

(4) Reverse geometry for Compton camera is capable of improving the efficiency and angular resolution of recognizing radionuclides on the axis of the detector in far field. An optimized reverse design would benefit the system to achieve accurate images with shorter measurement time. Or, it can help the system to collect more events in order to apply 3D reconstruction.

(5) For far field imaging measurements, until now, there are not any specific reconstruction algorithms developed. Thus, attention on the software development is highly meaningful and would directly contribute to the quality of the images.

(6) For current wide area imager, the large size of the crystal is the biggest limiting factor in achieving good angular resolution. Thus, if possible, application of depth of interaction measurements will improve the performance, although aggravating the complexity of the whole system.

5.5 Summary

A GAGG-SiPM Compton camera was built and evaluated in laboratory. The Compton camera was with 128 pixels. The total power consumption of the Compton camera including DAQ was 1584 mW. The measured angular resolution was 9.4° FWHM in azimuthal direction and 9.0° FWHM in lateral direction while the gap distance was 114 mm. The intrinsic efficiency was also calculated to be $1.01 pm 0.02\%$. With this angular resolution, the detector system is expected to achieve a spatial resolution of 1.6 m FWHM in azimuthal direction and 1.6 FWHM m in lateral direction at the position under the detector while it is working in CCM at an altitude of 10 m.

A new ASIC with 64ch DToT technology integrated was devised and evaluated in order to be applied as the front-end electronics for PD that is temperature independent. A very good linearity between the DToT time width and the input charge has been achieved. However, the ENC level obtained was a little bit high which cannot be used to process the signals from PDs. For semiconductors, e.g. Silicon strip detectors, or CdZnTe detectors, whose pulse heights are much higher than PD, this ASIC can be applied. Currently, we are designing another ASIC with a better ENC performance. In the coming future, PD will be employed to build a wide area gamma ray imager.

A new concept of reverse geometry for Compton camera to improve the detection efficiency as well as angular resolution for radioactive sources just under the detector was also proposed in this chapter. Two Compton cameras were built with a same number of pixels to demonstrate the concept. Comparison of experimental results shows that efficiency was improved by 20% in reverse geometry compared with that in normal geometry. Meanwhile, angular resolutions in both azimuthal and lateral directions were also improved. The reverse geometry for the evaluation experiments was very coarse and not optimized yet. Simulation works is demanded to determine

various parameters for this concept so as to obtain a maximized setup. These parameters include but not limit to the shape of both detector planes and the gap distance between them.

Field tests using the newly developed wide area gamma ray imager has also been conducted. GAGG-SiPM based large volume Compton camera was applied as the heart of the imager. The main purpose of the field measurements was to calibrate the performance of the wide area imager. To this end, the imager performed very well, e.g. with a similar count rate from each channel, the working temperature within the compensable range of the temperature compensation circuit. Preliminary reconstructed images were shown and discussed. Challenges to field imaging were detailedly studied and recommendations for the next run were made based on the calibration flights.

CHAPTER VI

Closing Remarks

The goal of this thesis is to design, fabricate and evaluate a gamma ray imager with wide area capability and high spatial resolution. To this end, both the prototype system and the newly developed large volume GAGG-SiPM imager performed very well both in laboratory and field environment. In addition, the multi-mode imaging capabilities for radioactive materials were demonstrated. Field testing of the wide area imager in Fukushima proved the systems and their Compton cameras capable of good performance and stability even in multivariate temperatures, high humidity, complicated terrain, and strong vibrations. Thanks for the application of DToT technology for signal processing, the built systems were with very low power consumption, e.g. power consumption of the large volume GAGG-SiPM system was only 1584 mW. Although the prototype wide area imager as well the benchmarked large volume system responses proved successful in wide area imaging in Fukushima, there remain several paths for optimization of the imager as well as technological challenges that need to be addressed prior to widespread deployment of a GAGG-based, Compton scattering principle applied gamma ray imager. The main achievements, advantages, limitations, and means for improvement of the wide area imager design and technology are summarized below.

6.1 Overall Achievements

In this work, a prototype Compton camera and another large volume Compton camera were designed, built, and tested. Both of them showed good spectral performance, promising angular resolutions and high efficiency. Equipping the Compton cameras on an unmanned helicopter, with proper configurations of orientation module, communication device with ground station, wide area gamma ray imagers with airborne imaging capability were built in the laboratory and assessed in field.

6.1.1 Performances of the two Wide Area Imagers

The prototype Compton camera, which performed as the heart of the prototype wide area imager, consisted 16 GAGG scintillators coupled to a 4 × 4 array of SiPM as the scatterer and another 16 GAGG scintillators coupled to a 4 × 4 array of APD as the absorber. The size of the GAGG in scatter was 10 mm × 10 mm × 5 mm while that in absorber was 1 centimeter cubic. The scatterer pixels achieved energy uncertainties of 6.5%(FWHM) at 662 keV, while absorber pixels of about 9%(FWHM) at 662 keV. The prototype system achieved an efficiency of 1.68%±0.04% and an angular resolution of 13.9°(FWHM) while working in CCM at the laboratory. In GCM with ESM applied, a spatial resolution of 10.7 cm(FWHM) was obtained when the distance of the detecting area is 11.2 cm away from the detector while it was 27.5 cm(FWHM) in SDM. The total power consumption of the prototype system was 1125 mW.

Followed the laboratory calibration of the Compton camera, the whole system was applied in field measurements in Fukushima. Results obtained demonstrate the system is useful for radiation detection and localization in a wide scale. Specifically, in GCM, the imager achieved the most detailed distribution map at an altitude of 10 m when ESM was applied. The reconstructed map based on the coincidence count rate

as a function of the GPS position was consistent with ground measured results using a gamma plotter at 5 cm height. In the map, two hot areas with a interval distance of 15 m between them were successfully identified and separated. A relationship between the coincidence count rate and the ground truth was also given. Therefore, the ground dose rate could be estimated using the recorded coincidence event in real radioactive materials detection and mapping. In CCM, although the imager could not give a diffuse distribution of the radionuclides as obtained in GCM, it was capable of imaging hot areas with higher spatial resolution. In real applications, these two working modes can be combined. The system can be firstly set to working in GCM to scan the contaminated places with high sensitivity, with the option of switching to CCM as soon as a radiation field of interest has been detected.

It is worth mentioning that before this prototype imager, there was not report about a successfully built and evaluated wide area imging system. It is also very meaningful to point out that, this prototype was also the first one to demonstrate the application of a Compton camera for aerial imaging in field.

Encouraged by the successful application of the prototype system in field and promising results obtained, a new GAGG-SiPM based large volume Compton camera was built and tested in the laboratory with the purpose to achieve higher efficiency and better angular resolution. The Compton camera was of 128 pixels. 64 10 mm $\times$ 10 mm $\times$ 5 mm GAGG crystals and another 64 10 mm $\times$ 10 mm $\times$ 10 mm GAGG crystals were coupled to two 8 $\times$ 8 arrays of SiPMs, respectively. The thinner detector array acted as the front plane to Compton scatter the incident photons, while the thicker arrays performed as the back plane to absorb the scattered gamma rays. The total power consumption of the Compton camera including DAQ was 1584 mW. All the pixels achieved an energy resolution of about 6%(FWHM) at 662 keV. The measured angular resolution was 9.4° FWHM in azimuthal direction and 9.0° FWHM in lateral direction while the gap distance was 114 mm. The intrinsic efficiency was

also calculated to be 1.01±0.02%. With this angular resolution, the detector system is expected to achieve a spatial resolution of 1.6 m FWHM in azimuthal direction and 1.6 FWHM m in lateral direction at the position under the detector while it is working in CCM at an altitude of 10 m.

The performance of the large volume detector in GCM was assessed by Geant4 simulation. In the simulation, the gap distance was 80 mm. The distance from the source to the scatterer plane was 100 mm. 4 different upper limits of energy losses on the scatter were selected to analyzed the results. The spatial resolutions when the upper limit was 50 keV, 100 keV, 200 keV, 300 keV and without ESM applied were 8.8 cm(FWHM), 10.6 cm(FWHM), 15.0 cm(FWHM), 18.2 cm(FWHM) and 21.4 cm(FWHM) respectively at 662 keV. And the spatial resolution in SDM was 24.0 cm(FWHM). In GCM with ESM applied, the spatial resolution can be largely improved compared with that in SDM. The spatial resolution was improved by 3 times in GCM with ESM applied compared with SDM.

Field experiment using the 8 × 8 SiPM system was conducted on Feb, 23rd, at the same place in Fukushima. The main purpose of the experiment was to calibrate the whole system. The test was focus on Compton imaging of hot regions. From the analysis of the result, the whole system performed very well, e.g., all the working channels almost had a similar count rate performance, the temperature in the enclosure of the Compton camera was within the compensable range of the temperature compensation circuits, and promising images were obtained under complicated terrains, high humidity, and strong AUH vibrations due to the wind. Challenges to field imaging were detailedly studied and recommendations for the next run were made based on the calibration flights.

6.1.2 Contributions of this Work

The most significant originality of this thesis is that a new concept of gamma ray imager that is capable of mapping diffuse distribution of radioactive materials, for homeland security, nuclear threat detection, is proposed. In this work, Compton cameras were firstly mounted on an unmanned helicopter to image the released nuclear isotopes in Fukushima, in a airborne measurement manner. Promising results both from calibration experiments in the laboratory and from filed tests demonstrate the wide area gamma ray imagers are of substantially enhanced abilities to detect, localize, characterize, monitor the transport of, and estimate the intensity of radiological and nuclear materials in a wide scale with high efficiency and accuracy.

In addition, through the application of DToT, we firstly and successfully built time-based Compton cameras with preponderant performance compared with other techniques, e.g. the mentioned instrument of HEMI and the Compton camera using 3D CZT detector. This new signal processing method showed its advantages in many aspects, e.g. good linearity, enough dynamic range, low power consumption, possibility of parallel signal processing, and capability of integration of both analog signals and digital signals in a single ASIC. The successfully application in a multi-channel system as Compton camera reveals the tremendous prospect of being applied in other gamma-ray imaging facilities such as PET and SPECT.

6.2 Limitations and Suggestions

Although the prototype wide area imager as well the benchmarked large volume system responses proved successful in wide area imaging in Fukushima, there remain several paths for optimization of the imager as well as technological challenges that need to be addressed prior to widespread deployment of a GAGG-based, Compton scattering principle applied gamma ray imager.

(1) The employment of SiPMs lowered the requirement for electronics due to their high signal to noise ratio. However, for the same reason, the performance of the whole system was dependent on the temperature.

Although temperature compensation circuits were applied, or even temperature compensation were employed during the data analysis process, the effect from the temperature can not be hundred-percent eliminated and still remains one big problem that depress the performance of the imagers. One reason is that the temperature sensor was not directly touched to the surface of the SiPMs, since each SiPM with the GAGG scintillator was enclosed by $BaSO_4$ to reflect the scintillation lights. Another reason might be the noise arose by the compensation circuits that has been ever observed during the laboratory tests.

One solution is, as discussed in Chapter V, to apply a compact temperature chamber to ensure the working temperature of SiPMs stable. The energy information obtained would be much more accurate due to the stable gain performance of the SiPMs. Another advantage for employing a temperature chamber is that the initial threshold could be set to be lower without any worries that the noise level would surpass it. As a result, events with much smaller energy depositions can be collected. And as discussed in Chapter II, those events with small scattering angles can help to achieve better angular resolution. Additionally, the efficiency can be also improved.

Another solution might be using PDs instead of SiPMs. With regards to the small signals from PD, substantially enhanced front-end electronics with low ENC are in great request. Commercial product, A250 is of noise at room temperature $\sim$100 electrons rms. Encouraged by the gap in ENC between our developed ASIC and the state of the art, there exist enormous potentialities of devising and fabricating ASICs with elevated performance.

(2) The cubic centimeter GAGG scincillators allow a simplified instrument design, since they greatly decrease the amount of electronics required to operate the system. This subsequently reduces the number of electronics-induced problems that always happen during real-world operations. But a significant compromise with regard to performance is imposed by the employment of large voxels.

The main issue with the large volume detectors is that the achievable angular resolution is limited for the Compton camera, since the interaction location resolution is determined by the size of the detector. This results in either a broad cross section distribution with long tails or in increase of sequences that can not be reconstructed, as discussed using simulation in Chaper III.

Depth of interaction(DOI) [155] could somehow decrease the influence because the position resolution in the axis direction can be determined. Recently, researchers from the National Institute of Radiological Science proposed a new X' tal cube PET detector with DOI capability [156, 157]. By optically covering all 6 surfaces of a segmented crystal block with multi-pixel photon counters (MPPCs), 2 mm^3 uniform crystal identification was successfully obtained. This method can be also applied to estimate the interaction position in GAGG, although the readout channels will be increased.

The best way is to reduce the voxel size. Because by doing this, not only the interaction location resolution can be declined, but also the fraction of useful events will be also increased, e.g. lower possibility will be obtained for a gamma-ray to have multi-scattering in a single crystal or in neighborhood crystals in the same detector array when small voxle size crystals are used, albeit at the cost of simplicity. ASIC application in the future could possible integrate a large number of channels in a sub-square centimeters size chip, thus subsequently allow the application of small voxel size crystals or DOI measurements.

(3) Taking advantage of the DToT technology, the DAQ was merely consisted of a FPGA with a verilog code running on it. The OR signals of scatterer and absorber are sent to a time window for coincidence measurement. A Visual Basic-based data logger was used to collect the energy, position, and timing information event by event through a USB connetion between a PC and the FPGA. Currently, two problems of the DAQ occurred during the tests and measurements. The DAQ software should be also improved to remedy the problems arose from it.

The first problem was, as shown in Chapter V, there were always signals from some channels can not be read, though the input are well prepared. It did not appear in the prototype system. One possible reason might be the competition and risk arose by the large number of channels and can be solved by carefully and professionally re-coding the verilog program. The other problem is about the data logger. Currently, the GPS information can only be updated after the total count was increased by 512 events. When the imager works in GCM at high altitude as a speed of 1 m/s, the GPS information might only be renewed over 10 seconds. This will decrease the spatial resolution since the distribution map was produced based on the coincidence count rate as a function of the GPS lacaltion.

(4) The present geometry of the Compton camera in the imager is sufficient for field testing and demonstration purpose. However, to improve the efficiency and sensitivity for the real applications in real world, the Compton camera would need to be modified to effectively make use of each pixel.

A reverse geometry for Compton camera introduced in Chapter V can be a good candidate for the modification. With less pixels constituting a circle shaped scatterer and more pixels forming a ring shaped absorber, the absolute efficiency

as well as the angular resolution would be improved when detecting the radioactive sources on the axis of the detector in far field.

Another path to increase the performance might be reinvestigating the pixel-to-pixel spacing in one array. Since, this can decrease those events that the scattered photons interact with detectors in the same plane. And those event can not be filtered during reconstruction. Carefully study based on Monte Carlo simulation might provide optimized spacing with respect to angular resolution and efficiency.

(5) Reconstructing images of the radioactive isotopes from the collected information of energy, timing, and position is as important as experiment itself. For specific detector in specific application, special reconstruction software should be developed. In this work, we programmed SBP, FBP and list mode MLEM reconstruction softwares that are, to be in truth, for general Compton cameras. However, for our GAGG based Compton camera, the reconstruction algorithms could be somehow improved, e.g. the Klein-Nishina formula could be further revised based on the real responses of the GAGG crystals to the incident gamma rays. The thickness of the Compton cones during reconstruction is also an interesting issue that worth the whistle. In this work, the thickness of the cones were chose to be similar as the real angular resolution.

The interaction position were set to be the center of each pixel, based on the assumption that the incident photons had a uniform possibility to interact at every point inside the crystal. However, in real experiment, this might not always true, with regard to the manufacture process, and the non-uniformity of incident angles of the photons. A Geant4 simulation was carried out to study the distribution of the interaction position inside a crystal using the same setup as described in Section 5.1.5. A 662 keV point source was placed on the

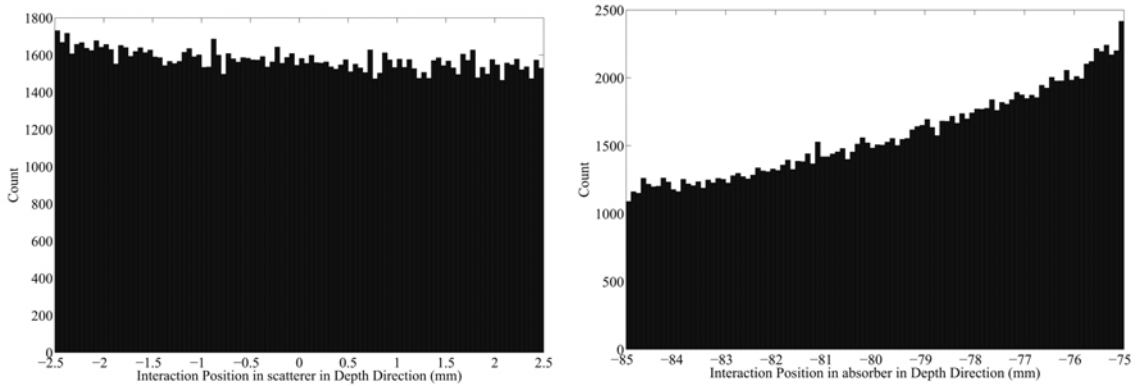

(a) Scatter (b) Absorber

Figure 6.1: Interaction position distribution in depth direction.

axis and 100 mm in front of the detector. Figure 6.1 shows the distributions of interaction positions in depth direction of both the scatterer and absorber. The interaction position in depth direction in scatter is uniformly distributed, however, the scattered photons tend to interact with front part of the absorber in greater possibilities.

In addition, as mentioned in Chapter V, 3D reconstruction would be required in CCM for hot regions imaging due to the complicated terrain and radiation from vegetation. If possible, real time imaging is also welcome for future applications.

6.3 Conclusions

Regardless of the current limitations of the imagers and unmanned helicopter vibrations, the benchmarked response and proven capabilities of this new concept of wide area imaging as demonstrated with the prototype imager, the calibrated large volume system and through simulation is an important step for the development, fabrication, and application of wide area gamma ray imagers. The multi working modes of the systems were also proven and in either of them, the wide area imagers are able to provide detailed distribution map of radioactive sources in a wide scale. In

real-world application, these two working modes are recommended to be combined. The system is firstly set to work in GCM to scan the contaminated places with high sensitivity, with the option of switching to CCM once a radiation field of interest has been detected. The systems can be rapidly improved for future measurements based upon the findings of this work.

BIBLIOGRAPHY

BIBLIOGRAPHY

[1] World Nuclear Association. http://www.world-nuclear.org/, 2012.

[2] International Atomic Energy Agency 'Fukushima Nuclear Accident Update Log.' . http://www.iaea.org/newscenter, 2012.

[3] MEXT. http://www.kananet.com/fukushima-osenmap/, 2011.

[4] Teppei J Yasunari, Andreas Stohl, Ryugo S Hayano, John F Burkhart, Sabine Eckhardt, and Tetsuzo Yasunari. Cesium-137 deposition and contamination of japanese soils due to the fukushima nuclear accident. *Proceedings of the National Academy of Sciences*, 108(49):19530–19534, 2011.

[5] Yasuto Miyake, Hiroyuki Matsuzaki, Takeshi Fujiwara, Takumi Saito, Takeyasu Yamagata, Maki Honda, and Yasuyuki Muramatsu. Isotopic ratio of radioactive iodine (129 i/131 i) released from fukushima daiichi npp accident. *Geochemical Journal*, 46(4):327–333, 2012.

[6] M Yamamoto, A Sakaguchi, S Ochiai, and T Imanaka. Isotopic compositions of transuranic nuclides released by the fukushima dai-ichi nuclear power plant accident: with emphasis on cm isotopes. *Journal of Radioanalytical and Nuclear Chemistry*, 300(3):1045–1052, 2014.

[7] Glenn F Knoll. *Radiation detection and measurement*. John Wiley & Sons, 2010.

[8] David L Chichester and Scott M Watson. Multispectral uv-visual imaging as a tool for locating and assessing ionizing radiation in air. In *Nuclear Science Symposium Conference Record (NSS/MIC), 2010 IEEE*, pages 447–453. IEEE, 2010.

[9] James M Hall, Steve Asztalos, Peter Biltoft, J Church, M-A Descalle, Thomas Luu, D Manatt, G Mauger, Eric Norman, D Petersen, et al. The nuclear car wash: Neutron interrogation of cargo containers to detect hidden snm. *Nuclear Instruments and Methods in Physics Research Section B: Beam Interactions with Materials and Atoms*, 261(1):337–340, 2007.

[10] P Linden, JK-H Karlsson, B Dahl, I Pazsit, and G Por. Localisation of a neutron source using measurements and calculation of the neutron flux and its gradient. *Nuclear Instruments and Methods in Physics Research Section A: Accelerators, Spectrometers, Detectors and Associated Equipment*, 438(2):345–355, 1999.

[11] Kevin D Krenz, Nicholas Mascarenhas, James S Brennan, Stanley Mrowka, and Peter Marleau. Results with the neutron scatter camera. Technical report, Sandia National Laboratories, 2008.

[12] Nicholas Mascarenhas, James Brennan, Kevin Krenz, Peter Marleau, and Stanley Mrowka. Results with the neutron scatter camera. *Nuclear Science, IEEE Transactions on*, 56(3):1269–1273, 2009.

[13] Peter Marleau, James Brennan, Erik Brubaker, Nathan Hilton, and John Steele. Active coded aperture neutron imaging. In *Nuclear Science Symposium Conference Record (NSS/MIC), 2009 IEEE*, pages 1974–1977. IEEE, 2009.

[14] A De Angelis, O Mansutti, and Massimo Persic. *Very-high-energy gamma astrophysics*. Societa italiana di fisica, 2008.

[15] F Aharonian, AG Akhperjanian, AR Bazer-Bachi, B Behera, M Beilicke, W Benbow, D Berge, K Bernlöhr, C Boisson, O Bolz, et al. Discovery of very high energy gamma-ray emission coincident with molecular clouds in the w 28 (g6. 4-0.1) field. *Astronomy & Astrophysics*, 481(2):401–410, 2008.

[16] Christian Joram, Jaques Seguinot, and Peter Weilhammer. Gamma ray detector for positron emission tomography (pet) and single photon emisson computed tomography (spect), July 17 2002. US Patent App. 10/521,221.

[17] WB Gilboy, J Foster, and M Folkard. A tomographic gamma-ray scanner for industrial applications. *Nuclear Instruments and Methods in Physics Research*, 193(1):209–214, 1982.

[18] Robley Dunglison Evans and Atome Noyau. *The atomic nucleus*, volume 582. McGraw-Hill New York, 1955.

[19] Richard Fitzgerald. Phase-sensitive x-ray imaging. *Phys Today*, 53:82, 2000.

[20] Michael E Phelps. Emission computed tomography. In *Seminars in nuclear medicine*, volume 7, pages 337–365. Elsevier, 1977.

[21] Glenn F Knoll. Single-photon emission computed tomography. *Proceedings of the IEEE*, 71(3):320–329, 1983.

[22] Mark W Groch and William D Erwin. Spect in the year 2000: basic principles. *Journal of Nuclear Medicine Technology*, 28(4):233–244, 2000.

[23] Raichle M E Ter-Pogossian M M and Sobel B E. Positron-emission tomography. 1980.

[24] John M Ollinger and Jeffrey A Fessler. Positron-emission tomography. 1997.

[25] El E Fenimore and TM Cannon. Coded aperture imaging with uniformly redundant arrays. *Applied optics*, 17(3):337–347, 1978.

[26] Sonal Joshi Kaye, Willy Robert Kaye, Jason Michael Jaworski, and Zhong He. Experimental limitations of coded aperture imaging using thick 3d-position-sensitive cdznte detectors. In *Nuclear Science Symposium Conference Record (NSS/MIC), 2010 IEEE*, pages 3856–3859. IEEE, 2010.

[27] Klaus P Ziock, Jeff Collins, Mark Cunningham, Lorenzo Fabris, Timothy Gee, James Goddard, Frezghi Habte, and Thomas Karnowski. The use of gamma-ray imaging to improve portal monitor performance. *Nuclear Science, IEEE Transactions on*, 55(6):3654–3664, 2008.

[28] Willy R Kaye, Nathan D Bennett, Christopher G Wahl, Zhong He, and Weiyi Wang. Gamma-ray source location by attenuation measurements. In *Nuclear Science Symposium Conference Record, 2007. NSS'07. IEEE*, volume 2, pages 1294–1298. IEEE, 2007.

[29] Oskar Klein and Yoshio Nishina. Über die streuung von strahlung durch freie elektronen nach der neuen relativistischen quantendynamik von dirac. *Zeitschrift für Physik*, 52(11-12):853–868, 1929.

[30] TCS-171B/172B. `https://www.hitachi-aloka.co.jp/products/data/radiation-002-TCS-171172`, 2014.

[31] Michelle Galloway, Andreas Zoglauer, Mark Amman, Steven E Boggs, and Paul N Luke. Simulation and detector response for the high efficiency multimode imager. *Nuclear Instruments and Methods in Physics Research Section A: Accelerators, Spectrometers, Detectors and Associated Equipment*, 652(1):641–645, 2011.

[32] Dan Xu, Zhong He, Carolyn E Lehner, and Feng Zhang. 4-pi compton imaging with single 3d position-sensitive cdznte detector. In *Optical Science and Tech-*

nology, the SPIE 49th Annual Meeting, pages 144–155. International Society for Optics and Photonics, 2004.

[33] Carolyn E Lehner, Zhong He, and Feng Zhang. 4π compton imaging using a 3-d position-sensitive cdznte detector via weighted list-mode maximum likelihood. *Nuclear Science, IEEE Transactions on*, 51(4):1618–1624, 2004.

[34] Dan Xu and Zhong He. Filtered back-projection in 4π compton imaging with a single 3d position sensitive cdznte detector. *Nuclear Science, IEEE Transactions on*, 53(5):2787–2796, Oct 2006.

[35] Shin Watanabe, Takaaki Tanaka, Kazuhiro Nakazawa, Takefumi Mitani, Kousuke Oonuki, Tadayuki Takahashi, Takeshi Takashima, Hiroyasu Tajima, Yasushi Fukazawa, Masaharu Nomachi, et al. A si/cdte semiconductor compton camera. *Nuclear Science, IEEE Transactions on*, 52(5):2045–2051, 2005.

[36] Shin' ichiro Takeda, Hiroyuki Aono, Sho Okuyama, S-n Ishikawa, Hirokazu Odaka, Shin Watanabe, Motohide Kokubun, Tadayuki Takahashi, Kazuhiro Nakazawa, Hiro Tajima, et al. Experimental results of the gamma-ray imaging capability with a si/cdte semiconductor compton camera. *Nuclear Science, IEEE Transactions on*, 56(3):783–790, 2009.

[37] J Kataoka, A Kishimoto, T Nishiyama, T Fujita, K Takeuchi, T Kato, T Nakamori, S Ohsuka, S Nakamura, M Hirayanagi, et al. Handy compton camera using 3d position-sensitive scintillators coupled with large-area monolithic mppc arrays. *Nuclear Instruments and Methods in Physics Research Section A: Accelerators, Spectrometers, Detectors and Associated Equipment*, 732:403–407, 2013.

[38] Wanno Lee, Gyuseong Cho, and Ho Dong Kim. A radiation monitoring system

with capability of gamma imaging and estimation of exposure dose rate. *Nuclear Science, IEEE Transactions on*, 49(3):1547–1551, Jun 2002.

[39] Cheol-Ha Baek, Ji Yeon Hwang, Su Jung An, Hyun-Il Kim, Sung-Woo Kwak, and Yong Hyun Chung. Portable nuclear safeguard equipment using pinhole gamma camera. In *Nuclear Science Symposium Conference Record (NSS/MIC), 2010 IEEE*, pages 454–456, Oct 2010.

[40] Cheol-Ha Baek, Su Jung An, Hyun-il Kim, Sung-Woo Kwak, and Yong Hyun Chung. Development of a pinhole gamma camera for environmental monitoring. *Radiation Measurements*, 59:114–118, 2013.

[41] Y Sanada, T Sugita, Y Nishizawa, A Kondo, and T Torii. The aerial radiation monitoring in japan after the fukushima dai-ichi nuclear power plant accident. *Prog. Nucl. Sci. Tech.*, 4:76–80, 2014.

[42] Shinichi Okuyama, Tatsuo Torii, Yasunori Nawa, Ikuo Kinoshita, Akihiko Suzuki, Masanori Shibuya, and Nobuyuki Miyazaki. Development of a remote radiation monitoring system using unmanned helicopter. In *International Congress Series*, volume 1276, pages 422–423. Elsevier, 2005.

[43] Shin-ichi Okuyama, Tatsuo Torii, Akihiko Suzuki, Masanori Shibuya, and Nobuyuki Miyazaki. A remote radiation monitoring system using an autonomous unmanned helicopter for nuclear emergencies. 2008.

[44] Yukihisa Sanada and Tatsuo Torii. Aerial radiation monitoring around the fukushima dai-ichi nuclear power plant using an unmanned helicopter. *Journal of environmental radioactivity*, 139:294–299, 2015.

[45] SE Inderhees, BF Phlips, RA Kroeger, WN Johnson, RL Kinzer, JD Kurfess, B Graham, and N Gehrels. Spectroscopy, imaging and compton-scatter polarime-

try with a germanium strip detector. *Nuclear Science, IEEE Transactions on*, 43(3):1467–1471, 1996.

[46] Feng Zhang, Zhong He, and Carolyn E Seifert. A prototype three-dimensional position sensitive cdznte detector array. *Nuclear Science, IEEE Transactions on*, 54(4):843–848, 2007.

[47] D. Protic, E.L. Hull, T. Krings, and K. Vetter. Large-volume si(li) orthogonal-strip detectors for compton-effect-based instruments. *Nuclear Science, IEEE Transactions on*, 52(6):3181–3185, Dec 2005.

[48] Hiroyuki Takahashi, Yuki Mitsuya, Takeshi Fujiwara, and Takashi Fushie. Development of a glass gem. *Nuclear Instruments and Methods in Physics Research Section A: Accelerators, Spectrometers, Detectors and Associated Equipment*, 724:1–4, 2013.

[49] LG Hyman. Time resolution of photomultiplier systems. *Review of Scientific Instruments*, 36(2):193–196, 1965.

[50] Ralph W Engstrom. *Photomultiplier handbook*. RCA Corp., 1980.

[51] Tsutomu Ishi, Junichi Fujikata, Kikuo Makita, Toshio Baba, and Keishi Ohashi. Si nano-photodiode with a surface plasmon antenna. *Japanese Journal of Applied Physics*, 44(3L):L364, 2005.

[52] RB Emmons. Avalanche-photodiode frequency response. *Journal of Applied Physics*, 38(9):3705–3714, 1967.

[53] P Buzhan, B Dolgoshein, A Ilyin, V Kantserov, V Kaplin, A Karakash, A Pleshko, E Popova, S Smirnov, Yu Volkov, et al. An advanced study of silicon photomultiplier. *ICFA Inst. Bull*, 21:28, 2001.

[54] P Buzhan, B Dolgoshein, L Filatov, A Ilyin, V Kantzerov, V Kaplin, A Karakash, F Kayumov, S Klemin, E Popova, et al. Silicon photomultiplier and its possible applications. *Nuclear Instruments and Methods in Physics Research Section A: Accelerators, Spectrometers, Detectors and Associated Equipment*, 504(1):48–52, 2003.

[55] B Dolgoshein, V Balagura, P Buzhan, M Danilov, L Filatov, E Garutti, M Groll, A Ilyin, V Kantserov, V Kaplin, et al. Status report on silicon photomultiplier development and its applications. *Nuclear Instruments and Methods in Physics Research Section A: Accelerators, Spectrometers, Detectors and Associated Equipment*, 563(2):368–376, 2006.

[56] Beverly E Law. *Remote sensing of radiation intercepted by vegetation to estimate aboveground net primary production across western Oregon.* PhD thesis, 1993.

[57] Shunsuke Kurosawa, Yasuhiro Shoji, Yuui Yokota, Kei Kamada, Valery I Chani, and Akira Yoshikawa. Czochralski growth of gd 3 (al 5- x ga x) o 12 (gagg) single crystals and their scintillation properties. *Journal of Crystal Growth*, 393:134–137, 2014.

[58] Kei Kamada, Shunsuke Kurosawa, Petr Prusa, Martin Nikl, Vladimir V Kochurikhin, Takanori Endo, Kousuke Tsutumi, Hiroki Sato, Yuui Yokota, Kazumasa Sugiyama, et al. Cz grown 2-in. size ce: Gd 3 (al, ga) 5 o 12 single crystal; relationship between al, ga site occupancy and scintillation properties. *Optical Materials*, 36(12):1942–1945, 2014.

[59] Carolyn E. Lehner. *4-PI compton Imaging using a single 3-D position sensitive CdZNTe detector.* PhD thesis, The University of Michigan, 2004.

[60] Hao Yang. *Applications of Digital ASIC Array System for Noise analysis, non-*

linearity correction, event classification and reconstruction. PhD thesis, The University of Michigan, 2013.

[61] Jason M. Jaworski. *Compton Imaging Algorithms for Position-Sensitive Gamma-Ray Detectors in the Presence of Motion.* PhD thesis, The University of Michigan, 2013.

[62] Yanfeng Du. *Development of a prototype compton scattering camera using 3-D position sensitive CZT detectoprs.* PhD thesis, The University of Michigan, 2001.

[63] William R. Kaye. *Energy and Position Reconstruction in Pixelated CdZnTe Detectors.* PhD thesis, The University of Michigan, 2012.

[64] Christopher G. Wahl. *Imaging, Detection, and Identification Algorithms for Position-Sensitive Gamma-Ray Detectors.* PhD thesis, The University of Michigan, 2011.

[65] Daniel J. Lingenfelter. *Source Detection and Image Reconstruction with position sensitive gamma ray detectors.* PhD thesis, The University of Michigan, 2012.

[66] Weiyi Wang. *Techniques and Applications of Compton Imaging for position senseitive gamma-ray detectors.* PhD thesis, The University of Michigan, 2011.

[67] Chibueze Uche. *Optimizing Compton Camera Performance.* PhD thesis, The University of Waikato, 2011.

[68] Wen Li. *Three-dimensional position sensitive CdZnTe Gamma ray spectrometers.* PhD thesis, The University of Michigan, 2001.

[69] Dan Xu. *Gamma-ray imaging and polarization measurement using 3-D position sensitive CdZnTe detectors.* PhD thesis, The University of Michigan, 2006.

[70] Lucas C Parra. Reconstruction of cone-beam projections from compton scattered data. *Nuclear Science, IEEE Transactions on*, 47(4):1543–1550, 2000.

[71] T Tomitani and M Hirasawa. Image reconstruction from limited angle compton camera data. *Physics in medicine and biology*, 47(12):2129, 2002.

[72] Roman Basko, Gengsheng L Zeng, and Grant T Gullberg. Application of spherical harmonics to image reconstruction for the compton camera. *Physics in Medicine and Biology*, 43(4):887, 1998.

[73] Michael J Cree and Philip J Bones. Towards direct reconstruction from a gamma camera based on compton scattering. *Medical Imaging, IEEE Transactions on*, 13(2):398–407, 1994.

[74] Harrison H Barrett, Timothy White, and Lucas C Parra. List-mode likelihood. *JOSA A*, 14(11):2914–2923, 1997.

[75] Lucas Parra and Harrison H Barrett. List-mode likelihood: Em algorithm and image quality estimation demonstrated on 2-d pet. *Medical Imaging, IEEE Transactions on*, 17(2):228–235, 1998.

[76] Scott J Wilderman, Jeffrey A Fessler, Neal H Clinthorne, JW LeBlanc, and W Les Rogers. Improved modeling of system response in list mode em reconstruction of compton scatter camera images. *Nuclear Science, IEEE Transactions on*, 48(1):111–116, 2001.

[77] Scott J Wilderman, Neal H Clinthorne, Jeffrey A Fessler, and W Les Rogers. List-mode maximum likelihood reconstruction of compton scatter camera images in nuclear medicine. In *Nuclear Science Symposium, 1998. Conference Record. 1998 IEEE*, volume 3, pages 1716–1720. IEEE, 1998.

[78] JW LeBlanc, NH Clinthorne, C-H Hua, E Nygard, WL Rogers, DK Wehe, P Weilhammer, and SJ Wilderman. Experimental results from the c-sprint prototype compton camera. *Nuclear Science, IEEE Transactions on*, 46(3):201–204, 1999.

[79] G.J. Schmid, D.A. Beckedahl, J.E. Kammeraad, J.J. Blair, K. Vetter, and A. Kuhn. Gamma-ray compton camera imaging with a segmented hpge. *Nuclear Instruments and Methods in Physics Research Section A: Accelerators, Spectrometers, Detectors and Associated Equipment*, 459(3):565 – 576, 2001.

[80] Feng Zhang, Zhong He, Glenn F Knoll, David K Wehe, and James E Berry. 3-d position sensitive cdznte spectrometer performance using third generation vas/tat readout electronics. *Nuclear Science, IEEE Transactions on*, 52(5):2009–2016, 2005.

[81] TJ O'Neill, D Bhattacharya, S Blair, G Case, OT Tumer, RS White, and AD Zych. The tigre desktop prototype results for 511 and 900 kev gamma rays. *Nuclear Science, IEEE Transactions on*, 42(4):933–939, 1995.

[82] BF Phlips, SE Inderhees, RA Kroeger, WN Johnson, RL Kinzer, JD Kurfess, BL Graham, and N Gehrels. Performance of a compton telescope using position-sensitive germanium detectors. *Nuclear Science, IEEE Transactions on*, 43(3):1472–1475, 1996.

[83] J.B. Martin, G.F. Knoll, D.K. Wehe, N. Dogan, V. Jordanov, N. Petrick, and M. Singh. A ring compton scatter camera for imaging medium energy gamma rays. *Nuclear Science, IEEE Transactions on*, 40(4):972–978, Aug 1993.

[84] Volker Schönfelder, Andreas Hirner, and K Schneider. A telescope for soft gamma ray astronomy. *Nuclear Instruments and Methods*, 107(2):385–394, 1973.

[85] D Herzo, R Koga, WA Millard, S Moon, J Ryan, R Wilson, AD Zych, and RS White. A large double scatter telescope for gamma rays and neutrons. *Nuclear Instruments and Methods*, 123(3):583–597, 1975.

[86] RW Todd, JM Nightingale, and DB Everett. A proposed gamma camera. *Nature*, 251:132–134, 1974.

[87] D.B. Everett, J.S. Fleming, R.W. Todd, and J.M. Nightingale. Gamma-radiation imaging system based on the compton effect. *Electrical Engineers, Proceedings of the Institution of*, 124(11):995–, November 1977.

[88] Manbir Singh. An electronically collimated gamma camera for single photon emission computed tomography. part i: Theoretical considerations and design criteria. *Medical Physics*, 10(4):421–427, 1983.

[89] Manbir Singh and David Doria. An electronically collimated gamma camera for single photon emission computed tomography. part ii: Image reconstruction and preliminary experimental measurements. *Medical Physics*, 10(4):428–435, 1983.

[90] R Ricardo Brechner and Manbir Singh. Comparison of an electronically collimated system and a mechanical cone-beam system for imaging single photons. *Nuclear Science, IEEE Transactions on*, 35(1):649–653, 1988.

[91] V Schönfelder, R Diehl, GG Lichti, H Steinle, BN Swanenburg, AJM Deerenberg, H Aarts, J Lockwood, W Webber, J Macri, et al. The imaging compton telescope comptel on the gamma ray observatory. *Nuclear Science, IEEE Transactions on*, 31(1):766–770, 1984.

[92] T Kamae, N Hanada, and R Enomoto. Prototype design of multiple compton gamma-ray camera. *Nuclear Science, IEEE Transactions on*, 35(1):352–355, 1988.

[93] Christopher John Solomon and Robert John Ott. Gamma ray imaging with silicon detectors—a compton camera for radionuclide imaging in medicine. *Nuclear Instruments and Methods in Physics Research Section A: Accelerators, Spectrometers, Detectors and Associated Equipment*, 273(2):787–792, 1988.

[94] N Dogan, David K Wehe, and Glenn F Knoll. Multiple compton scattering gamma ray imaging camera. 1990.

[95] N Dogan and DK Wehe. Optimization and angular resolution calculations for a multiple compton scatter camera. In *Nuclear Science Symposium and Medical Imaging Conference, 1993., 1993 IEEE Conference Record.*, pages 269–273. IEEE, 1994.

[96] Jerome Edward Gormley, WL Rogers, NH Clinthorne, DK Wehe, and GF Knoll. Experimental comparison of mechanical and electronic gamma-ray collimation. *Nuclear Instruments and Methods in Physics Research Section A: Accelerators, Spectrometers, Detectors and Associated Equipment*, 397(2):440–447, 1997.

[97] A.I. Bolozdynya, V.V. Egorov, A.V. Koutchenkov, G.A. Safronov, G.N. Smirnov, S.A. Medved, and V.L. Morgunov. High pressure xenon electronically collimated camera for low energy gamma ray imaging. *Nuclear Science, IEEE Transactions on*, 44(6):2408–2414, Dec 1997.

[98] Ichiro Fujieda and Victor Perez-Mendez. Theoretical considerations of a new electronically collimated gamma camera utilizing gas scintillation. *Japanese Journal of Applied Physics*, 25(12R):1925, 1986.

[99] J.W. LeBlanc, N.H. Clinthorne, C.-H. Hua, E. Nygard, W.L. Rogers, D.K. Wehe, P. Weilhammer, and S.J. Wilderman. C-sprint: a prototype compton camera system for low energy gamma ray imaging. *Nuclear Science, IEEE Transactions on*, 45(3):943–949, Jun 1998.

[100] Elena Aprile, Valeri Egorov, Fang Xu, Edward L Chupp, Philip P Dunphy, Tadayoshi Doke, Jun Kikuchi, Gerald J Fishman, Geoffrey N Pendleton, Kimiaki Masuda, et al. Liquid xenon gamma-ray imaging telescope (lxegrit) for medium energy astrophysics. In *SPIE's 1996 International Symposium on Optical Science, Engineering, and Instrumentation*, pages 337–348. International Society for Optics and Photonics, 1996.

[101] Elena Aprile, Valeri Egorov, Karl-Ludwig Giboni, Steven M Kahn, Tomotake Kozu, Uwe G Oberlack, S Centro, Sandro Ventura, Tadayoshi Doke, Jun Kikuchi, et al. Xena: a liquid-xenon compton telescope for gamma-ray astrophysics in the mev regime. In *SPIE's International Symposium on Optical Science, Engineering, and Instrumentation*, pages 88–99. International Society for Optics and Photonics, 1998.

[102] YF Du, Z He, GF Knoll, DK Wehe, and W Li. Evaluation of a compton scattering camera using 3-d position sensitive cdznte detectors. *Nuclear Instruments and Methods in Physics Research Section A: Accelerators, Spectrometers, Detectors and Associated Equipment*, 457(1):203–211, 2001.

[103] Yanfeng Du. *Development of a prototype Compton scattering camera using 3-D position sensitive CZT detectors.* University of Michigan., 2001.

[104] MA Deleplanque, IY Lee, K Vetter, GJ Schmid, FS Stephens, RM Clark, RM Diamond, P Fallon, and AO Macchiavelli. Greta: utilizing new concepts in γ-ray detection. *Nuclear Instruments and Methods in Physics Research Section A: Accelerators, Spectrometers, Detectors and Associated Equipment*, 430(2):292–310, 1999.

[105] EA Wulf, J Ampe, WN Johnson, RA Kroeger, JD Kurfess, and BF Phlips. Depth

measurement in a germanium strip detector. *Nuclear Science, IEEE Transactions on*, 49(4):1876–1880, 2002.

[106] Eric A. Wulf, Bernard F. Phlips, W. Neil Johnson, R.A. Kroeger, J.D. Kurfess, and Elena I. Novikova. Germanium strip detector compton telescope using three-dimensional readout. *Nuclear Science, IEEE Transactions on*, 50(4):1182–1189, Aug 2003.

[107] F Lebrun, A Bazzano, V Borrel, M Casse, A Bykov, A Coc, F Daigne, P Goldoni, J Grigorczuck, M Hernanz, et al. The compton cube. *Nuclear Instruments and Methods in Physics Research Section A: Accelerators, Spectrometers, Detectors and Associated Equipment*, 504(1):38–43, 2003.

[108] R Orito, H Kubo, K Miuchi, T Nagayoshi, A Takada, T Tanimori, and M Ueno. A novel design of the mev gamma-ray imaging detector with micro-tpc. *Nuclear Instruments and Methods in Physics Research Section A: Accelerators, Spectrometers, Detectors and Associated Equipment*, 513(1):408–412, 2003.

[109] Lisha Zhang, W Leslie Rogers, and Neal H Clinthorne. Potential of a compton camera for high performance scintimammography. *Physics in medicine and biology*, 49(4):617, 2004.

[110] Takefumi Mitani, Takaaki Tanaka, Kazuhiro Nakazawa, Tadayuki Takahashi, Takeshi Takashima, Hiroyasu Tajima, Hidehito Nakamura, Masaharu Nomachi, Tatsuya Nakamoto, and Yasushi Fukazawa. A prototype si/cdte compton camera and the polarization measurement. *Nuclear Science, IEEE Transactions on*, 51(5):2432–2437, 2004.

[111] Shin Watanabe, Takaaki Tanaka, Kazuhiro Nakazawa, Takefumi Mitani, Kousuke Oonuki, Tadayuki Takahashi, Takeshi Takashima, Hiroyasu Tajima, Ya-

sushi Fukazawa, Masaharu Nomachi, et al. A si/cdte semiconductor compton camera. *Nuclear Science, IEEE Transactions on*, 52(5):2045–2051, 2005.

[112] Tadayuki Takahashi et al. The astro-h mission, 2010.

[113] Dan Xu, Zhong He, Carolyn E Lehner, and Feng Zhang. 4-pi compton imaging with single 3d position-sensitive cdznte detector. In *Optical Science and Technology, the SPIE 49th Annual Meeting*, pages 144–155. International Society for Optics and Photonics, 2004.

[114] C.E. Lehner, Zhong He, and Feng Zhang. 4 pi; compton imaging using a 3-d position-sensitive cdznte detector via weighted list-mode maximum likelihood. *Nuclear Science, IEEE Transactions on*, 51(4):1618–1624, Aug 2004.

[115] Mark Amman, Paul N Luke, Julie S Lee, Lucian Mihailescu, Kai Vetter, Andreas Zoglauer, Cornelia B Wunderer, Michelle Galloway, Steven E Boggs, Henry Chen, et al. Detector module development for the high efficiency multimode imager. In *Nuclear Science Symposium Conference Record (NSS/MIC), 2009 IEEE*, pages 981–985. IEEE, 2009.

[116] Michelle Galloway, Andreas Zoglauer, Mark Amman, Steven E Boggs, and Paul N Luke. Simulation and detector response for the high efficiency multimode imager. *Nuclear Instruments and Methods in Physics Research Section A: Accelerators, Spectrometers, Detectors and Associated Equipment*, 652(1):641–645, 2011.

[117] K. Vetter, D. Chivers, B. Plimley, A. Coffer, T. Aucott, and Q. Looker. First demonstration of electron-tracking based compton imaging in solid-state detectors. *Nuclear Instruments and Methods in Physics Research Section A: Accelerators, Spectrometers, Detectors and Associated Equipment*, 652(1):599 – 601,

2011. Symposium on Radiation Measurements and Applications (SORMA) {XII} 2010.

[118] Brian Plimley, Daniel Chivers, Amy Coffer, Tim Aucott, Wenni Wang, and Kai Vetter. Reconstruction of electron trajectories in high-resolution si devices for advanced compton imaging. *Nuclear Instruments and Methods in Physics Research Section A: Accelerators, Spectrometers, Detectors and Associated Equipment*, 652(1):595–598, 2011.

[119] DH Chivers, A Coffer, B Plimley, and K Vetter. Impact of measuring electron tracks in high-resolution scientific charge-coupled devices within compton imaging systems. *Nuclear Instruments and Methods in Physics Research Section A: Accelerators, Spectrometers, Detectors and Associated Equipment*, 654(1):244–249, 2011.

[120] LE Smith, C Chen, Z He, and DK Wehe. Hybrid collimation for industrial gamma ray imaging: combining spatially coded and compton aperture data. In *Nuclear Science Symposium, 1998. Conference Record. 1998 IEEE*, volume 2, pages 1040–1045. IEEE, 1998.

[121] LE Smith, C Chen, DK Wehe, and Z He. Hybrid collimation for industrial gamma-ray imaging: combining spatially coded and compton aperture data. *Nuclear Instruments and Methods in Physics Research Section A: Accelerators, Spectrometers, Detectors and Associated Equipment*, 462(3):576–587, 2001.

[122] Brian L Evans, Jeffrey B Martin, Larry W Burggraf, MC Roggemann, and T-N Hangartner. Demonstration of energy-coded compton scatter tomography with fan beams for one-sided inspection. *Nuclear Instruments and Methods in Physics Research Section A: Accelerators, Spectrometers, Detectors and Associated Equipment*, 480(2):797–806, 2002.

[123] CDR Azevedo, FA Pereira, T Lopes, PMM Correia, ALM Silva, LFND Carramate, DS Covita, and JFCA Veloso. A gaseous compton camera using a 2d-sensitive gaseous photomultiplier for nuclear medical imaging. *Nuclear Instruments and Methods in Physics Research Section A: Accelerators, Spectrometers, Detectors and Associated Equipment*, 732:551–555, 2013.

[124] G Llosá, J Cabello, S Callier, JE Gillam, C Lacasta, M Rafecas, L Raux, C Solaz, V Stankova, C de La Taille, et al. First compton telescope prototype based on continuous labr 3-sipm detectors. *Nuclear Instruments and Methods in Physics Research Section A: Accelerators, Spectrometers, Detectors and Associated Equipment*, 718:130–133, 2013.

[125] Y Kong, H Brands, T Glaser, C Herbach, L Hoy, M Kreuels, M Kuster, G Pausch, J Petzoldt, C Plettner, et al. A prototype compton camera array for localization and identification of remote radiation sources. *Nuclear Science, IEEE Transactions on*, 60(2):1066–1071, 2013.

[126] L Zhang, SJ Wilderman, NH Clinthorne, and WL Rogers. An anthropomorphic phantom integrated egs4 monte carlo code and its application in compton probe. In *Nuclear Science Symposium Conference Record, 2000 IEEE*, volume 3, pages 20–119. IEEE, 2000.

[127] L.J. Meng and D.K. Wehe. Feasibility study of using hybrid collimation for nuclear environmental imaging. *Nuclear Science, IEEE Transactions on*, 50(4):1103–1110, Aug 2003.

[128] Malcolm J Cooper. Compton scattering and electron momentum. *Contemporary Physics*, 18(5):489–517, 1977.

[129] Roland Ribberfors. Relationship of the relativistic compton cross section to the

momentum distribution of bound electron states. *Phys. Rev. B*, 12:2067–2074, Sep 1975.

[130] D Brusa, G Stutz, JA Riveros, JM Fernández-Varea, and F Salvat. Fast sampling algorithm for the simulation of photon compton scattering. *Nuclear Instruments and Methods in Physics Research Section A: Accelerators, Spectrometers, Detectors and Associated Equipment*, 379(1):167–175, 1996.

[131] F Biggs, LB Mendelsohn, and JB Mann. Hartree-fock compton profiles for the elements. *Atomic data and nuclear data tables*, 16(3):201–309, 1975.

[132] R. Ribberfors and K. F. Berggren. Incoherent-x-ray-scattering functions and cross sections $(\mathrm{d}\sigma/\mathrm{d}\omega')_{\mathrm{incoh}}$ by means of a pocket calculator. *Phys. Rev. A*, 26:3325–3333, Dec 1982.

[133] C.E. Ordonez, Wei Chang, and A. Bolozdynya. Angular uncertainties due to geometry and spatial resolution in compton cameras. In *Nuclear Science Symposium, 1998. Conference Record. 1998 IEEE*, volume 3, pages 1535–1540 vol.3, 1998.

[134] L.A. Shepp and Y. Vardi. Maximum likelihood reconstruction for emission tomography. *Medical Imaging, IEEE Transactions on*, 1(2):113–122, Oct 1982.

[135] K. Shimazoe, H. Takahashi, Boxuan Shi, T. Orita, T. Furumiya, J. Ooi, and Y. Kumazawa. Dynamic time over threshold method. *Nuclear Science, IEEE Transactions on*, 59(6):3213–3217, Dec 2012.

[136] Allison et al. J. Geant4 developments and applications. *Nuclear Science, IEEE Transactions on*, 53(1):270–278, Feb 2006.

[137] S. Agostinelli et al. Geant4—a simulation toolkit. *Nuclear Instruments and*

Methods in Physics Research Section A: Accelerators, Spectrometers, Detectors and Associated Equipment, 506(3):250 – 303, 2003.

[138] Vladimir Ivanchenko, John Apostolakis, Alexander Bagulya, H Ben Abdelouahed, R Black, A Bogdanov, H Burkhard, S Chauvie, P Cirrone, G Cuttone, et al. Recent improvements in geant4 electromagnetic physics models and interfaces. In *3th Monte Carlo Conference MC2010*, volume 2, pages 898–903, 2011.

[139] J Apostolakis, M Asai, AG Bogdanov, H Burkhardt, G Cosmo, S Elles, G Folger, VM Grichine, P Gumplinger, A Heikkinen, et al. Geometry and physics of the geant4 toolkit for high and medium energy applications. *Radiation Physics and Chemistry*, 78(10):859–873, 2009.

[140] CERN. `http://geant4.web.cern.ch/geant4/support/download.shtml`, 2015.

[141] The Geant4 Low Energy Electromagnetic Physics Working Group. `https://twiki.cern.ch/twiki/bin/view/Geant4/LowEnergyElectromagneticPhysicsWorkingGroup`, 2014.

[142] R Marc Kippen. The geant low energy compton scattering (glecs) package for use in simulating advanced compton telescopes. *New Astronomy Reviews*, 48(1):221–225, 2004.

[143] Gamma plotter(ES 7410). `http://e-energy.co.jp/gammarod`, 2012.

[144] Hamamatsu(S3590-08). `http://www.hamamatsu.com/jp/ja/product/alpha/P/4103/S3590-08/index.html`, 2012.

[145] Veljko Radeka. Low-noise techniques in detectors. *Annual Review of Nuclear and Particle Science*, 38(1):217–277, 1988.

[146] T Orita, K Shimazoe, and H Takahashi. The dynamic time-over-threshold method for multi-channel apd based gamma-ray detectors. *Nuclear Instruments and Methods in Physics Research Section A: Accelerators, Spectrometers, Detectors and Associated Equipment*, 775:154–161, 2015.

[147] Orita Tadashi. *Study on a time-width signal processing method of radiation signals.* PhD thesis, The University of Tokyo, 2014.

[148] TR-71ui Thermo recorder. `http://www.tandd.co.jp/product/discon/tr7ui/`, 2013.

[149] Scott J Wilderman, NH Clinthorne, JA Fessler, Ch Hua, and W Rogers. List mode em reconstruction of compton scatter camera images in 3-d. In *Proc. IEEE Nuclear Science Symp*, volume 3. Citeseer.

[150] Anne C Sauve, AO Hero, W Leslie Rogers, SJ Wilderman, and NH Clinthorne. 3d image reconstruction for a compton spect camera model. *Nuclear Science, IEEE Transactions on*, 46(6):2075–2084, 1999.

[151] Soo Mee Kim, Jae Sung Lee, Mi No Lee, Ju Hahn Lee, Chun Sik Lee, Chan-Hyeong Kim, Dong Soo Lee, and Soo-Jin Lee. Two approaches to implementing projector–backprojector pairs for 3d reconstruction from compton scattered data. *Nuclear Instruments and Methods in Physics Research Section A: Accelerators, Spectrometers, Detectors and Associated Equipment*, 571(1):255–258, 2007.

[152] Andriy Andreyev, Arkadiusz Sitek, and Anna Celler. Fast image reconstruction for compton camera using stochastic origin ensemble approach. *Medical physics*, 38(1):429–438, 2011.

[153] Van-Giang Nguyen, Soo-Jin Lee, and Mi No Lee. Gpu-accelerated 3d bayesian

image reconstruction from compton scattered data. *Physics in medicine and biology*, 56(9):2817, 2011.

[154] Junqiang Li and John Valentine. Direct 3d image reconstruction for the energy subtraction compton scattering camera (escsc) with spatially invariant point spread function. In *Nuclear Science Symposium Conference Record, 2001 IEEE*, volume 4, pages 2147–2151. IEEE, 2001.

[155] David Peter Thomas Scraggs. *Digital signal processing techniques for semiconductor Compton cameras*. PhD thesis, Ph. D. Thesis, The University of Liverpool, 2007.

[156] Taiga Yamaya, Takayuki Mitsuhashi, Takahiro Matsumoto, Naoko Inadama, Fumihiko Nishikido, Eiji Yoshida, Hideo Murayama, Hideyuki Kawai, Mikio Suga, and Mitsuo Watanabe. A sipm-based isotropic-3d pet detector x'tal cube with a three-dimensional array of 1 mm 3 crystals. *Physics in Medicine and Biology*, 56(21):6793, 2011.

[157] Y. Yazaki, N. Inadama, F. Nishikido, T. Mitsuhashi, M. Suga, Kengo Shibuya, M. Watanabe, T. Yamashita, E. Yoshida, H. Murayama, and T. Yamaya. Development of the x'tal cube: A 3d position-sensitive radiation detector with all-surface mppc readout. *Nuclear Science, IEEE Transactions on*, 59(2):462–468, April 2012.